The Pennsylvania State University

The Graduate School

# IMPROVEMENTS TO TEMPERATURE PREDICTIONS OF FILM COOLED SOLIDS USING ITERATIVE CONJUGATE HEAT TRANSFER AND REDUCED ORDER FILM MODELING

A Dissertation in

Mechanical Engineering

by

Peter T. Ingram



Submitted in Partial Fulfillment

of the Requirements

for the Degree of

Doctor of Philosophy

August 2023

The dissertation of Peter T. Ingram was reviewed and approved by the following:

Stephen Lynch

Associate Professor of Mechanical Engineering

Dissertation Adviser

Chair of Committee

Anil Kulkarni

Professor of Mechanical Engineering

Daniel Haworth

Professor of Mechanical Engineering

Director of Graduate Program

David Hall

Assistant Professor of Aerospace Engineering

## Abstract

To accurately predict the life of turbine blade, accurate temperature predictions are necessary. It is widely accepted that the life of a turbine blade can be reduced by half if the temperature prediction of the metal blade is off by only 30°C.

This paper extends Iterative Conjugate Heat Transfer (ICHT) and Reduced Order Film Modeling (ROFM) to include spanwise variation in film cooling parameters by developing a model to extend the spanwise-averaged correlations into two-dimensional correlations, implement a superposition model for multiple row injection, and implement a model for coolant warming to increase the accuracy of these temperature predictions.

Three-dimensional temperature distributions in film cooled solids are calculated using ICHT-ROFM. ICHT is used to obtain conjugate temperature profiles using a loosely coupled system. The convective heat transfer is calculated on a similar blade without film-cooling while under the same flow conditions. The heat transfer coefficients are corrected by use of experimental data or correlations to incorporate the effect of film-cooling on the heat transfer coefficients. This is called Reduced Order Film Cooling (ROFM). ROFM needs experimental input for film cooling effectiveness and film heat transfer coefficients.

The developed correlations were used to predict the temperature downstream from a cooling hole for various conductivity and plate thicknesses for both spanwise averaged cooling parameters (1D) and spanwise varied parameters (2D). It was found that the spanwise averaged calculations underpredict temperatures, relative to the new model, by around 4% for Biot values similar to first row cooling holes in turbine blade applications.

Coolant warming was also accounted for and implemented in ICHT-ROFM method. It was found that coolant warming through the cooling holes causes about a 1% increase in surface temperatures for the case considered. While not significant, it is expected that in turbine applications, the coolant warming will be more significant, leading to larger increases in surface temperature.

# Table of Contents

## List of Figures

# List of Tables

# Nomenclature

$AR$ = Area ratio, $AR = A_{exit}/A_{hole}$

$D$ = Diameter of injection hole

$DR$ = Density ratio, $DR = \rho_c/\rho_G$

$h$ = Heat transfer coefficient (W/m$^2$K)

$h_f$ = Film heat transfer coefficient defined as follows

$$h_f = q_W/(T_{AW} - T_W)$$

$\left(\frac{h_f}{h_0}\right)$ =Film cooling heat transfer coefficient augmentation

$h_\theta$ = Film cooling heat transfer based on local temperature difference defined as

$$h_\theta = h_0\left(\frac{h_f}{h_0}\right)[1 - \eta\theta]$$

$I$ = Momentum flux ratio

$L$ = Length of hole from plenum to exit

$M$ = Blowing ratio or mass flux ratio

$$M = U_c\rho_c/U_G\rho_G$$

$P$ = Spanwise pitch, distance between holes within a row

$q_W$" = heat flux at fluid-solid interface surface (W/ m$^2$)

$s$ = Streamwise pitch, distance between rows of holes

$t$ = breakthrough width

$T_{aw}$ = Adiabatic wall temperature

$T_C$ = Temperature of secondary gas or coolant

$T_G$ = Temperature of mainstream gas

$T_W$ = Temperature of fluid-solid interface surface

$Tu$ % = Free stream turbulent intensity

$V_G$ = Mainstream gas inlet velocity

$x$ = streamwise coordinate

$z$ = spanwise coordinate

$z'$ = spanwise location of local maximum

### Greek

$\alpha$ = Inclination injection angle, angle from surface plane to axis of cooling hole
$\beta$ = Compound injection angle, projected angle between streamwise direction and axis of cooling hole
$\eta$ = Adiabatic film-cooling effectiveness

$$\eta = (T_G - T_{AW})/(T_G - T_j)$$

$\theta$ = nondimensional wall temperature

$$\theta = (T_G - T_c)/(T_G - T_w)$$

$\sigma$ = Lateral spreading of film cooling effectiveness

$\phi$ = nondimensional jet exit temperature (used elsewhere as $\chi$: coolant warming factor)

$$\phi = (T_G - T_j)/(T_G - T_C)$$

### Subscript

$0$ = No film-cooling
$C$ = Secondary gas or coolant side
$CL$ = Centerline
$e$ = at the hole exit

$G$ = mainstream gas side
$h$ = individual hole location
$j$ = jet exit or hole exit
$P$ or max=maximum value at a specified streamwise position

$x$ = streamwise component

$z$ = spanwise component

$\eta$ = effectiveness

### Accent

$\bar{X}$ = laterally averaged quantity (e.g., $\bar{\eta}$ )

# Chapter 1: Introduction

## 1.1 Background

An increase in the efficiency of gas turbines can be obtained by increasing turbine inlet temperature. Higher efficiencies allow turbine engines to produce higher thrust at lower costs. For engine power to double, the rotor inlet temperature should increase from 2500°F to 3500°F, as stated by Han et al. [1]. At such elevated temperatures, multiple modes of structural failure are present, including creep, cracking, oxidation, and melting. Keeping the metal components from failing in the turbine requires constant cooling. There are various cooling technologies that allow the blades to operate at temperatures hundreds of degrees above their melting temperatures. The most common techniques used today are convection cooling, impingement cooling and film-cooling, Sunden et al. [2].

Convection cooling refers to bleeding air from the compressor stage and passing it through cavities in the blade material. The cooling air is fed through the root of the blade. Often, turbulators are used to enhance mixing and increase the heat transfer in serpentine channels passing through the blade. Convection cooling is very common and is often combined with other cooling techniques, such as impingement or film-cooling.

Impingement cooling refers to cooling the back side of shell airfoil by directing jets. The shell is fabricated like sheet metal and offset from the rest of the blade material. This method of cooling is very effective and is often utilized in combination with other cooling schemes on early-stage blades and vanes, where temperatures of the gas stream are the highest.

Film-cooling refers to jets of coolant air that are injected into the boundary layer through discrete holes in the blade. This cooling technique is very effective and provides protection by using the coolant air to displace the hot exhaust gases and insulate the blade material from excessive heat transfer. Oftentimes, film-cooling is used in concert with other cooling techniques. It is not uncommon for the cooling jets to be fed from a convective cooling serpentine or for discrete cooling holes to be drilled into the shell of an impingement cooled airfoil. The focus of this paper will be flows with film-cooling. The purpose of this study is to further the development and

validation of a model for performing film-cooling calculations while including the thermal resistance of the metal, known as conjugate heat transfer effects.

Film cooling is fundamentally a jet in cross-flow. Mahesh [3] provides a comprehensive overview of steady jets in cross-flow. Gevorkyan et al. [4] performed experimental studies of a round jet in cross-flow. They found that for density ratios below unity did not mix as well as near unity. This was due to the difference in behavior between the low-density shear layer and high-density main flow. Zang and New [5] studied the near-hole behavior of a pair of jets using laser-induced fluorescence and particle imaging velocimetry. They found that there was significant flow shear stress from the interacting pair of inner vortices. Figure 1 shows the vortex structures of a jet in cross-flow.

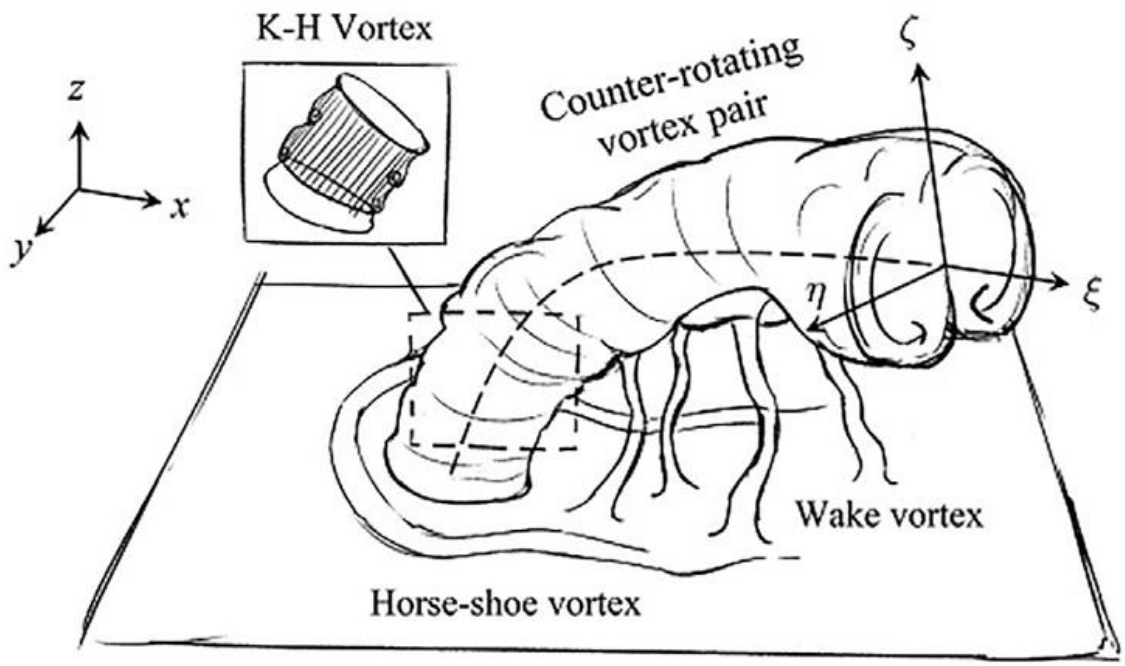


**Figure 1. Schematic of the vortex structures of a transverse jet in cross-flow [6].**

## 1.2 Derivation of Important Film-Cooling Properties

In fluid dynamics and heat transfer, it is important to develop dimensionless parameters that describe the physical phenomenon. For film-cooling, which can be seen diagramed in Figure 2, the definition of heat transfer without film-cooling, denoted with subscript "0", and with film-cooling, denoted with subscript "$f$", is required. The respective definitions can be seen in Equations (1) and (2).

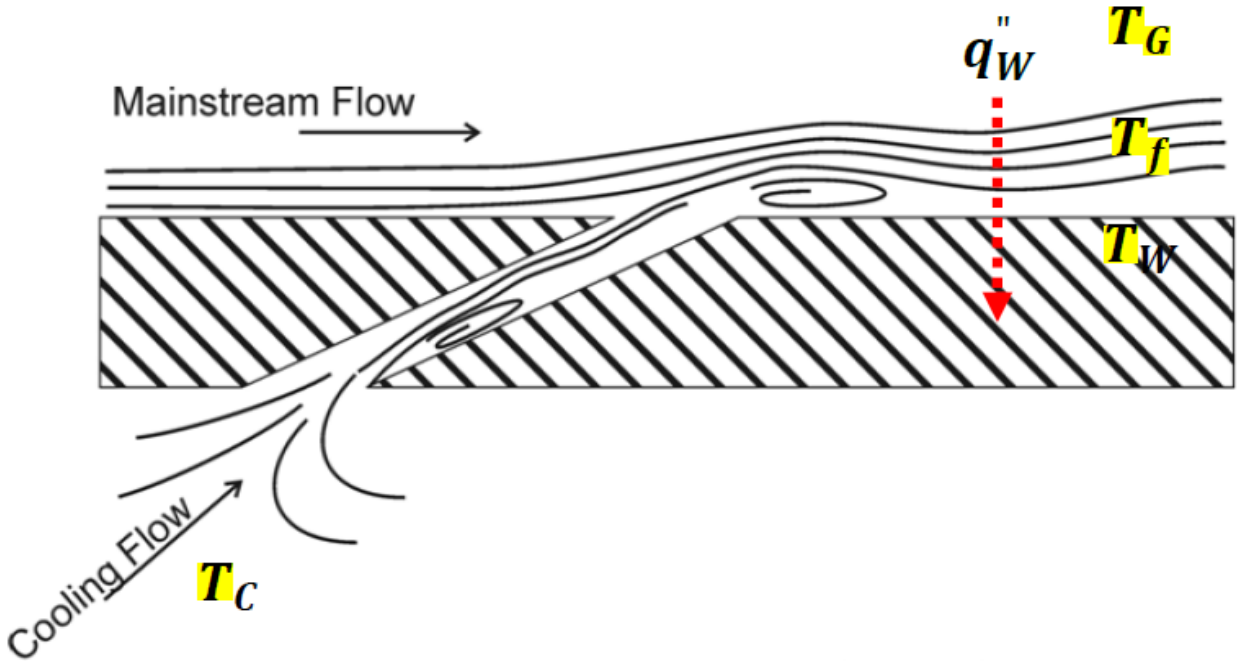


**Figure 2. Injection of Film Coolant [7].**

$$q_0'' = h_0(T_G - T_W) \tag{1}$$

$$q_f'' = h_f(T_f - T_W) \tag{2}$$

Where $T_G$ is the temperature of the mainstream gas, $T_W$ is the local wall temperature, and $T_f$ is the local film temperature which is equal to the wall temperature for similar flow conditions with an adiabatic wall, $T_{aw}$. This is true when the recovery effects are small, which is the case for many scaled experiments.

The ratio of these forms the dimensionless quantity below:

$$\frac{q_f''}{q_0''} = \frac{h_f(T_f - T_W)}{h_0(T_G - T_W)} \tag{3}$$

Some minor mathematical manipulation of Equation (3) yields the standard parameters.

$$\frac{q_f''}{q_0''} = \left(\frac{h_f}{h_0}\right)[1 - \eta\theta] \tag{4}$$

Where

$$\eta = \frac{T_G - T_{aw}}{T_G - T_C} = \frac{T_G - T_f}{T_G - T_C} \tag{5}$$

And

$$\theta = \frac{T_G - T_C}{T_G - T_W} \tag{6}$$

Here $\left(\frac{h_f}{h_0}\right)$ is the heat transfer coefficient augmentation, $\eta$ is the adiabatic effectiveness, and $\theta$ is the dimensionless wall temperature. In this instance, an $h_\theta$ is defined such that:

$$q_f'' = h_f(T_f - T_W) = h_\theta(T_G - T_W) \tag{7}$$

Which when normalized yields a similar relationship Equation (4).

$$\frac{q_f''}{q_0''} = \left(\frac{h_f}{h_0}\right)[1 - \eta\theta] = \frac{h_\theta}{h_0} \tag{8}$$

And hence

$$h_\theta = h_0\left(\frac{h_f}{h_0}\right)[1 - \eta\theta] \tag{9}$$

$$q_f'' = h_0\left(\frac{h_f}{h_0}\right)[1 - \eta\theta](T_G - T_W) \tag{10}$$

Therefore, it is possible to calculate the local heat flux under film cooling if the local convective heat transfer coefficient without the effects of film cooling, the local wall temperature, the heat transfer coefficient augmentation, and the adiabatic effectiveness are all known. The heat transfer coefficient augmentation and adiabatic effectiveness can be obtained from experimental data or empirical correlations.

## 1.3 Standard Experiments for Measuring Film Cooling Parameters

### Film Cooling Effectiveness

The coolant is injected ($T_C$) at a temperature that is not equal to the free stream gas temperature ($T_G$) with a wall heat flux ($q_W''$) of zero, typically created experimentally by using low conductivity material for the test model. The adiabatic wall temperature ($T_{AW}$) will be equal to the film temperature ($T_f$) under these conditions. The adiabatic film cooling effectiveness can then be calculated using Equation (5).

### Heat Transfer Coefficient Augmentation

The coolant is injected at the free stream gas temperature ($T_C = T_G$) with a small amount of wall heat flux ($q_W''$). At this condition, according to Equation (6), $\theta = 0$ and when $\theta = 0$, according to Equation (8), then $h_f = h_\theta$. That is to say, the convective heat transfer coefficient with film cooling is same as the standard definition basted on the local temperature difference between the wall and the free stream gas. The heat transfer coefficient without film cooling is measured under the same geometry and flow conditions except without any coolant injected.

An alternate method to arrive $h_\theta$ is by superimposing the temperature fields from two different coolant temperatures and a constant wall temperature, per Eckert [8]. The first case is when the coolant temperature is equal to the freestream gas temperature ($T_C = T_G$), that is $\theta = 0$. The second is performed with the coolant temperature equal to the wall temperature ($T_C = T_W$), or

when $\theta = 1$. These two temperature fields can be combined using Equation (11) to calculate the heat transfer coefficient at any arbitrary temperature.

$$h_\theta = h(0) + \theta[h(1) - h(0)] \tag{11}$$

## 1.4 Development of Reduced Order Film Model (ROFM)

The Reduced Order Film Model is based on the assumption that the film-cooling parameters are dependent solely on the flow field. This assumption is already made in literature; Baldauf et al [9] define the spanwise averaged Stanton number for a flow over a film-cooled solid as Equation (12).

$$\bar{St}_{f,non-conj} = f\left(\bar{\theta}, M, DR, Tu, \frac{x}{D}, \alpha, \frac{P}{D}, \frac{\delta_1}{D}, \frac{L}{D}\right) \tag{12}$$

Removing the spanwise averaging adds a dependency on the normalized spanwise direction ($\frac{z}{D}$) and Eq. (12) becomes.

$$St_{f,non-conj} = f\left(\theta, M, DR, Tu, \frac{x}{D}, \frac{z}{D}\alpha, \frac{P}{D}, \frac{\delta_1}{D}, \frac{L}{D}, \ldots\right) \tag{13}$$

Since the temperature dependency in Eq (13) limits the range of applicability, dividing the film-cooled Stanton number by the baseline uncooled Stanton number removes the temperature dependency leaving effects of film cooling injection parameters and geometry intact, Jennings [7]. This removes the temperature dependency as the uncooled Stanton number is only dependent on the temperature effects, as the injection parameters and hole geometry are not relevant to an uncooled surface.

$$\frac{St_{f,non-conj}}{St_{0,non-conj}} = \frac{h_{f,non-conj}}{h_{0,non-conj}} = f\left(M, DR, Tu, \frac{x}{D}, \frac{z}{D}\alpha, \frac{P}{D}, \frac{\delta_1}{D}, \frac{L}{D}\right) \tag{14}$$

Similarly, this can be done for the conjugate case as well, in which other cooling and conduction within the object affect the temperature at the surface.

$$\frac{St_{f,conj}}{St_{0,conj}} = \frac{h_{f,conj}}{h_{0,conj}} = f\left(M, DR, Tu, \frac{x}{D}, \frac{z}{D}\alpha, \frac{P}{D}, \frac{\delta_1}{D}, \frac{L}{D}\right) \tag{15}$$

Furthermore, since both augmentation functions have no dependency on temperature, both should have the same dependency on the injection parameters and hole geometry, since there is no difference in those parameters between the non-conjugate and conjugate analyses. Thus, the two augmentations can be equated

$$\left(\frac{h_f}{h_0}\right)_{conj} = \left(\frac{h_f}{h_0}\right)_{non-conj} \tag{16}$$

$$h_\theta = h_{0_{conj}}\left(\frac{h_f}{h_0}\right)_{non-conj}[1-\eta\theta] \tag{17}$$

Substituting the definition of the heat transfer coefficients as defined by Equation (8) yields,

$$\left(\frac{q_f{}''/(T_f - T_W)}{q_0{}''/(T_G - T_W)}\right)_{conj} = \left(\frac{q_f{}''/(T_f - T_W)}{q_0{}''/(T_G - T_W)}\right)_{non-conj}$$

$$\left(\frac{q_f{}''}{q_0{}''}\right)_{conj} = \left(\frac{q_f{}''}{q_0{}''}\right)_{non-conj}\left(\frac{T_G - T_W}{T_f - T_W}\right)_{non-conj}\left(\frac{T_f - T_W}{T_G - T_W}\right)_{conj}$$

$$\left(\frac{q_f{}''}{q_0{}''}\right)_{conj} = \left(\frac{q_f{}''}{q_0{}''}\right)_{non-conj}\left[\frac{(T_G - T_W)_{non-conj}}{(T_G - T_W)_{conj}}\right]\left[\frac{(T_f - T_W)_{conj}}{(T_f - T_W)_{non-conj}}\right] \tag{18}$$

The two temperature ratios can be separated and defined as follows in Equations (19) and (20).

$$\varphi_1 = \left[\frac{(T_G - T_W)_{non-conj}}{(T_G - T_W)_{conj}}\right] \tag{19}$$

$$\varphi_2 = \left[\frac{(T_f - T_W)_{conj}}{(T_f - T_W)_{non-conj}}\right] \tag{20}$$

It can easily be shown that $\varphi_1$ is simply the ratio of the conjugate dimensionless wall temperature and the non-conjugate dimensionless wall temperature.

Equations (19) and (20) can be substituted into Equation (18)

$$\left(\frac{q_f''}{q_0''}\right)_{conj} = \varphi_1\left(T_G, T_{W,conj}, T_{W,non-conj}\right)\varphi_2\left(T_f, T_{W,conj}, T_{W,non-conj}\right)\left(\frac{q_f''}{q_0''}\right)_{non-conj} \tag{21}$$

The local heat fluxes are temperature dependent, but the non-dimensional form has the dependency on temperature largely removed. When $\varphi_1\varphi_2$=1, the conjugate and non-conjugate heat flux will be the same. This can occur when $\varphi_1 = \frac{1}{\varphi_2}$ which occurs under one of two conditions. The first is when $T_G = T_f$ which occurs when there is no film cooling, and not of interest of this study as most first stage vanes and blades have full coverage film-cooling. The second is when $T_{W,conj} = T_{W,non-conj}$ which occurs when the metal has a very high thermal conductivity. Gas turbine blades usually consist of a low thermal conductivity metal coated in a low conductivity thermal barrier, so this case will not occur.

When $\varphi_1$ is greater than 1, then the non-conjugate solution is under predicting the blade temperature. This will result in shorter than expected part life or blade failure. When $\varphi_1$ is less than 1, then blade is over-cooled locally. This results in lower efficiency of the turbine. Neither of these situations are desirable.

## 1.5 Methods of Temperature Prediction

Most manufacturers use what is termed a conventional technique to determine blade temperature distribution using experimental and numerical results. In this approach, the values for adiabatic effectiveness and film heat transfer coefficient are paired with a Finite Element Analysis to determine the solid temperatures.

The full conjugate heat transfer method (CHT) method refers to modeling the entirety of the flow and the solid simultaneously. This includes modeling all internal flows, the external flow, and the injection of the coolant into the mainstream flow. This is computationally expensive due to the resolution and turbulence modeling requirements for the flow and can suffer from numerical inaccuracies due to the different timescales of convection versus conduction.

The Iterative Conjugate Heat Transfer Technique (ICHT) technique is a practical compromise between full conjugate simulations and conventional techniques to determine the solid temperature distribution, with which one can limit the inaccuracies of full CHT by providing experimental input to correctly predict the temperature field. In this methodology, convection and conduction domains are loosely coupled, wherein external convective heat transfer coefficient provides the boundary condition for conduction in blade metal, corrected by use of experimental data to incorporate the effect of film-cooling on the heat transfer coefficients. This is similar to the conventional method. The effect of conjugate heat transfer is taken into account by using this iterative technique known as the ICHT-Reduced Order Film Modeling (ROFM) process and can be seen in Figure 3. Consideration of conjugate heat transfer results in different surface temperatures after each iteration. This changes the temperature profiles near the wall leading to changes in the heat transfer coefficients. New heat transfer coefficients give new wall temperature distribution. Therefore, this process is iterated until convergence is achieved and both wall temperatures and heat transfer coefficients do not change anymore. Iterations stop when convergence is obtained, indicated by the continuity of temperature and heat flux at the fluid-metal interface.

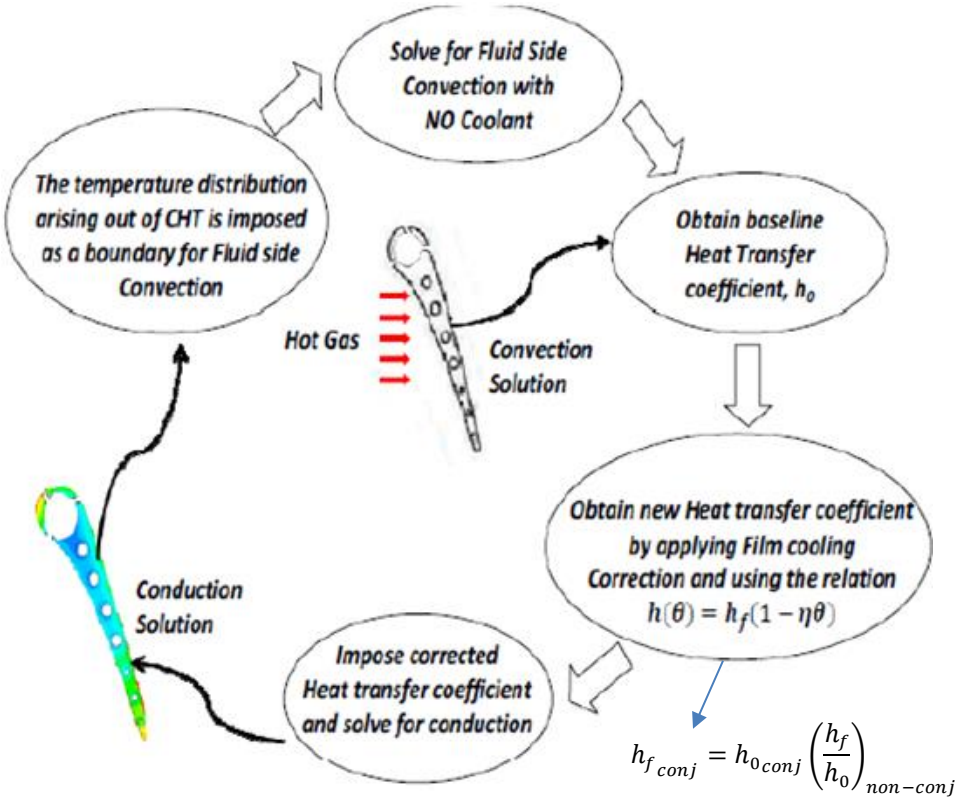


**Figure 3. Flow chart of the ICHT-ROFM technique [7].**

The conventional method does not take into account the effect of conjugate heat transfer on the heat transfer coefficients. Silieti et al. [10] reported that the full conjugate heat transfer (CHT) model shows a significant difference in temperature prediction when compared to adiabatic cases and confirmed that the CHT model can take into account the mutual influence of heat transfer on fluid flow and vice versa. They compared the centerline effectiveness for both adiabatic and conjugate cases and showed that a significant improvement in conjugate effectiveness of up to 3 times in the immediate region of the film cooling hole ($x/D < 6$) is observed. Bohn et al.'s [11] conjugate studies of a film-cooled turbine blade predicted 8% difference in temperatures for conjugate and decoupled conventional approach. Lu et al. [12] concluded that the application of the conjugate method includes the influence of heat transfer on the velocity field within the film. Kane and Yavuzkurt [13], who performed numerical simulation on a non-film-cooled blade, reported 30% deviation from data of Hylton and Nirmalan [14] in using the conventional constant wall temperature approach, whereas full conjugate results were much closer to the data with an overall deviation about a few percent. From the above mentioned review of literature, it

can be inferred that conjugate heat transfer plays a significant role in correctly predicting surface temperatures and heat transfer coefficients, as it takes into account effects arising out of internal convection and blade metal conduction. Dhiman and Yavuzkurt [15] developed an Iterative Conjugate Heat Transfer Technique (ICHT) where flow over a film-cooled blade is not solved directly. Instead, convective heat transfer is calculated on a similar blade without film-cooling and under the same flow conditions are corrected by use of experimental data to incorporate the effect of film-cooling on the heat transfer coefficients. The effect of conjugate heat transfer is taken into account by using this iterative technique. This approach is later named ICHT-Reduced Order Film Modeling (ROFM) technique. Using ICHT for uncooled surfaces, the deviations were as high as 3.5% between conjugate and conventional technique results for the wall temperature. In terms of convective heat transfer coefficient, this deviation is around 20%. Using ICHT-ROFM for film-cooled flat plates with high temperature differences, a deviation of up to 10% in wall temperature and 60% in heat transfer coefficients are observed. However, for film-cooling flows with low temperature differences between the mainstream flow and the coolant, a nominal deviation of up to 3% in wall temperature is observed indicating that the conjugate heat transfer effect diminishes with decreasing temperature difference.

## 1.6 Experimental Studies on Film-Cooling

Many researchers have studied the application of film-cooling to flat plates and gas turbine blades using experimental, theoretical, and numerical approaches. Goldstein [16] provided a review of early film-cooling studies. Yuen & Martinez [17], [18], [19] & [20] did an exhaustive study on film-cooling characteristics of round hole and presented film-cooling effectiveness and heat transfer coefficient data for various injection angles for single holes and rows of holes. Effectiveness and heat transfer coefficient augmentation were measured for a single hole for parameters of inclination angle, $\alpha$ =30, 60, and $90^0$, blowing ratio, $M$ =0.33-2 with a hole length of $L/D$ =4. For multiple rows, the data was measured for a spanwise pitch, $P/D$ =1 and 6 and for inline and staggered rows with streamwise pitch, $s/D$ =12.5. This data leads to a large amount of insight on how the film cooling properties behave in these configurations.

Similarly, Baldauf et al. [21], [22], [23] & [9] conducted a detailed study at engine-like conditions to obtain film-cooling effectiveness and heat transfer coefficient data at the mainstream temperature of 550K for various injection angles and blowing ratios. Baldauf et al collected effectiveness and heat transfer coefficient augmentation data for inclination angles, $\alpha$ =30, 60, and $90^0$, spanwise pitch of $P/D$ =2, 3, and 5, turbulence intensity of $Tu\%$ =1.5, 4%, $M$ =0.2-2.5, density ratio of $DR$ =1.2, 1.5, and 1.8 which was later used to develop detailed correlations.

Goldstein [16] summarized various geometry and flow related effects on film-cooling flows. Ekkad et al. [24] published a study measuring effectiveness and heat transfer data using transient liquid crystallography. They showed how utilizing a compound injection angle can increase film effectiveness. Both Yuen et al. and Baldauf et al. provided span-wise averaged and 2D contour plots of their data sets. Gritsch et al. [25] performed high speed experiments with diffuser holes on a flat plate. Data was reported for Mach numbers up to 0.6 and blowing ratios up to 2.0.

Hylton et al. [26] performed high speed, high temperature studies on a C3X vane in a linear cascade. The blade material chosen was stainless steel, allowing for conduction effects to play a prominent role in heat transfer and resulting in conjugate data. The data reported in this study is much more representative of what occurs in an engine as a result. Both experimental data and numerical results were reported in this study.

Sellers et al. [27] developed a superposition technique for the adiabatic effectiveness. This method was developed for slot cooling. This method assumes an approximately uniform spanwise profile. The resulting method can be seen in Equation (22) with the subscripts denoting the film-cooling slot.

$$\bar{\eta} = \bar{\eta}_1(x) + \bar{\eta}_2(x) - \bar{\eta}_1(x)\bar{\eta}_2(x) \qquad (22)$$

This method has been modified in an attempt to make it applicable for multiple rows of film-cooling holes. Zhu et al. [28] modified this method by adding weighting functions to correct for geometric differences. Two staggered rows of dustpan shaped holes with blowing ratio $M$ =0.5-2 were used in this study.

$$\bar{\eta} = a\bar{\eta}_1(x) + b\bar{\eta}_2(x) - b\bar{\eta}_1(x)\bar{\eta}_2(x) \tag{23}$$

The coefficients a and b in Equation (23) were developed to be functions of the blowing ratio.

Dees et al [29] investigated the effects of pressure gradient and freestream turbulence on the velocity and thermal boundary layer formation for a thermally similar turbine blade where temperature profiles were scaled to match engine conditions. It was found that effects on boundary growth vary significantly depending on the side of the turbine blade the boundary layer is forming, and both the pressure gradient and freestream turbulence need to be considered.

Chavez et al [30] investigated the effects of internally cooling on the effectiveness of a film cooled turbine blade with shaped holes. They found that the internal cooling from the cooling holes provided sufficient cooling in the near hole region. The internal cooling had a significant effect on the 3D conduction though the turbine blade and needs to be accounted for when predicting temperatures. They suggested using a significant conduction correction to the adiabatic effectiveness.

## 1.7 Correlations of Film-Cooling Properties

Several researchers have taken detailed and complete data on film-cooling effectiveness ($\eta$ ) and film heat transfer coefficient ($h_f$) which are needed for calculation of temperatures of film-cooled solid surfaces. Yuen & Martinez's [17] & [18] measurements were made for a single hole, whereas Baldauf's et al. [21] & [22] were for a row of holes. This data, and others like it, have been used to generate many correlations for $\eta$ and $h_f$ for many different film-cooling geometries and flow characteristics.

Baldauf et al. [23] & [9] used the data they collected to develop spanwise-averaged correlations for effectiveness and heat transfer coefficient augmentation for cylindrical holes under engine-like conditions.

$$\bar{\eta} = f(M, Tu, DR, \alpha, \frac{P}{D}, \frac{x}{D}, \frac{L}{D}) \tag{24}$$

$$\frac{\overline{h_f}}{h_0} = f(M, Tu, DR, \alpha, \frac{P}{D}, \frac{x}{D}, \frac{L}{D}) \quad (25)$$

Where $M$ is the blowing ratio, which the ratio of the injection mass flux to the free stream mass flux, $M = U_c\ \rho_c / U_G\ \rho_G$. $Tu$ is the free stream turbulence intensity. $DR$ is the density ratio between the coolant and the free stream gas. α is the inclination angle of the cooling hole, which is the angle between surface plane and the axis of the cooling hole. $P/D$ is the spanwise pitch, the distance between holes within a row, normalized on the hole diameter. $x/D$ is the streamwise position normalized on the hole diameter, which is the distance from the hole measured in number of hole diameters. $L/D$ is the cooling hole length normalized on the hole diameter. These developed correlations are quite complex and complicated to use but are quite accurate for the flow conditions.

Colban et al [31] developed a correlation for spanwise-averaged effectiveness for shaped holes from a large collection of data sets. This correlations was developed for shaped holes for the following ranges: $M$ =0.2-2.5, $t/P$ =0.31-0.65, $AR/(M\ P/D)$=0.17-1.17:

$$\bar{\eta} = f(M, \frac{P}{D}, \frac{x}{D}, AR, \frac{t}{D}) \quad (26)$$

Figure 4 shows the geometry and parameters of shaped-hole injection. The spanwise-averaged correlation approaches a value of $t/P$ as $x$ approaches zero. This corresponds to having the local effectiveness value of unity over the width, t of the hole and zero elsewhere. This is equivalent to having a step-function for the spanwise distribution which is true when there is no coolant warming.

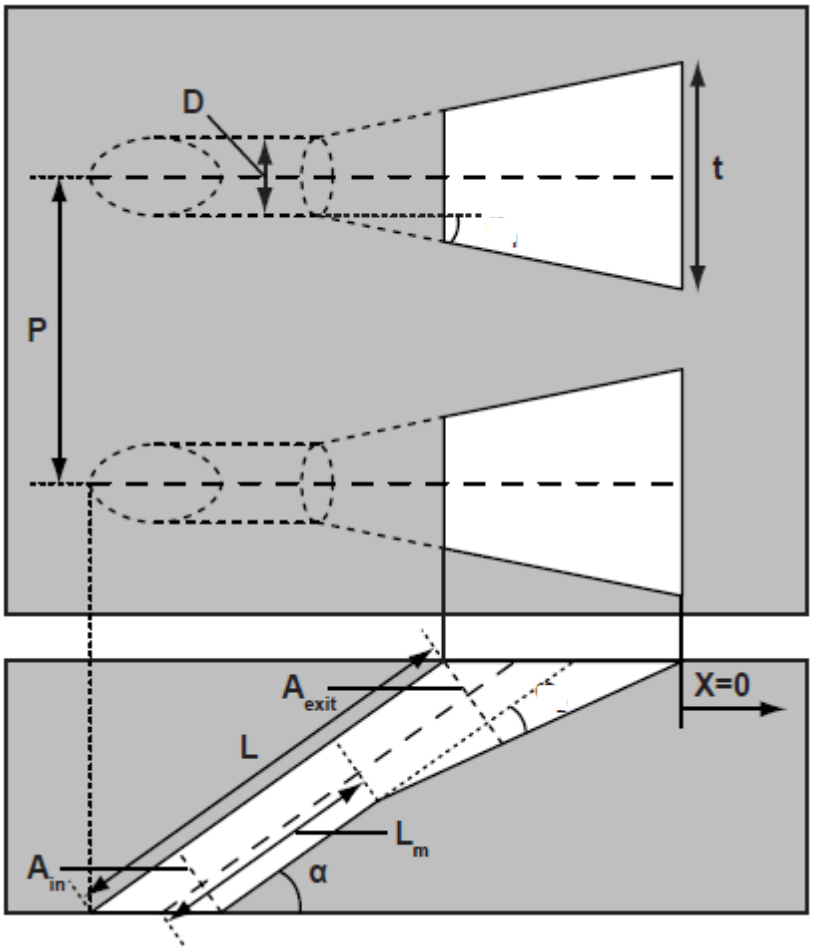


**Figure 4. Illustration of shaped hole geometrical parameters as given by Colban et al. [31].**

## 1.8 Numerical Studies on Film-Cooling

There are many numerical studies available for film-cooling. The numerical prediction of film-cooled flows with reasonable results is limited to the recovery region. Habte and Yavuzkurt [32] reported that Reynolds Averaged Navier-Stokes (RANS) models under predict mixing in the near field resulting in higher effectiveness values. RANS models varied in their results, ranging from under predicting effectiveness by as much as 80% to over predicting by as much as 200%. The best performance was by the k-ε model, which stayed around 20% error for its effectiveness prediction. Figure 5 is a plot of these results. It can be seen that predicted values do not become reasonable until $x/D > 3$. The location $x/D > 3$ represents the exit region of near the field of

the injection site and entrance into the wake region. Azzi and Lakehal [33] showed that RANS models under predict lateral spreading of the film. The result of such studies is that RANS models are inadequate in the near field. This currently holds true for all turbulence models.

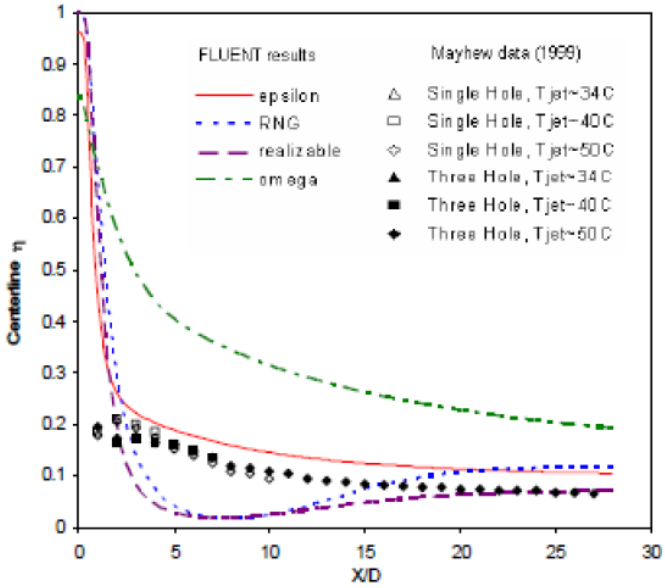


**Figure 5. Computational Results for Centerline Adiabatic Effectiveness Habte & Yavuzkurt [32]and Experimental Data Mayhew et al [34].**

Figure 6 is of a typical film-cooling geometry for a first stage blade likely to be seen in a high temperature gas turbine. Turbulence models would be very unreliable for predicting such a flow because by the time one film jet leaves the near field and settles down in the wake region, the solution enters the near field of the next cooling hole. It should also be noted that a first stage vane would have even more film-cooling holes on the airfoil surface than shown in Figure 6, as it is a half stage closer to the combustor outlet, which would cause larger discrepancies in predictions of film effectiveness and heat transfer coefficient augmentation for film-cooled flows solved using turbulence models. As flow geometries become more complicated, prediction of flow and the blade temperature becomes very complex, and currently cannot be accurately performed by using just CFD due to turbulence models not being able to predict the near field of film cooling jets as investigated by Foroutan and Yavuzkurt [35].

Different turbulence models for film cooling were investigated by Garg [36]. The k-ω, q-ω, and zero-equation Baldwin-Lomax models were investigated. It was found that k-ω agreed best with experimental data. Ma et al. [37] simulated cooling flow on a transonic squealer tip with both experimentation and CFD. They compared the Spalart-Allmaras model and the k-ω Shear Stress Transport (SST) model and found that the k-ω SST was more capable of capturing the flow physics and better matched the experimental data. Yan et al. [38] investigated film cooling effects on a squealer-winglet tip and found that the k-ω model was the best option of the models studied. Montomoli et al. [39] successfully implemented the k-ω SST model and matched experimental data for film cooling with high $P/D$. Jiang et al. [40] simulated two rows with multiple holes using the k-ω SST model. They found that curvature and rotational effects significantly affect jet behavior and therefore film cooling effectiveness. Jiang et al. [41] did a mesh sensitivity analysis on RANS simulations of film cooling. They found that for cylindrical holes and shaped holes up to a blowing ratio of $M = 0.5$, that the models matched the film cooling effectiveness well. They also found that the heat transfer spatial variations did not match well, nor did the film cooling effectiveness for high blowing ratio.

Yuan et al. [42] used large-eddy simulation (LES) to model flow of a round jet in cross-flow. They found good agreement between the LES results and experimentation and found the LES could reproduce the large-scale structures of the flow. Muppidi and Mahesh [43] used direct numerical simulation of a jet in cross-flow. They found good agreement with experimental data and that the near-hole region is far from turbulent equilibrium. They also compared results from RANS simulations and did not find good agreement. LES and DNS are not feasible to use on a film cooled turbine blade, despite the high accuracy. Turbine blades can have hundreds of holes and complex geometries which are difficult for these methods [44] [45].

Bryant and Rutledge [46] used CFD to model conjugate heat transfer in a film cooled turbine blade to determine relative significance of cooling modes. The different modes investigated on the blade with shaped cooling holes were convection along the cooling holes, convection in the plenum, and convection from the film cooling. It was found that the most significant was the film cooling, then the convection along cooling holes, and least significant was the convection from the plenum. It is concluded that designers must optimize all the forms in conjunction with each other as the overall heat transfer is determined by the balance of the three.

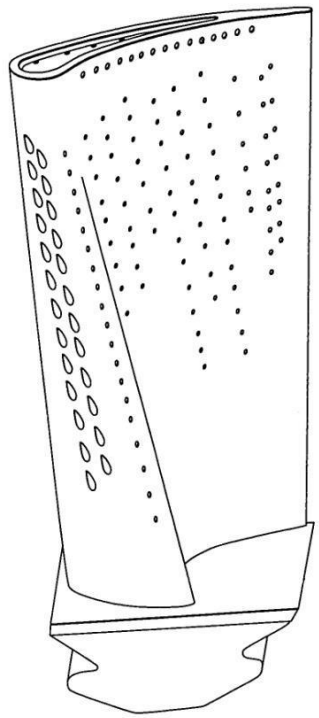

**Figure 6. Typical Film-Cooling Configuration for a First Stage Blade [47].**

The literature shows multiple gaps in the predictive capabilities of conventional Computational Fluid Dynamics (CFD) programs for film-cooled flows. Turbulence models are incapable of providing satisfactory results in the near field, making them unacceptable for predicting wall temperatures for early-stage turbine vanes and blades. Turbulence models have fallen behind experimental findings. An alternative method for solving near-field film-cooled flows is needed. Further, any film-cooled airfoil should be solved in a manner that includes the effect of blade conduction on the baseline convection in the solution, successfully resolving conjugate effects. Given the low thermal conductivity of the blade material and thermal barrier coatings, such effects can have a large influence on the predicted final wall temperature. The ICHT-ROFM method allows the implementation of experimental data or correlations. To accurately implement the 3D ICHT-ROFM method 2D correlations are needed for both the adiabatic effectiveness and

the heat transfer coefficient augmentation. While several spanwise-averaged correlations exist in the published literature, 2D correlations are nonexistent.

Recent work has been done by Chen et al. [48] on a diffusion-based model for prediction of spanwise distribution of effectiveness for shaped holes. They found that the model they developed includes the effects of diffusion and convective transportation in the spanwise directions. The spanwise convection was modeled to be dominated by vortex entrainment. The model was found to be accurate with errors between 8% and 14% when compared to experimental data.

Chen et al. [6] also developed an integral model for jet trajectories based on the conservation of mass and conservation of momentum applied to jets in cross flow. They identified and modeled the major factors in jet deflection to be the drag force and jet ingestion. They also modeled the changing jet size by modeling the growth of the counter rotating vortex pair. Their model more closely matched experimental data than existing correlations, for varied values of blowing ratio, density ratio, and turbulence intensity.

The previous two studies were synthesized into a single model by Chen et al. [49] for 2D effectiveness predictions. Again, the model was found to have errors between 8% and 14%.

## 1.9 Conclusions and Motivations

Experiments to obtain heat transfer coefficient data are performed with either constant temperature or constant heat flux on the surface on which the data is collected. Therefore, the effects of the conduction within the surface are not taken into account within the data. This data is then used in conventional techniques by turbine blade designers to calculate the temperature field within the blade. A turbine blade has several modes of heat transfer occurring, including external convection, internal conduction, and internal convection. In realistic cases, neither the temperature nor the heat flux are constant in time or uniform in space. This method usually yields erroneous predictions of the temperature fields. An efficient method to incorporate conjugate heat transfer effects is needed to improve turbine blade design.

The survey of literature on numerical studies of film cooling revealed that current two-equation turbulent models are inadequate in predicting the mixing and spreading of the film cooling jet. This leads to poor temperature predictions within the film cooled solid. More complex simulation methods, such as hybrid RANS-LES, are very computationally large and time consuming with results that still yield erroneous temperature fields. Applying these methods to a fully coupled conjugate solution increases the grid size and therefore the computational time, while still having the issues with predicting the fluid flow. An alternate method that can loosely couple the fluid and solid domains, while accurately predicting the heat transfer coefficients is required to accurately predict the solid temperature field in a timely manner.

A method to be able to accurately predict 3D temperature distributions in the blades is needed. The present study deals with this need using numerical techniques of Iterative Conjugate Heat Transfer with Reduced Order Film Modeling (ICHT-ROFM) while implementing 2D correlations for film-cooling effectiveness and heat-transfer coefficient augmentation ($h_f/h_0$). This technique simplifies the computational process and takes into account the effect of the thermal resistance of blade metal on the temperature distribution. 2D correlations are necessary for accurate 3D temperature fields which are necessary for the calculations of thermal stresses within the film cooled solid.

## 1.10 Objectives

The current research focuses on extending Iterative Conjugate Heat Transfer (ICHT) with Reduced Order Film Modeling (ROFM) to three-dimensional temperature predictions for single and multiple row film cooled solids.

The main objectives of this study are as follows:

1. **Develop 2D Correlations**
    a. **Develop correlations for film cooling effectiveness and heat transfer coefficient augmentation for single row of cylindrical cooling holes including the effects of relevant parameters**. In this study the available spanwise-averaged correlations for film-cooling effectiveness and heat transfer coefficient are extended to 2D form as a function of axial and spanwise directions. These correlations are functions of the blowing ratio ($M$), streamwise inclination angle (α), spanwise pitch ($P/D$), and the density ratio $DR$.
    b. **Develop correlations for film cooling effectiveness and heat transfer coefficient augmentation for single row of shaped holes including the effects of relevant parameters**. The correlations have been expanded to include effects of shaped holes, including the area ratio ($AR$) and break through width ($t/D$)
    c. **Develop correlations for film cooling effectiveness and heat transfer coefficient augmentation for compound holes including the effects of relevant parameters.** The correlations have been expanded to include effects of compound holes via the spanwise injection angle ($\beta$).

2. **Develop a superposition technique for film cooling parameters**
    a. Develop a superposition method for interaction within a row of holes
    b. Develop a superposition method for interactions between multiple rows of film cooling holes

3. **Investigate and develop a method that includes near-hole effects**
    a. Investigate effects of internal cooling of the solid within the injection hole
    b. Develop method for dealing with hole boundary conditions using ICHT-ROFM

## Chapter 2: Development of 2D Correlations

### 2.1 Overview of Effects of Relevant Geometry and Fluid Flow Parameters

There are many parameters that affect cooling performance. The following discusses many of those parameters as well as their impact. The primary parameters will be the focus of this work. The momentum flux ratio and the secondary parameters are not included in this work. At the time of the correlation development, these parameters were not well incorporated into published correlations. Figure 7 shows the geometric parameters of a shaped cooling hole and Figure 8 shows compound angle injection hole.

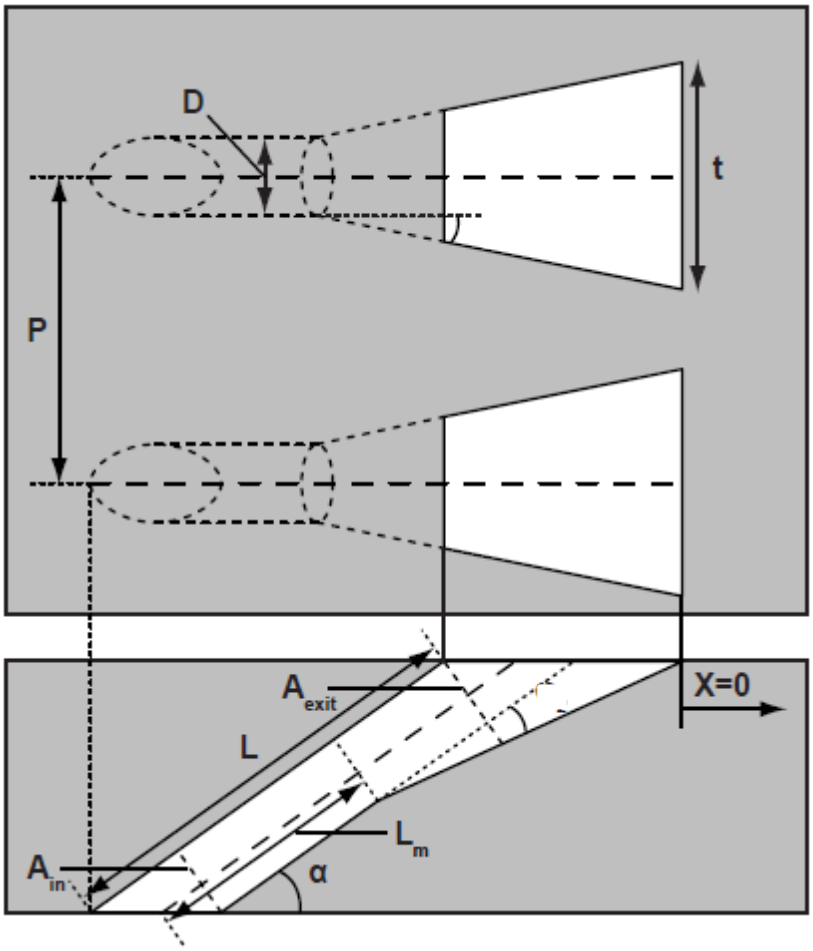


**Figure 7. Illustration of shaped hole geometrical parameters as given by Colban et al. [31].**

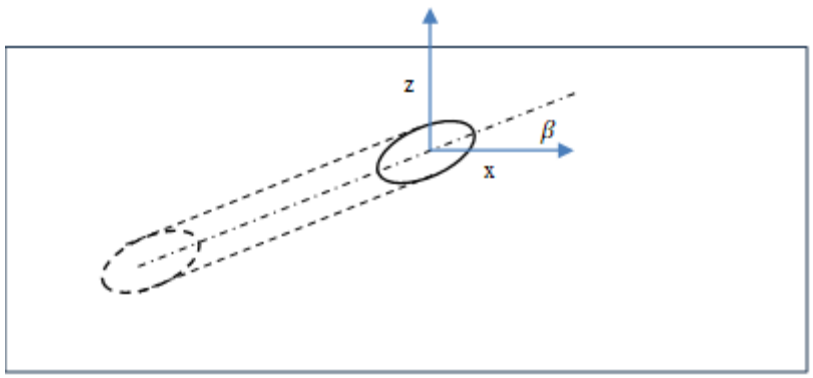


**Figure 8. Hole geometry for compound injection.**

Primary:

Blowing ratio ($M = U_c\rho_c/U_G\rho_G$): The ratio of the mass flux from the cooling hole to the mass flux of the mainstream flow. The jet remains attached for low blowing rations, detaches and reattaches for jets with moderate blowing ratios and detaches for high blowing ratios. Strongly affects decay rate of effectiveness and the location of peak heat transfer coefficient augmentation.

Momentum flux ratio ($I = {U_c}^2\rho_c/{U_G}^2\rho_G$): The ratio of the momentum flux from the cooling hole to the momentum flux of the mainstream flow.

Inclination injection angle ($\alpha$): A primary parameter that determines jet behavior (attached or detached). Affects decay rate of effectiveness.

Compound injection angle ($\beta$): Projected angle between hole axis and streamwise direction. Moves peak values of effectiveness from the hole centerline. Causes asymmetry in the spanwise profile of effectiveness and heat transfer coefficient augmentation.

Turbulence intensity ($Tu\%$): Higher values of freestream turbulence leads to increased mixing which causes the centerline effectiveness to decay faster and increased spreading of effectiveness.

Spanwise pitch ($P/D$): Distance between holes within a row normalized on the hole diameter. Limits width of jet; small values lead to stronger jet interactions and increased shear and mixing between the cooling jets.

Breakthrough width ($t/D$): The width of the hole at the exit normalized on the hole diameter. The width of the hole at the exit used for shaped holes directly affects the spreading of the effectiveness at the hole exit.

Area Ratio ($AR = A_{exit}/A_{hole}$): The area of the hole exit normalized on the area of the cylindrical cooling line. Values larger than unity correspond to a diffuser. Used for shaped holes. Directly affects the exit blowing ratio, changing the effective exit velocity for a given flow rate of coolant.

Surface curvature: Affects boundary layer formation and attachment due to pressure gradients along the surface.

Surface roughness: Average of surface height variations. Increased surface roughness usually leads to increase mixing, shear, and heat transfer.

Secondary:

Density ratio ($DR$), Spanwise pitch ($P/D$), Hole length ($L/D$), Free Stream Pressure Oscillations, Streamwise pitch, Approach boundary layer, Location of hole, Mainstream Mach number, Unsteadiness in freestream, Rotation of mainstream flow due to turbine blade rotation around the turbine shaft.

## 2.2 Transport of Thermal Energy from a Point Source

A simple model for film cooling injection is a point source in uniform steady flow. The transport equation can be simplified to only diffusion and advection. A schematic of this phenomenon can be seen in Figure 9.

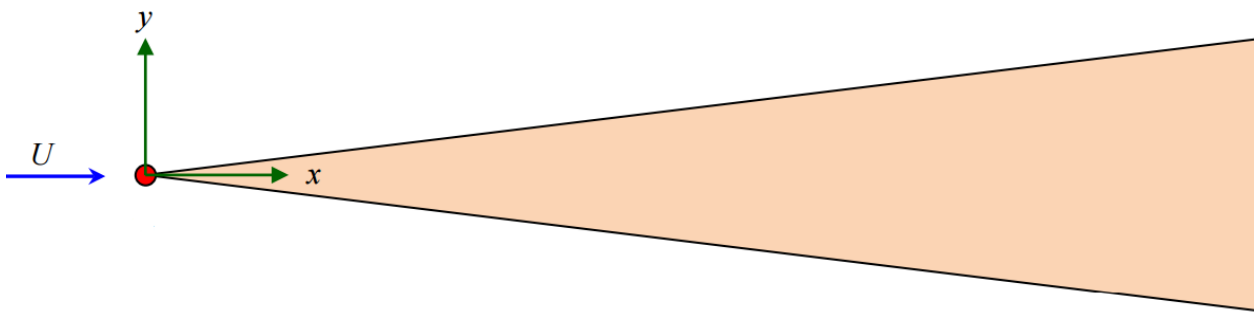


**Figure 9. Diffusion from a point source in uniform flow.**

The transport of a conserved scalar (ϕ) is given by the equation below:

$$\frac{\partial \phi}{\partial t} + \nabla \cdot (\vec{u}\phi) = \nabla \cdot (\Gamma \nabla \phi) + S_\phi \qquad (27)$$

The transient term, $\frac{\partial \phi}{\partial t}$, which is the local rate of change of $\phi$, accounts for the accumulation of $\phi$ within the differential control volume.

The convection term, $\nabla \cdot (\vec{u}\phi)$, accounts for the transport of $\phi$ due to the existing velocity field.

The diffusion term, $\nabla \cdot (\Gamma \nabla \phi)$, accounts for the transport of $\phi$ due to its local gradients where $\Gamma$ is the diffusion coefficient of $\phi$.

The source term, $S_\phi$, accounts for change of $\phi$ due to the creation or removal of $\phi$ in the differential control volume.

### Diffusion equation for the transport of thermal energy ($\phi = \rho C_p \theta$)

For this simple case of a point source in cross flow, the flow vector's, $\vec{u}$, only component is in the x direction. The simplified equation in Cartesian coordinates can be seen in Equation (28) in which $\theta$ is a function of $\theta(x, y, z, t)$. Where x is the streamwise direction, y is the vertical direction, and z is the spanwise direction.

$$\frac{d}{dt}(\rho C_p \theta) = -\frac{d}{dx}(\rho U C_p \theta) + \frac{d}{dx}\left(k_x \frac{d\theta}{dx}\right) + \frac{d}{dy}\left(k_y \frac{d\theta}{dy}\right) + \frac{d}{dz}\left(k_z \frac{d\theta}{dz}\right) \qquad (28)$$

Further assumptions can be used to simplify this equation are as follows:

- Steady source
- $U$ is constant in both space and time
- Advection dominates the x-direction
- $k_y$ and $k_z$ vary only in the x-direction

After applying these assumptions, Equations (28) becomes Equation (29) where $\theta$ is a function of $\theta(x, y, z)$.

$$\rho U C_p \frac{d\theta}{dx} = k_y \frac{d^2\theta}{dy^2} + k_z \frac{d^2\theta}{dz^2} \tag{29}$$

This differential equation needs five boundary conditions. Two of the boundary conditions are that far away in the $y$ and $z$ directions, the temperature is not affected by the point source and the dimensionless temperature is zero.

$$\text{As } y \to \infty,\ \theta \to 0 \tag{30}$$

$$\text{As } z \to \infty,\ \theta \to 0 \tag{31}$$

The next two boundary conditions stem from symmetric about the x axis such that the temperature is at a extremum at the x-axis.

$$\left.\frac{d\theta}{dy}\right|_{y=0} = 0 \tag{32}$$

$$\left.\frac{d\theta}{dz}\right|_{z=0} = 0 \tag{33}$$

The last boundary condition is the application of conservation of energy. Since the source and the flow are steady and do not vary with time, there can be no accumulation of energy at any given x location. Thus, the total energy flowing across the plane at any given $x$ location, must be equal to that emitted from the source.

$$\iint \rho U C_p \theta \, dz dy = Q \tag{34}$$

The resulting solution to the transport equation is

$$\theta = \frac{Q}{2\pi\rho U C_p \sigma_y(x)\sigma_z(x)} \exp\left\{-\frac{1}{2}\left[\left(\frac{y}{\sigma_y(x)}\right)^2 + \left(\frac{z}{\sigma_z(x)}\right)^2\right]\right\} \tag{35}$$

Where $\sigma_y(x)$ and $\sigma_z(x)$ are correlations for the vertical and spanwise spreading and $Q$ is the energy entering the system from the point source.

To make the model better match the physical reality of injection, the vertical and horizontal position of the jet must be accounted for. A simple way to account for this is to move the location of the source as the jet changes location. This is done by including an offset to the vertical and spanwise location that is only function of the streamwise coordinate. The functions $H_y(x)$ and $H_z(x)$ are introduced to offset the vertical and spanwise directions respectively.

$$\theta = \frac{Q}{2\pi\rho U C_p \sigma_y(x)\sigma_z(x)} \exp\left\{-\frac{1}{2}\left[\left(\frac{y - H_y(x)}{\sigma_y(x)}\right)^2 + \left(\frac{z - H_z(x)}{\sigma_z(x)}\right)^2\right]\right\} \tag{36}$$

The film cooling effectiveness is measured using an adiabatic wall. This can be modeled by placing a virtual source that mirrors the vertical location. This ensures that there is no heat transfer over the wall by returning any thermal energy that is transferred over the wall by the real source. This results in the following equation.

$$\begin{aligned}\theta = \frac{Q}{2\pi\rho U C_p \sigma_y(x)\sigma_z(x)} \Bigg( &\exp\left\{-\frac{1}{2}\left[\left(\frac{y - H_y(x)}{\sigma_y(x)}\right)^2 + \left(\frac{z - H_z(x)}{\sigma_z(x)}\right)^2\right]\right\} \\ &+ \exp\left\{-\frac{1}{2}\left[\left(\frac{y + H_y(x)}{\sigma_y(x)}\right)^2 + \left(\frac{z - H_z(x)}{\sigma_z(x)}\right)^2\right]\right\}\Bigg)\end{aligned} \tag{37}$$

The adiabatic effectiveness is measured at the wall, which on the plane corresponds to a vertical coordinate of zero. This simplifies the equation to only two dimensions and $\theta$ is now a function of $\theta(x, z)$ along the specified surface.

$$\theta = \frac{Q}{\pi\rho U C_p \sigma_y(x)\sigma_z(x)} \exp\left\{-\frac{1}{2}\left[\left(\frac{H_y(x)}{\sigma_y(x)}\right)^2 + \left(\frac{z - H_z(x)}{\sigma_z(x)}\right)^2\right]\right\} \tag{38}$$

Correlations for the vertical and spanwise spreading and the vertical and horizontal source location are needed. This can be further simplified and reduce the number of correlations by combining all the terms that are only a function of the streamwise coordinate.

$$\theta = \theta_{CL}(x) \exp\left\{-\frac{1}{2}\left[\left(\frac{z - H_z(x)}{\sigma_z(x)}\right)^2\right]\right\} \tag{39}$$

This results in a distribution that has a centerline function that is only a function of the streamwise coordinate, and a spanwise distribution that is Gaussian with a peak location and spanwise spreading that are functions of the streamwise coordinate only. $\theta_{CL}(x)$, $\sigma_z(x)$, and $H_z(x)$ are spatially only functions of streamwise position $x$, but are also dependent on the film cooling parameters outlined in the previous section.

In the case of compound injection, there is advection in the in the spanwise z-direction and the assumption that the transportation in the spanwise direction is only by diffusion is violated. This is not investigated in this work.

## 2.3 Correlation for Adiabatic Film Cooling Effectiveness

The correlation developed is based on the developed model that showed the film-cooling effectiveness profile was Gaussian in the spanwise direction, centered on the cooling hole exit for inline injection. This was observed by Ramsey et al. [50] for single hole cooling. To examine how the assumed spanwise distribution can capture the film-cooling effectiveness profile, raw data from Lawson [51] is compared with a summation of normal distributions. As seen in Figure 10, the Gaussian distribution can capture much of the behavior in the spanwise direction. Using the assumed Gaussian profile, existing spanwise-averaged correlations can be used to develop 2D correlations. The developed 2D correlations are formulated to satisfy the spanwise-averaged correlations on which they are based.

The effectiveness at any location $(x, z)$ or any normalized location $(\tilde{x}, \tilde{z})$ where $\tilde{x} = x/D$ and $\tilde{z} = z/D$ is given by:

$$\eta(\tilde{x},\tilde{z}) = \eta_{CL}(\tilde{x})\, e^{-\frac{(\tilde{z}-\tilde{z}_h)^2}{2\sigma(\tilde{x})^2}} \tag{40}$$

This 2D correlation contains two main parameters: $\eta_{CL}(\tilde{x})$, which is the centerline effectiveness, and $\sigma(\tilde{x})$, the transverse width of effectiveness and is evaluated at a constant source location of $H_z(x) = \tilde{z}_h$, where $\tilde{z}_h$ is the normalized hole location. For inline injection, the point source will not need to be moved as it is assumed the maximum effectiveness will be in line with hole location. Equation (40) can be spanwise-averaged, and the result compared with spanwise-averaged correlations given by Baldauf et al. [23] to determine the parameters $\eta_{CL}(\tilde{x})$ and $\sigma(\tilde{x})$.

Assuming that for a row of holes, the transverse distribution of effectiveness can be approximated by a sum of Gaussian distributions, then, for H holes:

$$\begin{aligned}\eta_{total}(\tilde{x},\tilde{z}) &= \eta_1(\tilde{x},\tilde{z}) + \eta_2(\tilde{x},\tilde{z}) + \cdots + \eta_H(\tilde{x},\tilde{z}) = \sum_{h=1}^{H} \eta_h(\tilde{x},\tilde{z}) \\ &= \sum_{h=1}^{H} \eta_{CL_h}(\tilde{x})\, e^{-\frac{(\tilde{z}-\tilde{z}_h)^2}{2\sigma_h(\tilde{x})^2}}\end{aligned} \tag{41}$$

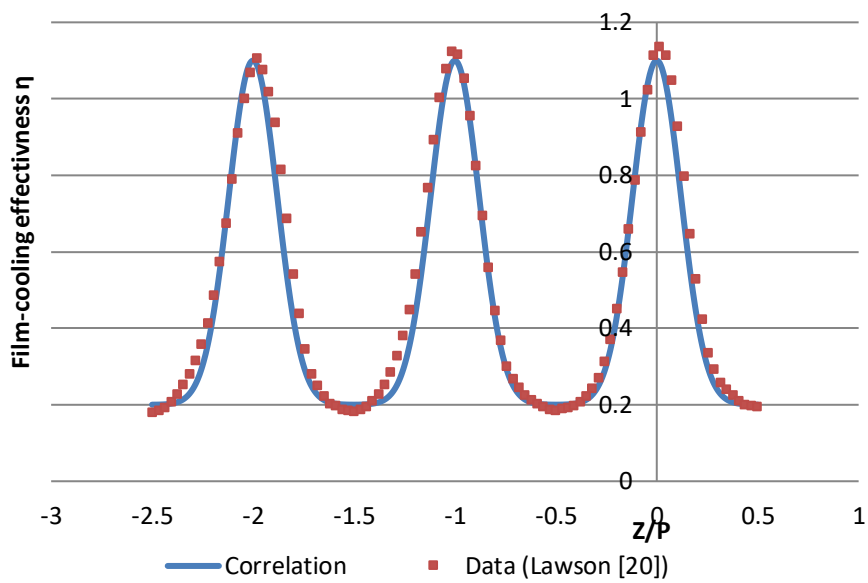


**Figure 10. Spanwise profile of film-cooling effectiveness at downstream location (x/D=0.981).**

The spanwise-average of Equation (41) is:

$$\bar{\eta}(\tilde{x}) = \frac{1}{\Delta z}\int_{\Delta z/2}^{\Delta z/2}\sum_{h=1}^{H}\eta_{CL_h}(\tilde{x})\, e^{-\frac{(\tilde{z}-\tilde{z}_h)^2}{2\sigma_h(\tilde{x})^2}}\, d\tilde{z} \tag{42}$$

If $\Delta z$ is an order of magnitude larger than the lateral spreading of the effectiveness, then the local effectiveness should approach zero as the z approaches $\Delta z$. Thus, the spanwise-average simplifies to:

$$\bar{\eta}(\tilde{x}) = \frac{1}{\Delta z}\sum_{h=1}^{H}\sqrt{2\pi}\,\eta_{CL_h}(\tilde{x})\,\sigma_h(\tilde{x}) \tag{43}$$

Baldauf et al. [23] has presented a correlation for a single hole in cross-flow. The streamwise scaling for this correlation is a function of the spanwise pitch, which is undefined for a single hole. The correlation presented appears to begin before the hole, since the value of the spanwise-averaged effectiveness begins at zero and increases from there. Baldauf et al. [23] claim this is due to high levels of entrainment.

According to Baldauf et al. [23], the spanwise-averaged effectiveness for a single hole should be given by the following:

$$\bar{\eta} = \eta_p^*\eta^*\frac{DR^{0.9/\frac{P}{D}}}{sin(\alpha)} \tag{44}$$

Where $\eta^*$and $\eta_p^*$ are the normalized effectiveness and peak effectiveness as given in Baldauf et al. [23] and

$$f = \frac{DR^{0.9/\frac{P}{D}}}{sin(\alpha)} \tag{45}$$

Assuming a Gaussian distribution in the lateral direction, then the spanwise-averaged effectiveness is obtained as follows:

$$\bar{\eta} = \eta_p^*\eta^* f = \frac{\sqrt{2\pi}}{\Delta\tilde{z}}\eta_{CL}(\tilde{x})\,\sigma(\tilde{x}) \tag{46}$$

Where $\eta_{CL}(\tilde{x})$ is the centerline effectiveness, and $\sigma(\tilde{x})$ is the standard deviation of the lateral spreading, given by the following equations:

$$\eta_{CL}(\tilde{x}) = \frac{C_1}{[1 + (\frac{\xi}{\xi_0})^{(a^*+b^*)c^*}]^m} \tag{47}$$

$$\sigma(\tilde{x}) = \frac{C_2(\frac{\xi}{\xi_0})^{a^*}}{[1 + (\frac{\xi}{\xi_0})^{(a^*+b^*)c^*}]^n} \tag{48}$$

and

$$C_1 C_2 = \frac{\eta_p^* \eta_0 f \Delta\tilde{z}}{\sqrt{2\pi}} \tag{49}$$

Where $\xi$ is the downstream distance parameter defined by Baldauf et al. [23] as $\xi = 4xP/\pi D^2 M$. If $\xi_0, a^*, b^*, c^*$, which are correlations coefficients, match those given in Baldauf et al. [23], then the spanwise-averaged correlation developed by Baldauf et al. [23] will automatically be satisfied by the distribution assumed. The other correlation coefficients introduced here are $C_1, C_2, m, n$ and need to be determined.

In the far-field, the spanwise spreading grows asymptotically, such that the spanwise variations become negligible compared to the axial decay of effectiveness. This assumption appears to be true for a row of holes in which the local effectiveness becomes uniform by 20-30D downstream. From the study by Yuen [17] on single holes, this assumption also seems to be true for single holes. This assumption gives values of 'n' and 'm' as follows:

$$n = \frac{a^*}{(a^* + b^*)c^*} \tag{50}$$

$$m = \frac{b^*}{(a^* + b^*)c^*} \tag{51}$$

Assuming that the value of the local effectiveness is approximately unity at the hole, then $C_1$ and $C_2$ will be:

$$C_1 = 1 \tag{52}$$

$$C_2 = \frac{\eta_p^* \eta_0 f \Delta\tilde{z}}{\sqrt{2\pi}} \tag{53}$$

Where $\Delta\tilde{z} = \Delta z/D$ and $\Delta z$ is the lateral distance over which the effectiveness was integrated. For the geometry used by Baldauf et al. [23], the width of the test section is 44D. Based on these, the final distribution for local effectiveness is given as:

$$\eta(\tilde{x},\tilde{z}) = \eta_{CL}(\tilde{x})\, e^{-\frac{(\tilde{z}-\tilde{z}_h)^2}{2\sigma(\tilde{x})^2}} \tag{54}$$

Resulting in centerline effectiveness and lateral spreading as follows:

$$\eta_{CL}(\tilde{x}) = \frac{1}{[1 + (\frac{\xi}{\xi_0})^{(a^*+b^*)c^*}]^{\frac{b^*}{(a^*+b^*)c^*}}} \tag{55}$$

and

$$\sigma(\tilde{x}) = \frac{\frac{\eta_p^* \eta_0 f \Delta\tilde{z}}{\sqrt{2\pi}} (\frac{\xi}{\xi_0})^{a^*}}{[1 + (\frac{\xi}{\xi_0})^{(a^*+b^*)c^*}]^{\frac{a^*}{(a^*+b^*)c^*}}} \tag{56}$$

For large values of x or ξ, it can be shown that both the centerline effectiveness approximately and the spanwise-average also behave like $\bar{\eta} \sim 1/\xi^{b^*}$. This agrees with the idea that in the far-field, the effectiveness is no longer strongly affected by the lateral spreading but rather is dominated by the decay of the centerline effectiveness. This is consistent with the asymptotic growth in the lateral spreading and that in the far-field, the effectiveness is more uniform. Figure 11 shows the resulting film cooling effectiveness for singular row of holes.

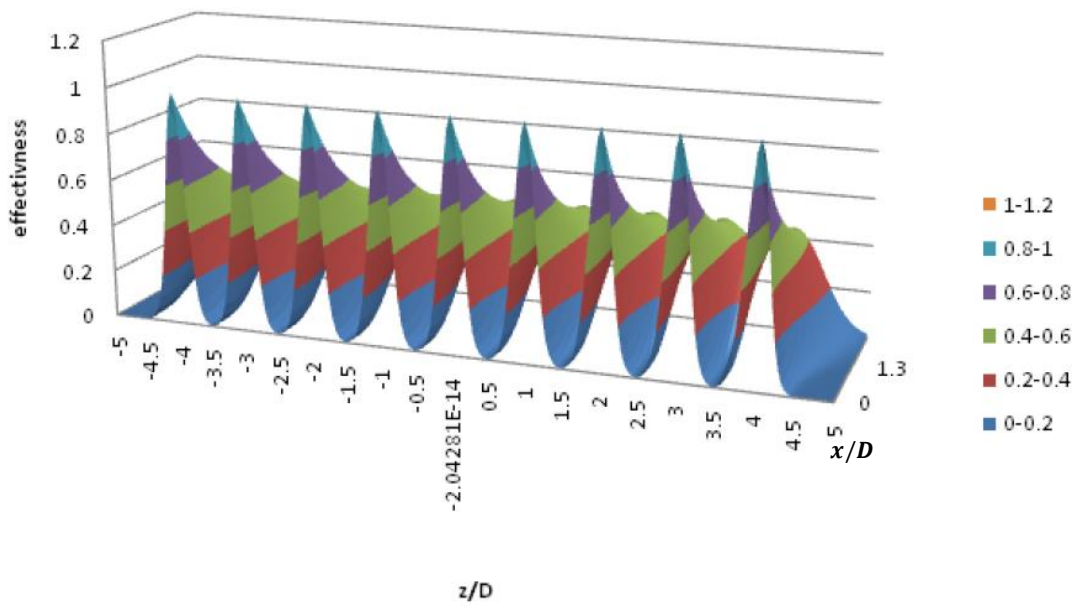


**Figure 11. Resulting effectiveness profiles at the hole location across the span of a row of film cooling holes.**

## 2.4 Correlation for Heat Transfer Coefficient augmentation

The spanwise profile of the heat transfer coefficient augmentation can vary significantly depending on the coolant jet behavior and streamwise location. Baldauf et al. [9] discuss and display the different phenomenon that cause changes in the heat transfer coefficient in Figure 12.

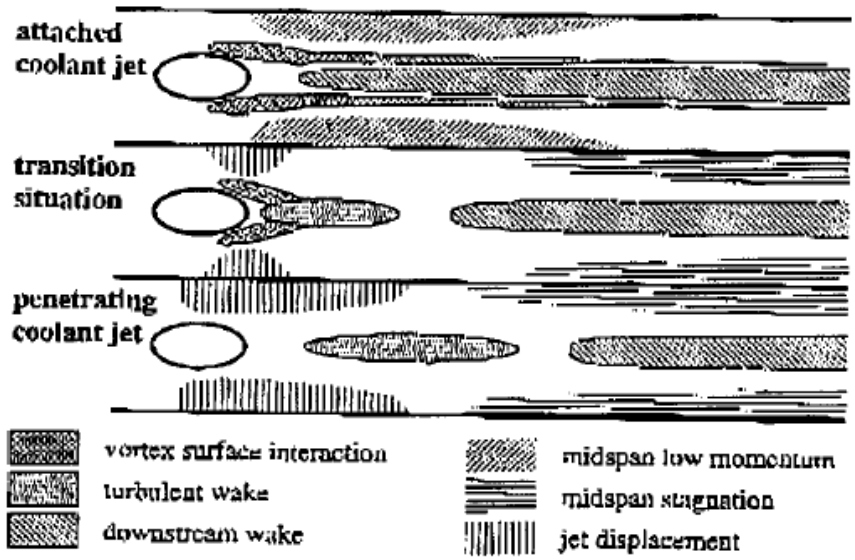


**Figure 12. Physical phenomenon that cause heat-transfer coefficient augmentation (hf/h0) according to Baldauf et al. [9].**

Figure 13 shows an assumed transverse (spanwise) distribution of the heat transfer coefficient augmentation ($h_f/h_0$) around a singular film-cooling hole with an attached cooling coolant jet. There are three functions that describe this assumed Gaussian distribution.

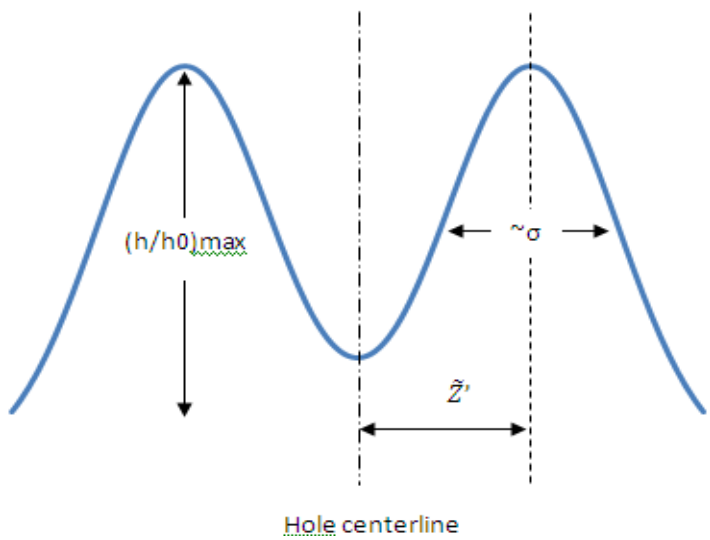


**Figure 13. Assumed transverse distribution of heat transfer coefficient augmentation for a film-cooling hole.**

The first, $\tilde{Z}' = z'/D$, describes the dimensionless distance from the hole to the location of the maximum heat transfer coefficient enhancement. The second is the value of the maximum heat transfer coefficient augmentation ($(h_f/h_0)_{max}$), and the third is the dimensionless standard deviation around the maximum heat transfer coefficient augmentation locations. All three are functions of the flow parameters and the streamwise location. Ammari et al. [52] found high heat transfer coefficients at the edge of the jet for low blowing ratios ($M < 0.5$) due to high shear between the main flow and the jet. Large values were on the centerline in the vicinity of the hole for intermediate ($M = 0.5 - 1.0$) and large blowing ratios ($M > 1$). This occurs because when the jet detaches, the hot mainstream fluid is entrained beneath the jet, causing an increase in heat transfer. This is consistent with the findings of Yuen et al. [18] on their study with a single hole. Therefore, for a single hole $\tilde{Z}'$ would be a strong function of $M$ and would effectively go to zero for high blowing ratios ($M > 1$). This is shown in Figure 14.

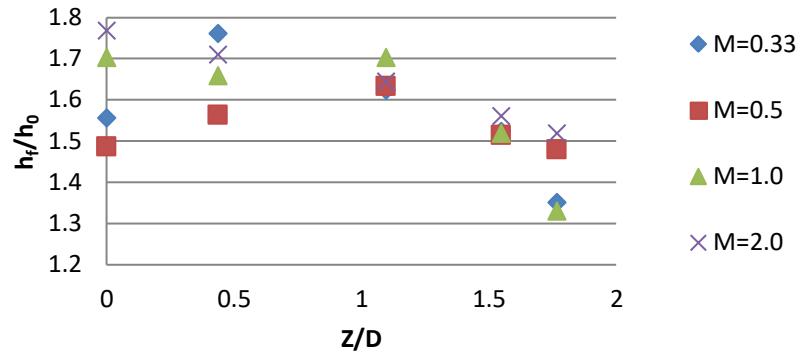


**Figure 14. Spanwise distribution of heat transfer coefficient augmentation at x/d=2 for a single hole in cross-flow with α=30° data from Yu et al [53].**

For a single row of holes, Yu et al. [53] discuss the transverse distribution shown in Figure 15 at two transverse locations. The centerline is at the same transverse location as the center of one of the cooling holes, and the mid-span is the axial line midway between centers of two cooling holes. They discuss two competing factors that influence the magnitude of the heat transfer coefficient. First, the increasing boundary layer thickness due to the injection causes an increase in convective resistance. The second is the enhanced flow shear induced by the jet interaction with the mainstream flow, resulting in an increase in heat transfer. The centerline is expected to be more impacted by the first factor. Meanwhile, between the holes, the second factor would greatly dominate, causing an increased heat transfer. Therefore, the maximum heat-transfer coefficient augmentation should occur at mid-span between the holes or at $\widetilde{Z}'$ of approximately $P/2D$.This is shown in Figure 12, taken from Baldauf et al. [9].

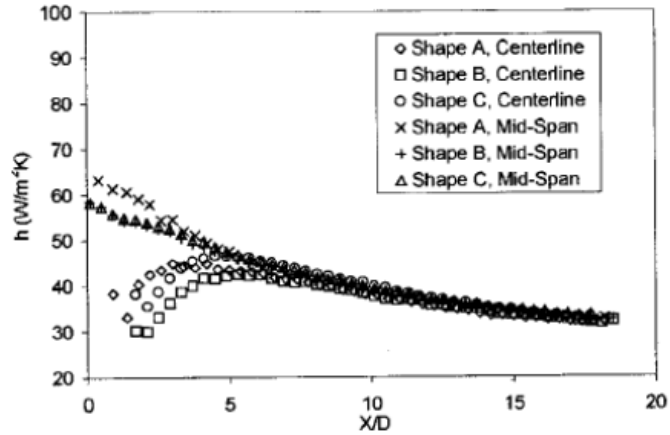


(*a*) **M=0.5**

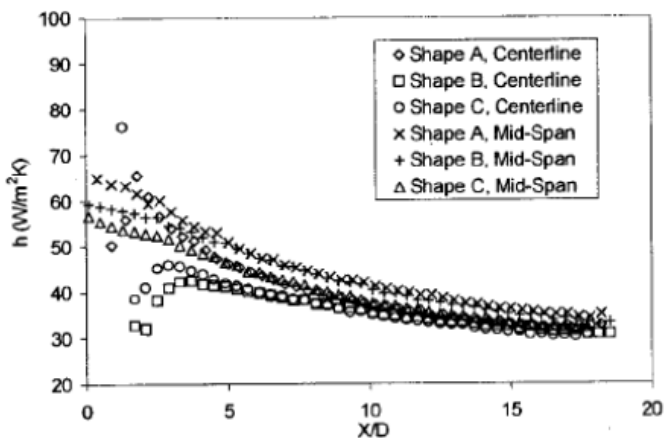


(*b*) **M=1.0**

**Figure 15. Centerline and mid-span streamwise distribution of heat transfer coefficient for a single row of holes, P/D=3 for 3 different shaped holes as presented by Yu et al. [53].**

For a single hole, the assumed $\left(\frac{\overline{h_f}}{h_0}\right)$ distribution is:

$$\left(\frac{\overline{h_f}}{h_0}\right) - 1 = \frac{1}{\Delta z}\int_{-\frac{\Delta z}{2}}^{\frac{\Delta z}{2}}\left[\left(\frac{h_f}{h_0}\right)_{max} - 1\right] e^{-\frac{(\tilde{z}-\tilde{z}')^2}{2\sigma^2}} dz \tag{57}$$

For $N$ similar holes:

$$\left(\overline{\frac{h_f}{h_0}}\right) - 1 = \frac{N}{\Delta z}\int_{-\frac{\Delta z}{2}}^{\frac{\Delta z}{2}}\left[\left(\frac{h_f}{h_0}\right)_{max} - 1\right] e^{-\frac{(\tilde{z}-\tilde{z}')^2}{2\sigma^2}} dz \tag{58}$$

The spanwise-average is developed by a similar approach used in Equations (42) and (43), which yields:

$$\left(\overline{\frac{h_f}{h_0}}\right) - 1 = \frac{N}{\Delta z\sqrt{2\pi}}\left[\left(\frac{h_f}{h_0}\right)_{max} - 1\right]\sigma \tag{59}$$

The same correlation for the spreading can be used and is given in Equation (56). This can be shown to be valid for the model developed in Section 2.2 by equating the convection from a surface to the conduction through the fluid at the surface.

$$-k_f \left.\frac{dT}{dy}\right|_{y=surface} = h_f(T_G - T_W) \tag{60}$$

Solving Equation (60) it can be shown that the convective heat transfer coefficient is proportional to the derivative of the dimensionless temperature with respect to $y$.

$$h_f \sim \left.\frac{d\theta}{dy}\right|_{y=surface} \tag{61}$$

Substituting in Equation (36) and evaluating the derivative in Equation (69) it can be shown that the convective heat transfer coefficient is proportional to a function of x, g(x), and a spatial variation in the z direction.

$$h_f \sim g(x)\exp\left\{-\frac{1}{2}\left[\left(\frac{z - H_z(x)}{\sigma_z(x)}\right)^2\right]\right\} \tag{62}$$

Normalizing on the base line heat transfer coefficient, which would be expected to be only a function of the streamwise direction yields the following relationship.

$$\left(\frac{h_f}{h_0}\right) \sim \frac{g(x)}{h_0(x)} \exp\left\{-\frac{1}{2}\left[\left(\frac{z - H_z(x)}{\sigma_z(x)}\right)^2\right]\right\} \tag{63}$$

Therefore, for this simple case, it can be seen that the spanwise variation of the heat transfer coefficient augmentation should have a similar behavior to the spanwise spreading of the adiabatic film cooling effectiveness.

With this supposition, the following equation is obtained:

$$\left(\frac{h_f}{h_0}\right)_{max} = \left(\left(\overline{\frac{h_f}{h_0}}\right) - 1\right) \frac{\Delta z \sqrt{2\pi}}{N\sigma(x)} + 1 \tag{64}$$

Where $\left(\overline{\frac{h_f}{h_0}}\right)$ is given by Baldauf et al. [9] or any other appropriate spanwise-averaged correlation. Figure 16 shows the resulting heat transfer coefficient augmentation for a single hole.

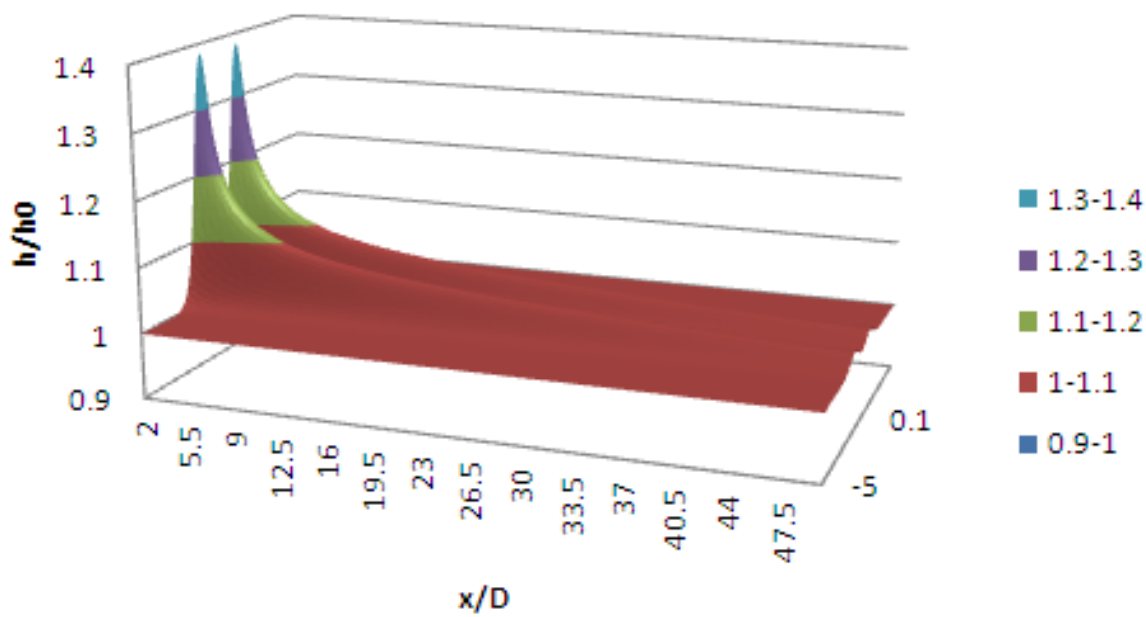


**Figure 16. Resulting heat transfer coefficient augmentation (hf/h0) distribution for a single hole with m=0.5, α=30$^0$ from correlations in the near hole region.**

## 2.5 Effects of Shaped Holes on Film Cooling Parameters

Shaped holes add two main geometric parameters as compared to cylindrical holes. The first is $t$, which is termed the breakthrough width of the hole since it is no longer simply equal to the injection tube diameter. The second is the area ratio ($AR$). Both of these parameters can be seen in Figure 17 as presented by Colban et al. [31].

Colban et al. [31] suggest that, at the hole breakthrough, the spanwise distribution of effectiveness is a step function with a value of unity over the hole and zero elsewhere, which is true without coolant warming. This assumption results in the spanwise-averaged correlation for effectiveness to approach a value of $t/P$ at the hole breakthrough location. This spanwise distribution should quickly become Gaussian due to mixing at the edges of the jet. This boundary condition is very different than that given by Baldauf et al. [23]. The Baldauf correlation began at a value of zero due to high entrainment. The spanwise spreading of the effectiveness should be modified to account for this effect, and the correlation proposed by Colban et al [31] is used to do this. This is done in the method proposed previously.

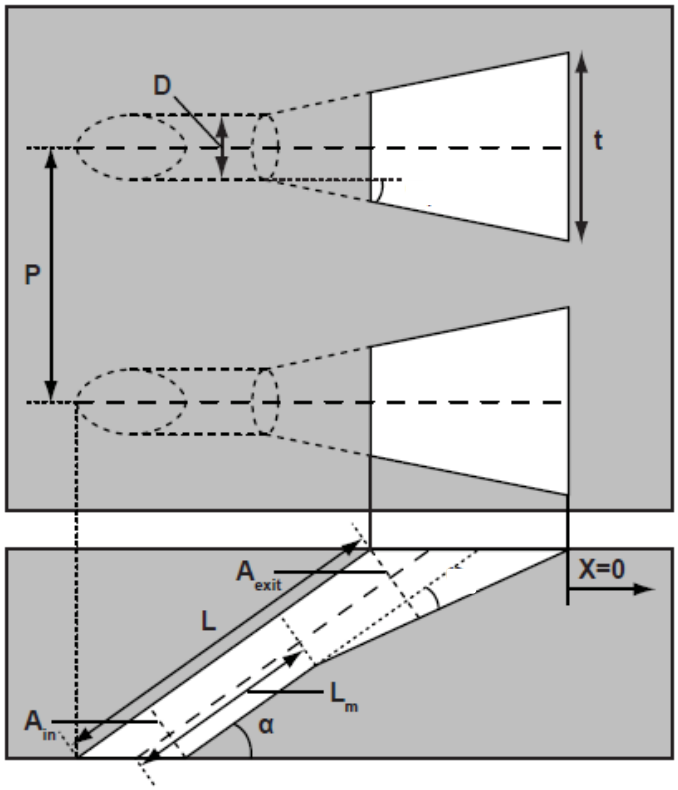


Figure 17. Illustration of shaped hole geometrical parameters as presented by Colban et al. [31].

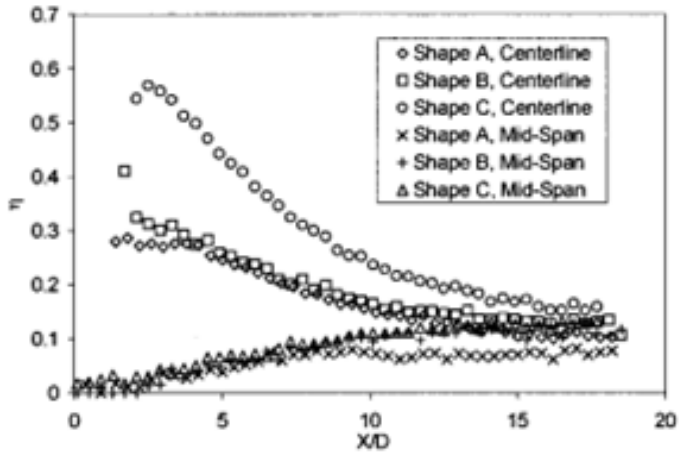


Figure 18. Centerline and midline effectiveness for shaped holes from Yu et al [53].

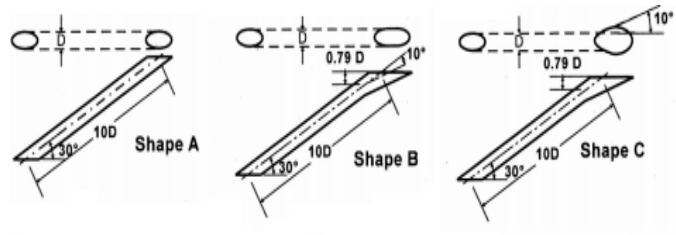


**Figure 19. Different shaped holes used by Yu et al [53].**

Figure 18 and Figure 19 show that the centerline effectiveness decays less quickly in the streamwise direction with diffuser shaped holes (B and C) than with a cylindrical hole (A). This is expected because the coolant is more uniformly distributed over the surface. The mid-span and centerline effectiveness values approach similar values in streamwise direction more quickly for the diffuser shaped holes due to more uniform spreading of the coolant. At around 12-15 hole diameters downstream, the effectiveness becomes more uniform in the spanwise direction due to the increased spreading of the jet.

To account for the shape of the hole, the streamwise blowing ratio is modified by the area ratio ($AR$). These modifications must "disappear" as the hole approaches a cylindrical shape. $M_{sh}$ is the modified blowing ratio to be used in the developed correlations. A power-law correlation is used to fit the data, given as:

$$M_{sh} = C_{sh1} AR^{C_{sh2}} M \tag{65}$$

Where $C_{sh1} AR^{C_{sh2}}$ approaches unity as the hole shape approaches that of a cylindrical hole. The function $C_{sh1} AR^{C_{sh2}}$ is determined such that the centerline correlation can predict the centerline effectiveness for shaped holes. $C_{sh1}$ must be unity so that the effect of the area ratio returns to unity for cylindrical holes, when AR=1, and $C_{sh2}$ was found to be 0.8762 from data from Yu et al. [53].

By applying the conservation of mass to the jet inlet and exit of the shape hole the following were obtained:

$$M_e = M/AR \tag{66}$$

and

$$U_e = U/AR \tag{67}$$

Where $M_e$ and $U_e$ are the blowing ratio and velocity ratio at the exit of the shaped hole, if the density does not change significantly along the hole length.

The heat-transfer coefficient augmentation correlation developed previously should be modified to use the exit mass flow rate. This is done to account for the shear at the edge of the jet is a function of the velocity difference and thus the exit mass flow rate. The location of maximum heat transfer coefficient is located at the edge of the hole; this is due to the low exit blowing ratio causing large shear at the edge of the hole. This agrees with the observations of Yuen et al. [18] and can be observed in the experimental data from Gritsch et al [25].

## 2.6 Effects of Compound Angle Holes on Film Cooling Parameters

For inline holes the maximum value of the adiabatic effectiveness was located on the hole centerline in the axial direction. The location and value of maximum heat transfer coefficient augmentation was assumed to be symmetric with respect to the hole centerline, which is not the case for compound angle holes. The locations of maximum effectiveness and heat transfer coefficient augmentation are functions of the compound angle and the streamwise position. A schematic of the location can be seen in Figure 20.

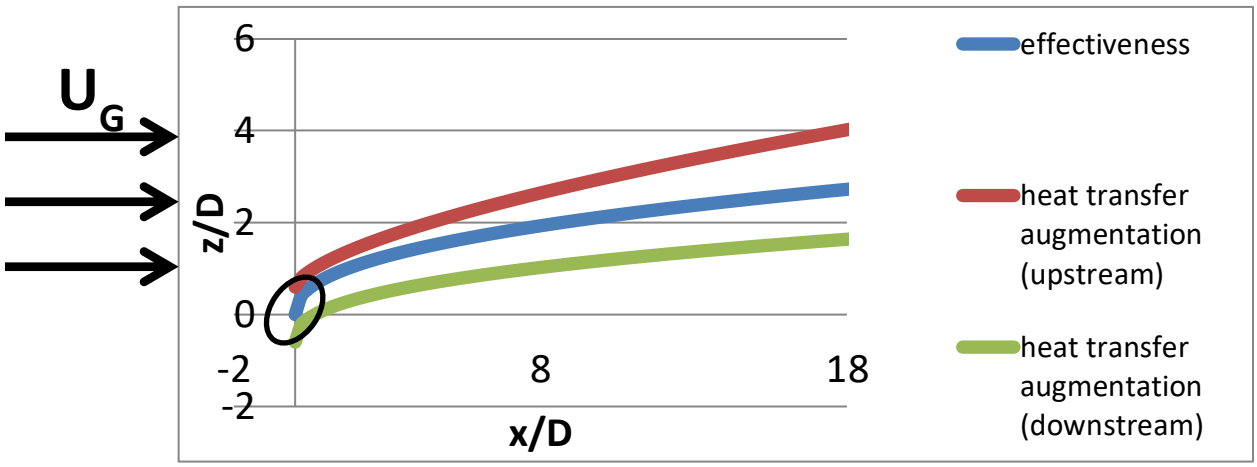


**Figure 20. Location of spanwise maximum heat transfer augmentation and film cooling effectiveness.**

The exposed upstream side of the jet, i.e., the side in the direction of the compound angle flow that is exposed to the mainstream flow, has a significantly higher heat transfer coefficient augmentation than that of the downstream side. This is due to the increased shear near the wall due to the mainstream and compound jet interaction. For compound angle holes, the jet exit flow was broken into streamwise and spanwise components using the injection angle ($\alpha$) and the compound injection angle ($\beta$). These are given by:

$$x_e = \cos(\alpha)\cos(\beta) \tag{68}$$

and

$$z_e = \cos(\alpha)\sin(\beta) \tag{69}$$

The blowing ratio at the exit in these directions is simply defined as:

$$M_{ex} = M_e \cos(\alpha) \cos(\beta) \tag{70}$$

and

$$M_{ez} = M_e \cos(\alpha) \sin(\beta) \tag{71}$$

The location of maximum effectiveness and heat transfer was determined by examining twelve experimental data sets of Mayhew et al. [34] and Aga and Abhari [54]. The cases are documented in Table 1.

**Table 1. Experimental cases used in the correlation development.**

| M | α | β | tu% | Source |
|---|---|---|---|---|
| 0.5 | 30 | 45 | 1 | Mayhew et al. [34] |
| 0.5 | 30 | 45 | 10 | Mayhew et al. [34] |
| 1 | 30 | 15 | 1 | Aga and Abhari [54] |
| 1 | 30 | 45 | 1 | Mayhew et al. [34] |
| 1 | 30 | 45 | 10 | Mayhew et al. [34] |
| 1 | 30 | 60 | 1 | Aga and Abhari [54] |
| 1 | 30 | 90 | 1 | Aga and Abhari [54] |
| 1.5 | 30 | 45 | 1 | Mayhew et al. [34] |
| 1.5 | 30 | 45 | 10 | Mayhew et al. [34] |
| 2 | 30 | 15 | 1 | Aga and Abhari [54] |
| 2 | 30 | 60 | 1 | Aga and Abhari [54] |
| 2 | 30 | 90 | 1 | Aga and Abhari [54] |

The location of maximum effectiveness was normalized on the spanwise exit blowing ratio, and the streamwise coordinate was normalized on the streamwise exit blowing ratio given in Equations (70) and (71). The normalized streamwise coordinate is $\frac{x/D}{M_{ex}}$ which is a simplified ratio of the Reynolds numbers $Re_x/Re_D$ The effectiveness is mass flow dependent and therefore a strong function of the exit mass flow rates, which determine how the effectiveness is transported. The result is given by Equation (72). The data along with the correlation results are shown in Figure 21. The correlation closely follows the data with a high $R^2 = 0.9284$. The average deviation of the correlation from the data was less than 8%. The correlation is of the form:

$$\frac{z_\eta^{'}/D}{M_{ez}} = C_{\eta 1}\left(\frac{x/D}{M_{ex}}\right)^{C_{\eta 2}} \tag{72}$$

Where $C_{\eta 1}$and $C_{\eta 2}$were found to be $C_{\eta 1} = .7479$ and $C_{\eta 2} = 0.42426$.

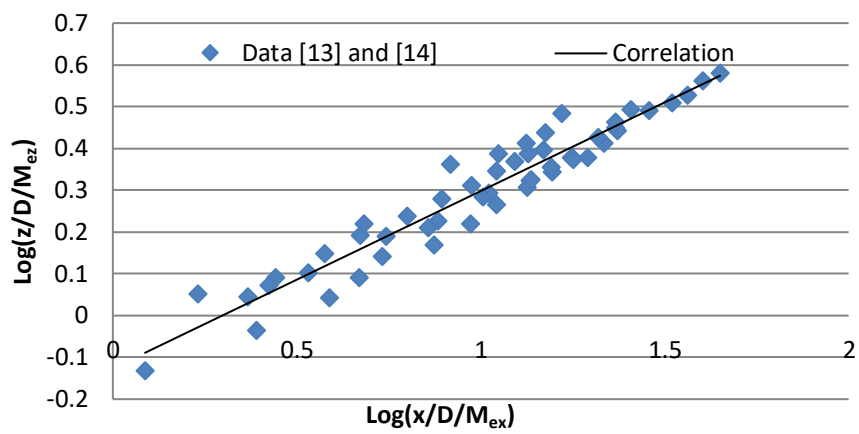


**Figure 21. Correlation for prediction of the location of maximum effectiveness and experimental data from Mayhew et al. [34] and Aga and Abhari [54] $r^2$=0.9284 for compound angle injection.**

The spanwise spreading of the effectiveness is affected by the breakthrough width which is a function of the injection angles. The intersection of the cylindrical hole and the plane of the flat plate forms an ellipse. The width of the ellipse can be used to approximate the breakthrough

width. The equation for the ellipse in radial coordinates can be directly related to the injection parameters and simplifies to the following:

$$\frac{t}{D} = \left[ sin\alpha \sqrt{(sin\beta)^2 + \left(\frac{cos\beta}{sin\alpha}\right)^2} \right]^{-1} \tag{73}$$

Similar methods were used to develop correlations for the heat transfer coefficient augmentation. The upstream side location of maximum heat transfer coefficient augmentation was normalized on the spanwise exit component given in Equation (74). The downstream location of maximum heat transfer coefficient augmentation was normalized to the spanwise exit blowing ratio given in Equation (75). The results can be seen in Figure 22 and Figure 23. The correlation for the location of the maximum heat transfer coefficient augmentation on the upstream side has a maximum variation from the data of $z/(Dz_e) = 0.9032$ and an average deviation of 10%. The downstream side heat transfer coefficient augmentation correlation has a maximum deviation of $z/(DM_{ez}) = 0.3826$ and average deviation of 16% from the data. Again, the correlations take the form:

$$\frac{z'_{hto}/D}{z_e} = C_{hto1}\left(\frac{x}{D}\right)^{C_{hto2}} \tag{74}$$

and

$$\frac{z'_{hti}/D}{M_{ez}} = C_{hti1}\left(\frac{x}{D}\right)^{C_{hti2}} \tag{75}$$

where $C_{hto1} = 1.9039$, $C_{hto2} = 0.4284$, $C_{hti1} = 0.6600$ and $C_{hti2} = 0.4008$.

The exponent of x/D ($C_{hto2}$) in Equation (74) is the highest, whereas the lowest value is for the downstream side heat transfer coefficient augmentation ($C_{hti2}$) in Equation (75). This agrees with the observations from the experimental data that the location of the upstream side heat transfer coefficient augmentation occurs farthest from the injection site, while the location of the downstream side heat transfer coefficient augmentation is the closest to the injection site.

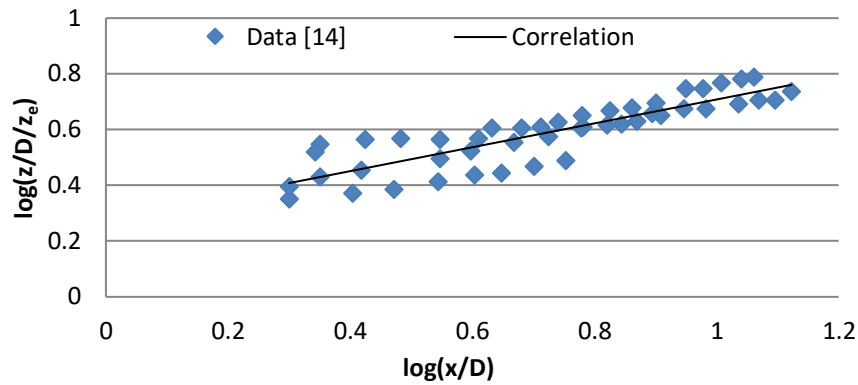


**Figure 22. Correlation prediction of streamwise side location of maximum heat transfer coefficient augmentation and experimental data from Aga and Abhari [54] $r^2$=0.7546.**

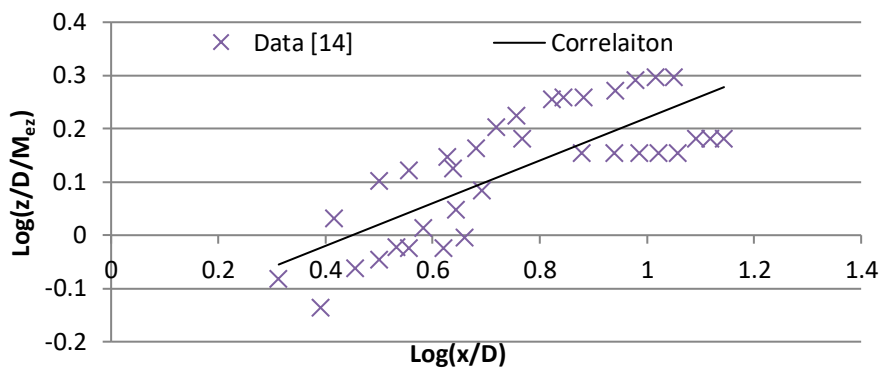


**Figure 23. Correlation prediction of downstream side location of maximum heat transfer coefficient augmentation and experimental data from Aga and Abhari [54], $r^2$=0.6086.**

The presented correlations are applicable for compound angles between $15^0$ and $60^0$ and potentially higher angles, as well as blowing ratios between 0.5 and 2. The correlations deviate from data at lower angles and blowing ratios. This is due to the fact that at low angles, the

location of maximum heat transfer shifts to a location of $z/D = 0.5$, for which the current correlation does not account. In the region very near the hole ($x/D < 2$), the location of maximum heat transfer is strongly affected by hole shape.

## 2.7 Development of Superposition Techniques for Multiple Rows of Holes

The adiabatic effectiveness is defined as:

$$\eta(x,z) = \frac{T_G - T(x,z)}{T_G - T_C} \tag{76}$$

Where $T_G$ the free-stream gas temperature, but this would be the local wall temperature if the cooling jet did not exist. For multiple rows of holes, the $T_G$ for downstream rows should be the temperature resulting from the upstream cooling holes. Thus, for the first row of cooling holes, effectiveness can be defined as in the literature.

$$\eta_1(x,z) = \frac{T_G - T_1(x,z)}{T_G - T_C} \tag{77}$$

For the second row of holes, the maximum local temperature difference is no longer between the freestream and the coolant, but the temperature resulting from the first row of coolant injection. $T_1(x,z)$ replaces $T_G$ as follows:

$$\eta_2(x,z) = \frac{T_1(x,z) - T_2(x,z)}{T_1(x,z) - T_C} \tag{78}$$

Where $T_1(x,z)$ is the local temperature resulting from the first row of injection, and $T_2(x,z)$ is the local temperature resulting from the first two rows of injection.

Solving both of these equations for the local temperature gives:

$$T_1(x,z) = T_G - (T_G - T_C)\eta_1(x,z) = \big(1 - \eta_1(x,z)\big)T_G - \eta_1(x,z)T_C$$

and

$$T_2(x,z) = T_1(x,z) - (T_1(x,z) - T_C)\eta_2(x,z) = \big(1 - \eta_2(x,z)\big)T_1(x,z) - \eta_2(x,z)T_C.$$

This recursive relationship will continue for subsequent rows. Substituting the previous row temperature (the first row) into the current row (the second row) one obtains:

$$T_2(x,z) = \big(1 - \eta_2(x,z)\big)[\big(1 - \eta_1(x,z)\big)T_G - \eta_1(x,z)T_C] - \eta_2(x,z)T_C,$$

Which simplifies to the following.

$$T_2(x,z) = T_G - \eta_1(x,z)(T_G - T_C) - \eta_2(x,z)\big(1 - \eta_1(x,z)\big)(T_G - T_C). \tag{79}$$

Then the overall effectiveness after the second row based on free-stream gas (if none of the cooling holes were present) is:

$$\eta(x,z) = \frac{T_G - T_2(x,z)}{T_G - T_C}.$$

Substituting the previous equation in for $T_2(x,z)$,

$$\eta(x,z) = \frac{T_G - [T_G - \eta_1(x,z)(T_G - T_C) - \eta_2(x,z)\big(1 - \eta_1(x,z)\big)(T_G - T_C)]}{T_G - T_C}$$

Which simplifies to

$$\eta(x,z) = \eta_1(x,z) + \eta_2(x,z)\big(1 - \eta_1(x,z)\big). \tag{80}$$

If a third row is added, the effectiveness becomes

$$\eta(x,z) = \eta_1(x,z) + \eta_2(x,z)\big(1 - \eta_1(x,z)\big) + \eta_3(x,z)\big(1 - \eta_1(x,z)\big)\big(1 - \eta_2(x,z)\big)$$

This recursive relationship simplifies to:

$$\eta(x,z) = \sum_{i=1}^{R} \eta_i(x,z) \prod_{j=0}^{i-1} (1 - \eta_j(x,z)) \tag{81}$$

with

$$\eta_0(x,y) = 0\,,$$

Where $\eta(x,z)$ is the effectiveness after $R^{th}$ row.

The span-wise averaged effectiveness for two rows of holes is given by

$$\bar{\eta}(x) = \int \eta(x,z)\,dz = \int \eta_1(x,z) + \eta_2(x,z)\big(1 - \eta_1(x,z)\big)\,dz = \int \eta_1(x,z)dz + \int \eta_2(x,z)\,dz - \int \eta_1(x,z)\eta_2(x,z)dz. \tag{82}$$

$$\bar{\eta}(x) = \bar{\eta}_1(x) + \bar{\eta}_2(x) - \int \eta_1(x,z)\eta_2(x,z)dz \tag{83}$$

It is important to note that

$$\int \eta_1(x,z)\eta_2(x,z)dz = \overline{\eta_1\eta_2}(x) \neq \bar{\eta}_1(x)\bar{\eta}_2(x)$$

$$\bar{\eta}(x) = \bar{\eta}_1(x) + \bar{\eta}_2(x) - \overline{\eta_1\eta_2}(x) \tag{84}$$

A superposition method for the adiabatic effectiveness developed was first proposed by Sellers [27] in 1963. This superposition method ignores the disturbances from upstream injection. This method has been applied to the spanwise-averaged effectiveness.

$$\bar{\eta}(x) = \bar{\eta}_1(x) + \bar{\eta}_2(x)(1 - \bar{\eta}_1(x)) \tag{85}$$

This application of the superposition method to spanwise-averaged effectiveness introduces errors from the approximation of the integral. Several different weighting methods have been proposed to improve approximation of this integral for this superposition method. Zhu et al. [28] have suggested a set of weighting functions for the superposition of film-cooling effectiveness.

$$\bar{\eta}(x) = A(x)\bar{\eta}_1(x) + B(x)\bar{\eta}_2(x)\big(1 - \bar{\eta}_1(x)\big) \tag{86}$$

Where $A(x)$ and $B(x)$are the weighting functions.

There will be errors from the spanwise-averaging of the effectiveness. This will remove the need for some of the weighting functions. Local weighting functions may need to be developed to account for the disturbances from upstream injections.

$$\eta(x,z) = \eta_1(x,z) + a(x,z)\eta_2(x,z)\big(1 - \eta_1(x,z)\big) \tag{87}$$

Where $a(x,z)$ is a weighting function and is a function of film-cooling parameters.

## 2.8 Superposition for Multiple Row Injection

The heat transfer coefficient for a film cooled surface is given in Equation (9). This coefficient is based on the temperature difference between the surface and the free stream. In developing a technique for superposition, it was assumed that the second row of holes is not exposed to the free stream flow, but the resulting flow from the previous row of film-cooling holes. Figure 24 shows a schematic for multiple rows of film-cooling holes. It is assumed that the second row experiences the local effective $h(\theta)$ from the upstream injection instead of the convective heat transfer coefficient without film-cooling. Substituting this heat-transfer coefficient from the first row, $h(\theta)_1$, into Equation (9) for the second row in place of $h_0$ results in Equation (88). Equation (89) results from simplifying Equation (88) after the substitution.

$$h(\theta)_2 = h(\theta)_1 \left(\frac{h_f}{h_0}\right)_2 (1 - \eta_2 \theta) \tag{88}$$

$$h(\theta)_2 = h_0 \left(\frac{h_f}{h_0}\right)_1 \left(\frac{h_f}{h_0}\right)_2 (1 - [\eta_1 + \eta_2(1 - \eta_1 \theta)]\theta) \tag{89}$$

A total heat transfer coefficient augmentation, $\left(\frac{h_f}{h_0}\right)_T$ and total film-cooling effectiveness, $\eta_T$ can be defined such that Equation (89) simplifies to the same form as Equation (9). This definition results in Equations (90) and (91) and is the basis for the superposition method developed.

$$\left(\frac{h_f}{h_0}\right)_T = \left(\frac{h_f}{h_0}\right)_1 \left(\frac{h_f}{h_0}\right)_2 \tag{90}$$

$$\eta_T = \eta_1 + \eta_2(1 - \eta_1 \theta) \tag{91}$$

This method results in superposition techniques for both the heat transfer coefficient augmentation and the film-cooling effectiveness. The superposition method for effectiveness is similar to that proposed by Sellers [27] for two-dimensional cooling gaps. The method developed in that study is extended to 3D film-cooling in the present study.

Figure 25 shows the film cooling effectiveness measured by Zhu et al [28] for two staggered rows seen in Figure 24. The resulting flow has significantly higher effectiveness than either of the individual rows. The staggered row configuration gives significantly better coverage than a single row. As the need for better coverage increases, more complicated cooling hole schematics arise. The method of superposition used here obtains multiple row film cooling effectiveness and heat transfer coefficients from single row properties.

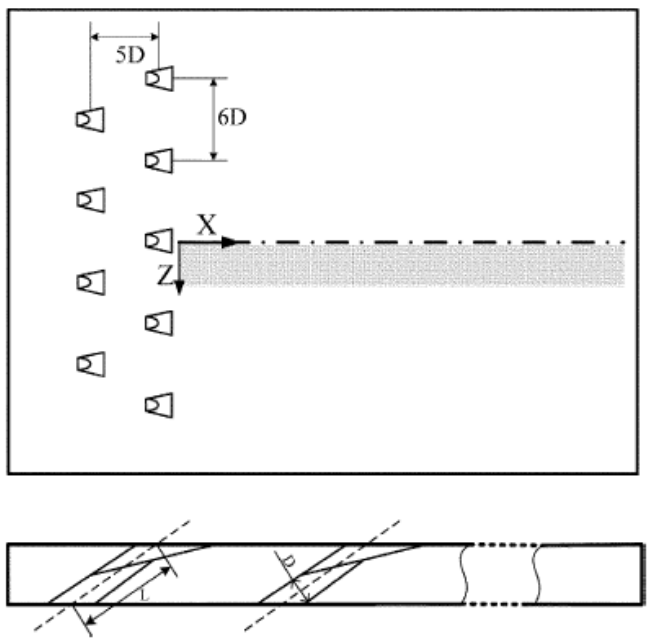


**Figure 24. Schematic of staggered rows of dustpan-shaped holes used by Zhu et al. [28].**

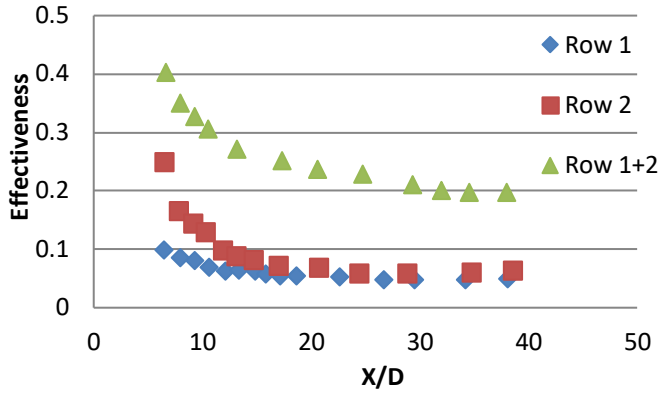


**Figure 25. Spanwise averaged results of experimental data from Zhu et al [28] for individual and two staggered rows M=1.5.**

# Chapter 3: Effects of Spanwise Variations and Coolant Warming on Film Cooling

The studies in this chapter are twofold. The first is to classify under what conditions, are 3D calculations needed and to quantify the error when compared to a similar 2D calculation. The second is to get a baseline for conditions in which coolant warming becomes significant and the level of errors caused by neglecting coolant warming. These concerns arose during the development of and integration of the ICHT-ROFM method to include the near-hole region and the effects of cooling within the cooling hole.

## 3.1 Effects of Biot number and spanwise variation in dimensionless temperature

The Biot number is the dimensionless ratio of the rate of convection from the surface of an object to the rate of conduction through the object and is shown below.

$$Bi = \frac{h\forall}{k_s A_{exposed}} \tag{92}$$

Where $h$ is the convective heat transfer coefficient between the object and the fluid surrounding it, $\forall$ is the volume of the object, $k_s$ is the conduction coefficient of the solid object, and $A_{exposed}$ is the surface area of the object exposed to the fluid. In general, for small Biot numbers, $Bi < 0.1$, the temperature variation within the object is less than 5%, and those variations can be ignored with minimal error.

For this analysis, a slice across the spanwise direction of the solid is analyzed. Streamwise conduction is being neglected in this analysis. A finite difference method was applied for the conduction in the solid for the geometry and boundary conditions shown in Figure 26. The goal is to obtain a general trend of the behavior of spanwise variation in film cooling parameters on the local temperatures and the spanwise-average temperature.

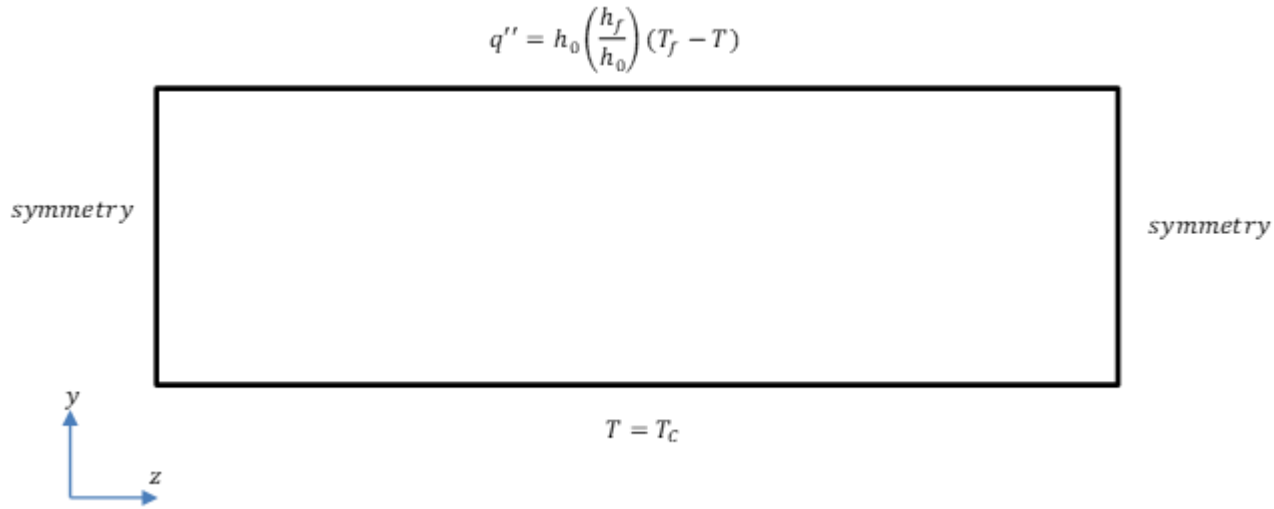


**Figure 26. Solid domain and applied boundary conditions for spanwise variation investigation.**

The applied film-cooling parameters correspond to those in the low temperature case investigation as specified in Table 2. The width analyzed is one spanwise pitch of a film cooling hole. The streamwise location is just downstream of the cooling hole ($x/D = 1.85$). The conductivity of the solid is varied such that the Biot numbers range between $10^{-5}$ to $10^{3}$ when based on the plate thickness. Three plate thickness are investigated, corresponding to $L_C/D = 4,8,16$. This analysis was repeated, but with applying the spanwise-averaged film-cooling parameters.

Table 2. Flow conditions for low temperature difference.

| **BOUNDARY CONDITIONS** | |
|---|---|
| Injection angle $\alpha=30^0$ | |
| Diameter of hole **D** | **10mm** |
| Mainstream gas velocity, $\mathbf{V_G}$ | **13m/s** |
| Mainstream temperature, $\mathbf{T_G}$ | **300K** |
| Free stream turbulence, **Tu %** | **2.7 %** |
| Coolant Temperature **Tc** | **280K** |
| Blowing Ratio **M** | 0.5 |
| **Material Properties** | |
| Material of Plate | Composite |
| Conductivity Composite **k** | 1.5 W/mK |

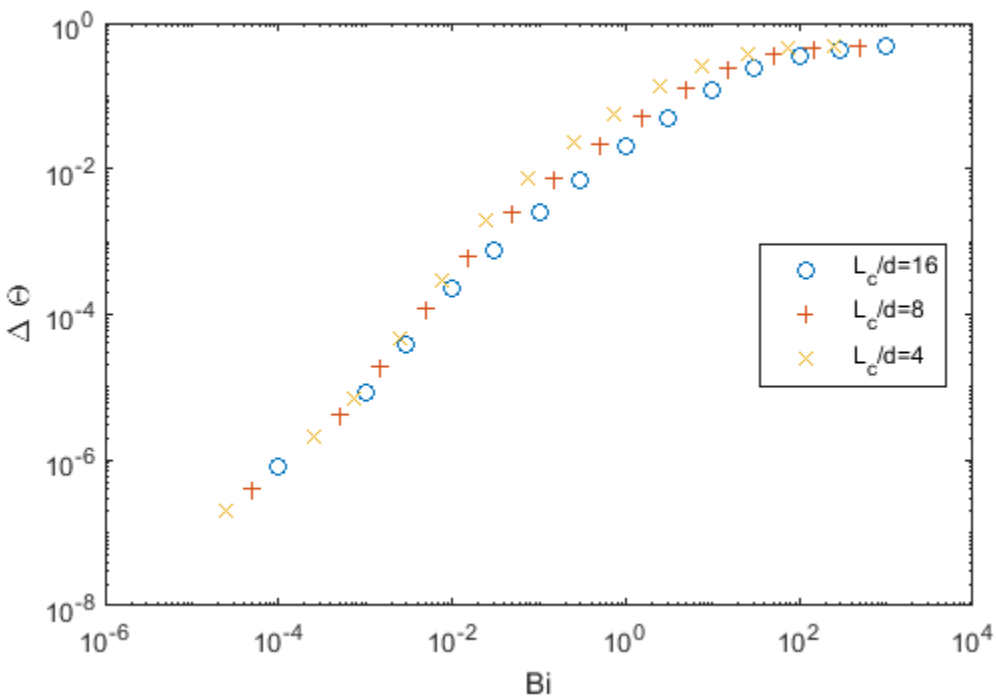


Figure 27 Spanwise temperature variation versus local Bi.

Figure 27 shows the dimensionless peak-to-peak variation of temperature along the spanwise $z$ direction for the given streamwise position, $x$, $(x/D = 1.85)$ for various relative thicknesses as a function of the Biot number. There is larger variation between aspect ratios Biot numbers

between $10^{-2}$ and 10, with about 30% relative difference in the magnitude of maximum temperature variations. Agreement between aspect ratios is better at low Bi and high Bi. In this region of low Bi, conduction in the plate is dominant, as such the classic definition of Bi is appropriate as the characteristic length is that over which the conduction occurs. The conduction occurs through the plate and is dominated by the temperature difference between the plate and the gas. At higher Bi, there is variation between the aspect ratios, this is because local temperature variations become more important as Bi increases. The thickness of the plate is no longer a good approximation of the conductive length scale.

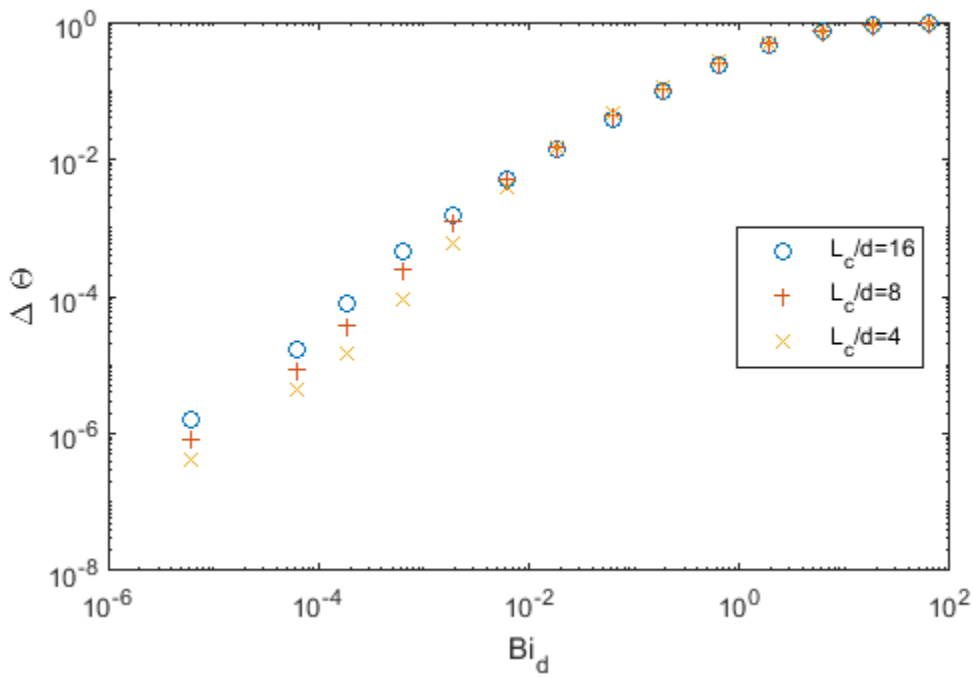


**Figure 28 Spanwise temperature variation versus local $Bi_D$.**

The Biot number in this Figure 28 is based on the characteristic length of the hole diameter. This was chosen because at the higher Bi, the conduction is dominated by the local variations in surface temperatures. These variations are due to the local values of heat transfer augmentation and film cooling effectiveness which vary with position normalized on the hole diameter. As such, the characteristic distance for local conduction is the hole diameter. There is very good

agreement over the various aspect ratios at higher Bi as this is the appropriate length scale for the local conduction. For extremely high Bi, the variations approach the driving temperature difference ($T_G$ and $T_C$), this is approaching the adiabatic case, so the near hole temperature should approach the coolant temperature and the midspan, at which there is minimal film coverage, should approach the gas temperature.

There is poor agreement with this length scale in the region of small Bi. As discussed previously, the appropriate length scale is this region should be the plate thickness. Variations between aspect ratios are significant in lower Bi numbers. These variations are not important since the level of spanwise temperature variation in this range of Bi numbers is extremely small. The variations between the aspect ratio becomes negligible at around $Bi_d * \frac{L_c}{d} > 0.1$ which corresponds to $Bi > 0.1$ when based on the characteristic length of the plate thickness. The temperature variations begin to be dominated by local conduction and the hole diameter should be used as the conductive length scale.

When $Bi_d \approx 1$, the spanwise temperature variations begin to become significant, on the order of 10's of percent of the total temperature difference for this cooling hole configuration and flow conditions. Knowing the material properties of the material, an estimate of the convection coefficient can be made, and a local Stanton number can be calculated from an appropriate correlation. This can be used to estimate the region in which there is expected to be significant spanwise temperature variations.

The next analysis compares two different methods applied to the same cases. Both approaches use the geometry and boundary conditions shown in Figure 26. The first uses the developed two-dimensional correlation for film cooling parameters to calculate three-dimensional temperature distributions. The spanwise-averaged temperature for this case is calculated and nondimensionalized on the driving temperature, $T_G - T_C$. The second uses one-dimensional, spanwise averaged, correlations for film cooling parameters to calculate the 2D temperature distribution, which would not vary in the spanwise direction. The ratio of the dimensionless temperatures of these two methods, $\bar{\theta}_{3D}/\bar{\theta}_{2D}$, would give insight to the errors that occur from the spanwise-average simplification.

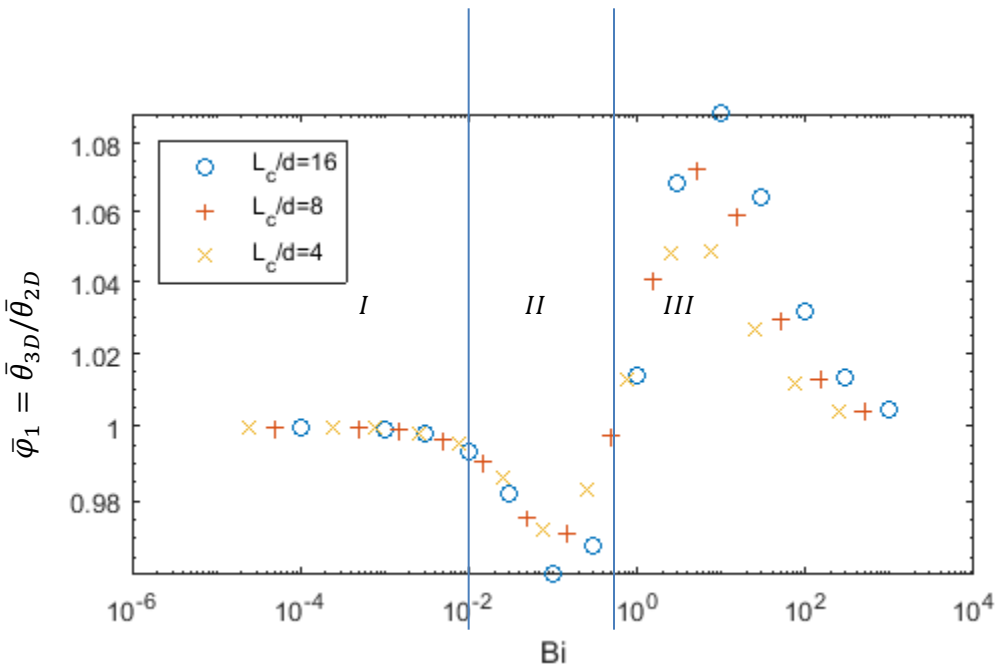


**Figure 29: Spanwise-averaged temperature ratio versus Bi.**

Figure 29 shows the ratio of the dimensionless spanwise-average temperature for the two methods. A value of $\bar{\varphi}_1 > 1$ corresponds to the spanwise-varied case resulting in a higher spanwise-averaged temperature than that of the spanwise-averaged case.

Figure 29 can be broken into three primary regions.

I: Bi less than $10^{-2}$. The ratio between the two methods is near unity. This is because the system is conduction dominated and spanwise-averaged non-conjugate is sufficient.

II: Bi=$10^{-2}$- $10^{-0.5}$, The spanwise averaged case overestimates temperature. The collocation of lower heat transfer augmentation and high effectiveness that causes lower temperatures. Since the system is still conduction dominated, the low temperature regions dominate.

III: Bi over $10^{-0.5}$. The spanwise averaged case underestimates the temperature. This is due to the fact that there is a lack of collocation of the effectiveness and heat transfer augmentation, there are regions of high heat transfer augmentation but low effectiveness that drive up local temperature. These effects are detrimental when the system is convection dominated, in that the temperature is under predicted when using a spanwise averaged analysis.

The peak difference is 5-9%, after which the ratio returns to 1 as $Bi$ increases further and as it approaches adiabatic conditions. The wall temperature approaches the adiabatic wall temperature, since the spanwise-average adiabatic effectiveness is the same between the two cases, the temperatures of the two cases approach the same value.

According to Maikell et al [55] the expected Biot number for first row of cooling on a turbine blade in engine conditions range from $Bi = 1.0$ to 2.1. At these levels, the temperature is expected to be around 4% higher than what is predicted by a spanwise-averaged analysis.

## 3.2 Coolant Warming in Laminar Pipe

The cooling jet temperature will increase as it flows through the turbine blade. This temperature increase will be determined by the heat transfer from the turbine blade to the coolant through convection as it passes through the internals of the turbine blade. The heat transfer leads to a jet exit temperature that will be higher than the initial coolant temperature. This will lead to a decrease in the effectiveness of the film cooling as the film temperature will be higher than expected when using the initial coolant temperature.

To utilize correlations, which are based on the jet exit temperature, the jet exit temperature must be known. The jet exit temperature is determined by the heat transfer to the coolant internally, which is affected by the overall heat transfer. Thus, to accurately calculate the heat transfer and temperature profiles in a film cooled solid, the internal and external cooling must be calculated simultaneously. This can be computationally expensive and difficult given the variety of flows involved. An alternative is to solve the internal cooling and external cooling iteratively and can implemented into ICHT-ROFM.

The dimensionless heat transfer coefficient with film cooling based on the traditional temperature difference between the gas and wall temperatures can be seen below.

$$\frac{h_\theta}{h_0} = \left(\frac{h_f}{h_0}\right)(1 - \eta\theta) \tag{93}$$

In experiments to measure the adiabatic effectiveness, the jet exit temperature is inherently equal to the coolant due to the adiabatic condition. In application, the jet exit temperature is expected

to be higher than the initial coolant temperature. The coolant temperature $T_C$ should be the coolest temperature the film cooled solid is exposed to. This is how Chavez et al [30] defines the $T_C$ to be the coolest internal coolant temperature for the dimensionless solid temperature.

In application, the adiabatic effectiveness is defined as below, where an effectiveness of unity corresponds to the film temperature is equal to the jet exit temperature. The jet exit temperature is unknown in application as the temperature will be determined by the energy gained during internal cooling.

$$\eta = \frac{T_G - T_{AW}}{T_G - T_{C,jet\ exit}} \tag{94}$$

The dimensionless wall temperature is defined as below. To keep the dimensionless wall temperature to its proper bounds, $T_C$ should continue to be used.

$$\theta = \frac{T_G - T_{C,internal}}{T_G - T_W} \tag{95}$$

To maintain equivalency, the remaining terms can be combined by introducing a dimensionless term for the jet exit temperature.

$$\phi_j = \frac{T_G - T_{C,jet\ exit}}{T_G - T_{C,internal}} \tag{96}$$

The modified dimensionless heat transfer coefficient can be seen below.

$$\frac{h_\theta}{h_0} = \left(\frac{h_f}{h_0}\right)\left(1 - \eta\phi_j\theta\right) \tag{97}$$

The adiabatic effectiveness times the dimensionless jet exit temperature, is the equivalent adiabatic effectiveness based on the internal coolant temperature. The equivalent effectiveness $\eta\phi_j$ is independent of the jet exit temperature and all coolant holes are normalized on the same temperature difference.

The wall temperature with the effects of internal coolant warming can be normalized on the wall temperature with no internal thermal pick up as seen below. This is equivalent to the ratio of the dimensionless wall temperature with no internal coolant warming over the dimensionless wall temperature with coolant warming.

$$\frac{T_G - T_{w,\phi}}{T_G - T_{w,\phi=1}} = \frac{\theta_{\phi=1}}{\theta_\phi} \tag{98}$$

Solving for the wall temperature with internal coolant warming yields the following.

$$T_{w,\phi} = \left(1 - \frac{\theta_{\phi=1}}{\theta_\phi}\right) T_G + \left(\frac{\theta_{\phi=1}}{\theta_\phi}\right) T_{w,\phi=1} \tag{99}$$

$\frac{\theta_{\phi=1}}{\theta_\phi}$ is bounded between '0' and '1'. '0' corresponds to a $T_{w,\phi}$ being equal to the gas temperature and '1' corresponds to $T_{w,\phi}$ being equal to $T_{w,\phi=1}$, which is the wall temperature when there is no internal thermal pick up to the coolant.

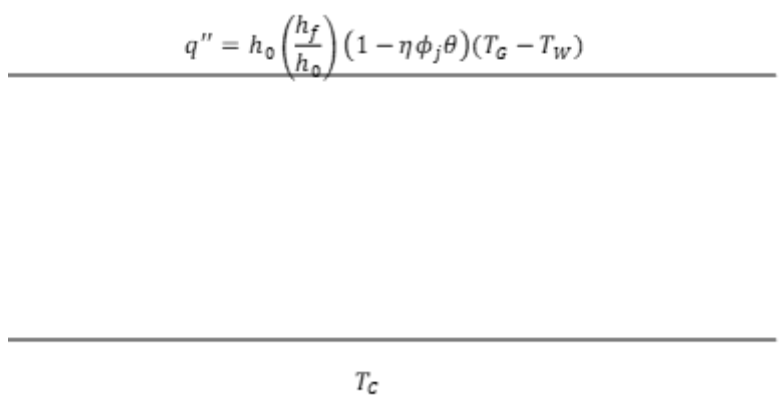


**Figure 30. Geometry and applied boundary conditions for 1D analysis of effects of coolant heating.**

For the 1-D geometry shown in Figure 30, this can be solved from an energy balance.

$$\frac{\theta_{\phi=1}}{\theta_\phi} = \frac{1 + Bi_0 \frac{h_f}{h_0} \eta\phi_j}{1 + Bi_0 \frac{h_f}{h_0} \eta} \tag{100}$$

As seen in Figure 31, the effect of $\phi$ is small when $Bi_0$, $\frac{h_f}{h_0}$, or $\eta$ is small. The Biot number is small when the solid is highly conductive compared to the local convection. It is expected that $\frac{h_f}{h_0}$ will be on the order of one and is unlikely to have a significant effect. The adiabatic effectiveness will be small when the current location is outside the effects of the cooling jet, and therefore will not be influenced by the change in the jet exit temperature.

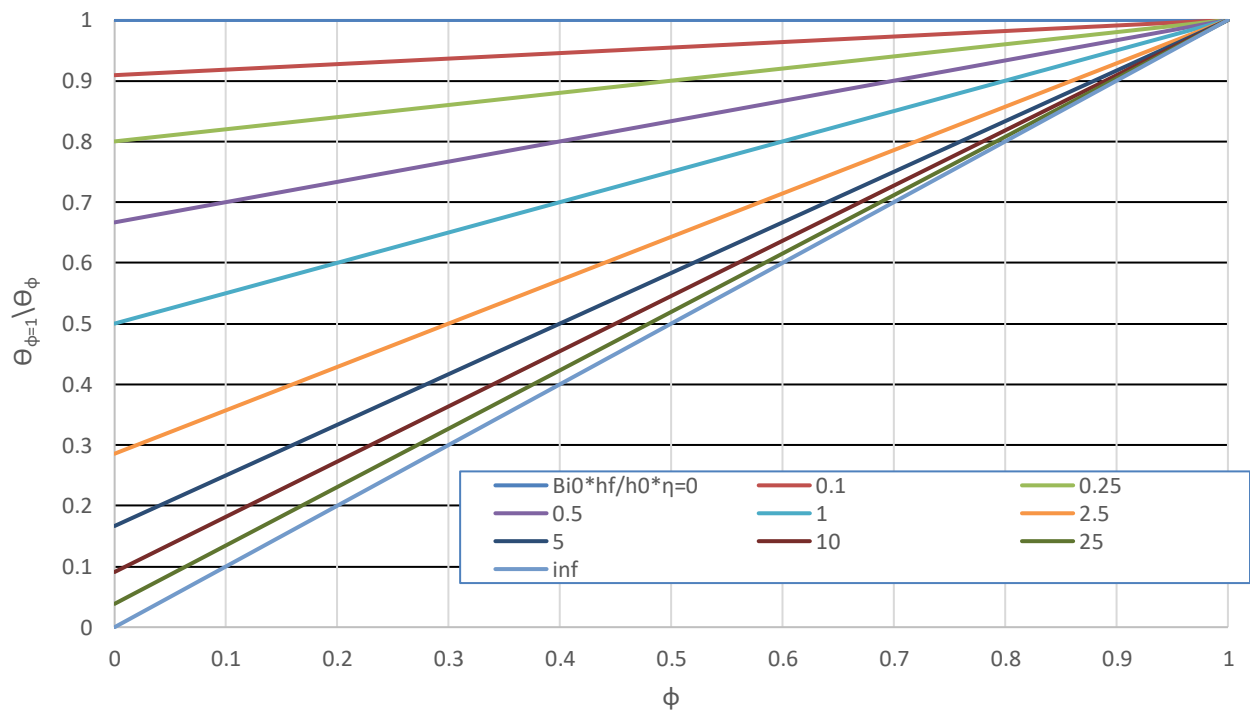


**Figure 31 Change in dimensionless wall temperature vs dimensionless jet exit temperature.**

The mean dimensionless jet exit temperature can be determined from thermodynamics. Any thermal energy convected from the wall of the cooling hole will be carried with the coolant flow.

$$\dot{Q}_{conv} = \dot{m}C_p(T_o - T_i) \tag{101}$$

Where $T_o$ is the temperature of the coolant at the outlet, $T_i$ is the temperature of the coolant at the inlet, and

$$\dot{Q}_{conv} = \int q''_{conv} dA \tag{102}$$

And the convective flux at any point along the hole is

$$q''_{conv} = h(T_s - T_m) \tag{103}$$

Where $T_s$ is the local solid temperature and $T_m$ is the local mean temperature in the flow.

For this case when looking over the entire coolant hole, the inlet temperature $T_i$ will be the coolant temperature $T_C$ and the outlet temperature $T_o$ will be the jet exit temperature $T_j$. This can be solved for the jet exit temperature.

$$T_j = \frac{\dot{Q}_{conv}}{\dot{m}C_p} + T_C$$

The coolant temperature can be updated numerically for each small step $da$ along the axis length ($a$) through the hole length.

$$T_{a+da} = \frac{d\dot{Q}_{conv}}{\dot{m}C_p} + T_a \tag{104}$$

A first pass attempt at approximating the thermal pickup along the cooling hole length would be to treat the system as internal pipe flow with constant wall temperature.

$$T_j = T_S - (T_S - T_C)\exp\left(\frac{-hA_s}{\dot{m}C_p}\right) \tag{105}$$

Substituting in h from the definition of $Nu = \frac{hD}{k}$, $\dot{m} = \rho V A_c$, and the areas for a cylindrical pipe then Eq. (105) becomes

$$T_j = T_S - (T_S - T_C)\exp\left(\frac{-4\,Nu\,k\,L}{D^2\rho V C_p}\right) \tag{106}$$

The dimensionless solid temperature normalized on the difference between the mainstream gas and the coolant is seen in Eq.(107)

$$\theta_S = \frac{T_G - T_C}{T_G - T_S} \tag{107}$$

Combining these two equations yield and solving for the dimensionless jet exit temperature as defined in Eq. (96) yields:

$$\phi_j = \frac{T_G - T_{jet\ exit}}{T_G - T_C} = \frac{1}{\theta_S} + \left(1 - \frac{1}{\theta_S}\right) \exp\left(\frac{-4\ Nu\ k\ L}{D^2 \rho V C_p}\right) \tag{108}$$

The dependence on the hole geometry L and D will be determined by the appropriate Nusselt relation. For fully developed flow laminar flow in a pipe with constant wall temperature, the accepted Nusselt relation is $Nu = 3.66$. The exponent's dependence on hole geometry becomes $\frac{L}{D^2}$. For developing laminar flow, the Nusselt relation developed by Seider and Tate [56] can be used.

$$Nu = 1.86 \left(\frac{Re\ \mathrm{Pr}\ D}{L}\right)^{\frac{1}{3}} \tag{109}$$

The resulting dependence of the convection coefficient on the hole geometry is $\left(\frac{L}{D^2}\right)^{\frac{2}{3}}$.

Figure 32 shows how the dimensionless jet exit temperature changes with varying the hole geometry using the correlation developed by Sider and Tate. This case is for evaluating air at a bulk mean temperature of 500°C with a velocity at Ma=0.4 and the dimensionless solid temperature being $\frac{1}{\theta_s} = 0.5$. The coolant warming starts to become significant for values of $\frac{L}{D^2}$ greater than $10^3$ $m^{-1}$ For values of $\frac{L}{D^2}$ greater than $10^5$ $m^{-1}$, the exit temperature is approximately the surface temperature. Figure 33 shows this region in more detail.

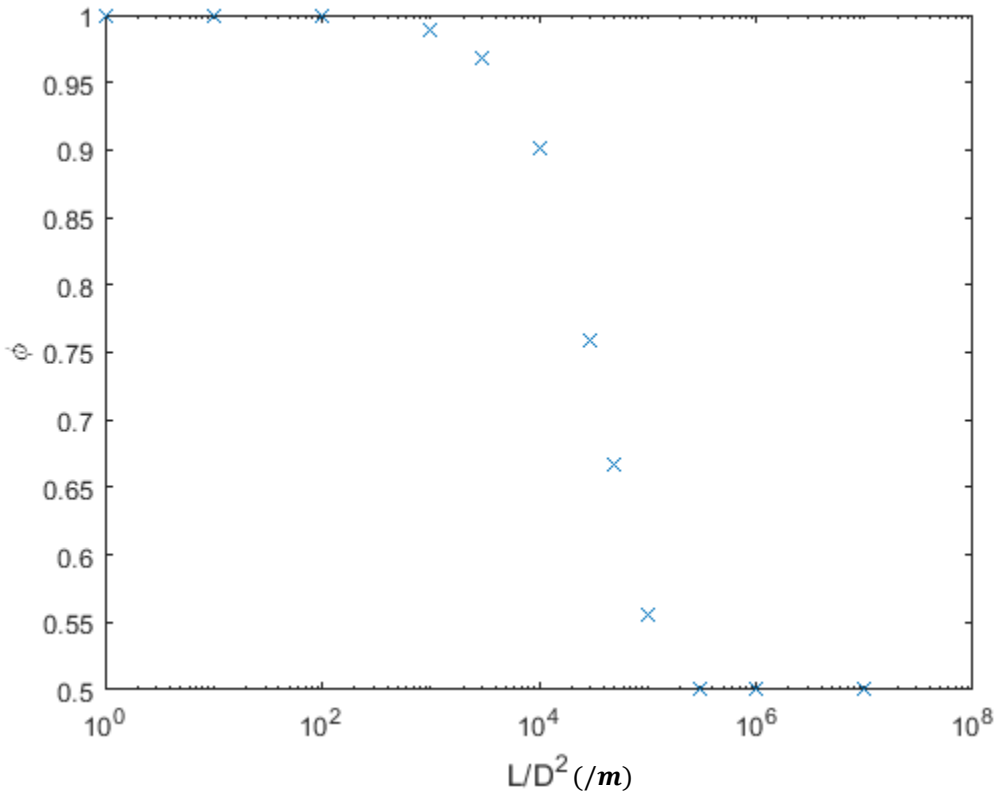


**Figure 32. Dimensionless jet exit temperature as a function for the hole geometry $L/D^2$ for air properties at a bulk temperature of 500ºC and velocity corrisponding to Ma=0.4 and dimensionless solid temperature of $\frac{1}{\theta_s}$ =0.5.**

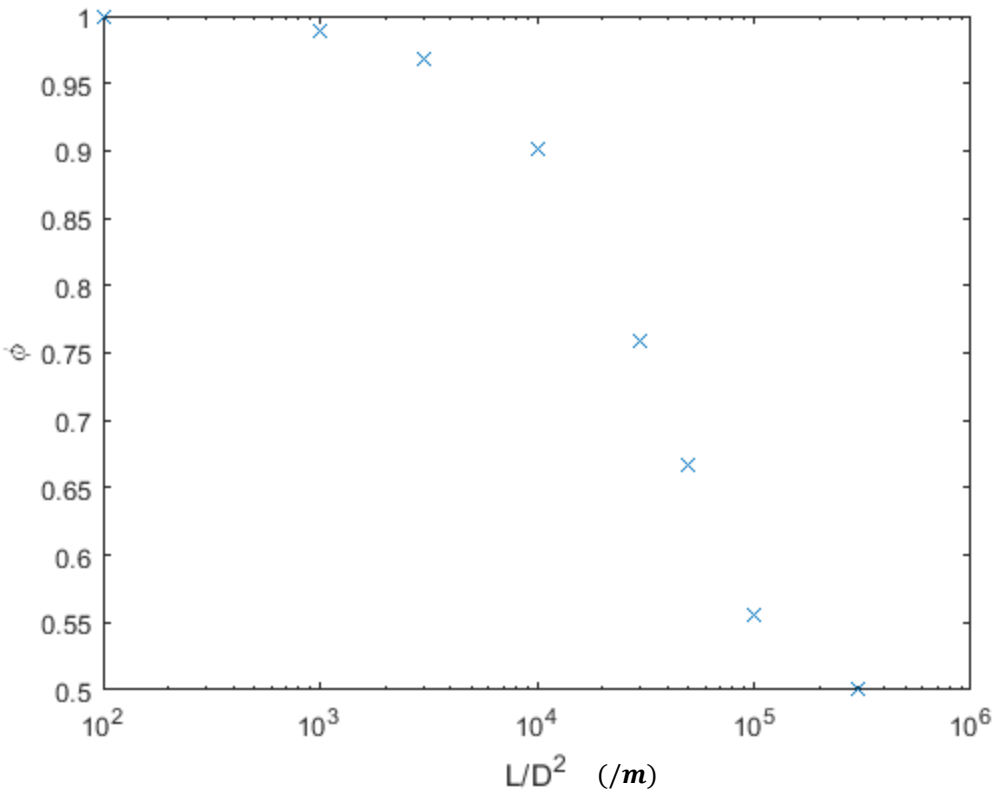


**Figure 33. Dimensionless jet exit temperature as a function for the hole geometry $L/D^2$ for air properties at a bulk temperature of 500°C and velocity corresponding to Ma=0.4 and dimensionless solid temperature of $\frac{1}{\theta_s}$ =0.5, area of interest.**

## 3.3 Coolant Warming in Turbulent Flow with Solid Conduction

Coolant warming was investigated for flow through a circular hole in a large plane. Two cases were run with the second being a scaled-up model with ten times the hole diameter with the same temperatures. The solid geometry is modeled using a finite difference method for conduction in a two dimensional cylindrical solid with geometry and boundary conditions shown in Figure 34. The fluid flowing through the center hole was discretized and its temperature was updated with the effects of convection with the local wall according to Equation (104). The outer diameter of the plane was set to a length of 20D. It was found that the cooling effects of the hole reached 8-10D, after which, the temperatures were within 1% of the 1D solution.

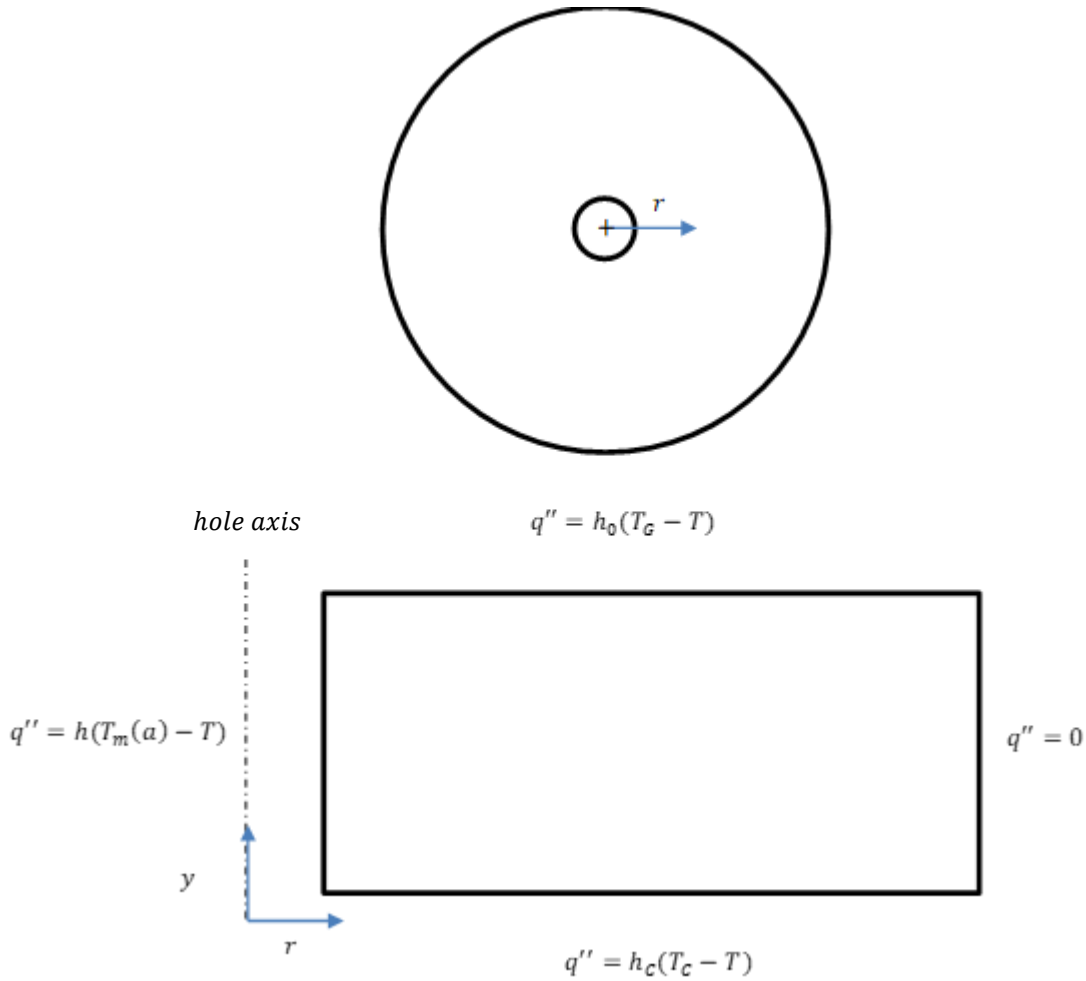


**Figure 34. Geometry and boundary conditions for radial analysis of coolant warming.**

A correlation for the heat transfer in a short turbulent vertical pipe was used with the geometry shown in Figure 34, Hata and Noda [57].

$$Nu_D = 0.02Re_d^{0.85}\left(\frac{L}{D}\right)^{-0.08}\left(\frac{\mu}{\mu_s}\right)^{0.14} \tag{110}$$

$Nu_D$ for the two cases analyzed varied from $Nu_D$=178 for the L/D=1 to $Nu_D$=148 for L/D=20.

The dimensionless jet exit temperature, $\phi$, is determined during the solid analysis and is determined by updating the mean temperature along the hole length using Eq (104). The values used in the analysis can be seen in Table 3 with air properties being evaluated at $T_G$ and $T_C$ when appropriate.

Table 3. Values used in two scaled analyses.

| | | | |
|---|---|---|---|
| D | 1 | 10 | mm |
| $T_G$ | 1000 | 1000 | K |
| $T_C$ | 300 | 300 | K |
| $h_C$ = | 5000 | 500 | W/m^2K |
| $h_0$ = | 10000 | 1000 | W/m^2K |
| k = | 15 | 15 | W/mK |

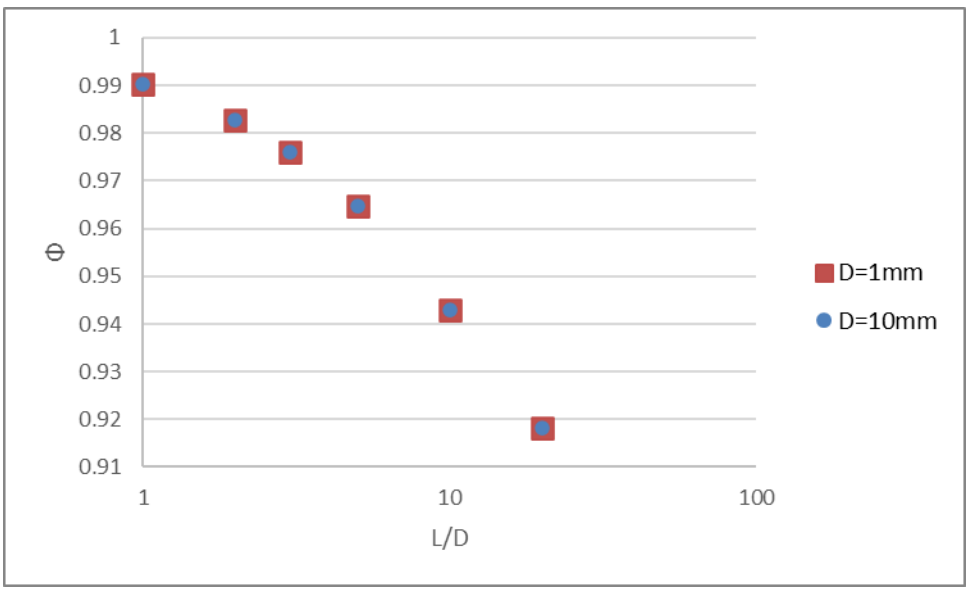


Figure 35. Dimensionless jet exit temperatures for various L/d for two scaled cases from the 2D radial analysis.

Figure 35 shows the dimensionless jet exit temperature for varying dimensionless hole length for the two hole diameters, $D$ =1mm and the scaled $D$ =10mm. The good agreement between the results of the two scales shows that the proper scaling was used. These values agree with the range seen in application according to Chavez et al [30]. The dimensionless jet exit temperature without the effects of film cooling be seen below in

$$\phi_j = \phi_j\left(St, Bi, \frac{h_C}{h_0}, Nu_D, \frac{L}{D}\right) \tag{111}$$

Here, St and Bi are based on the hot gas convective heat transfer coefficient and the thickness of the plane is the characteristic length in the Biot number. $h_C$ is the internal heat transfer coefficient and $Nu_D$ is the dimensionless heat transfer coefficient in the cooling hole.

When film cooling is included, the coolant warming gains a dependency on the film cooling parameters in addition the parameters in Eq. (111)

$$\phi_j = \phi_j\left(St_0, Bi_0, \frac{h_C}{h_0}, Nu_D, \frac{L}{D}, M, DR, Tu, \frac{x}{D}, \frac{z}{D}\alpha, \frac{P}{D}, \frac{\delta_1}{D}\right) \tag{112}$$

The jet exit temperature is there for a function of the film cooling and must be solved in conjunction with the external flow.

## Chapter 4: ICHT-ROFM Applied to a Film Cooled Flat Plate

### 4.1 Governing Equations and Turbulence Models

In this study, the fluid is assumed to be Newtonian with temperature dependent variable properties. The governing equations are the continuity, momentum, and energy equations. The instantaneous governing equations are listed below in tensor notation.

The conservation of mass

$$\frac{\partial \rho}{\partial t} + \frac{\partial}{\partial x_j}\left[\rho u_j\right] = 0 \tag{113}$$

The conservation of momentum

$$\frac{\partial}{\partial t}(\rho u_i) + \frac{\partial}{\partial x_j}\left[\rho u_i u_j + p\delta_{ij} - \mu\left(\frac{\partial \mathrm{u_i}}{\partial \mathrm{x_j}} + \frac{\partial \mathrm{u_j}}{\partial \mathrm{x_i}} - \frac{2}{3}\frac{\partial \mathrm{u_k}}{\partial \mathrm{x_k}}\delta_{\mathrm{ij}}\right)\right] = 0 \tag{114}$$

The conservation of energy

$$\frac{\partial}{\partial t}\left[\rho\left(C_v T + \frac{u_k u_k}{2}\right)\right] + \frac{\partial}{\partial x_j}\left[\rho u_j\left(C_v T + \frac{u_k u_k}{2}\right) + u_j p - \frac{C_p}{C_v}\frac{\partial T}{\partial x_j} - \mu u_i\left(\frac{\partial \mathrm{u_i}}{\partial \mathrm{x_j}} + \frac{\partial \mathrm{u_j}}{\partial \mathrm{x_i}} - \frac{2}{3}\frac{\partial \mathrm{u_k}}{\partial \mathrm{x_k}}\delta_{\mathrm{ij}}\right)\right] = 0 \tag{115}$$

The governing equations are coupled through the unknown velocity, pressure, temperature, and density and therefore must be solved simultaneously in conjunction with equations of state to relate fluid properties. With the additional complexity of the nonlinear viscous term, analytical solutions are not possible save for simple cases. This leaves CFD as the best solution method for solving complex flows.

When using CFD, it is important to select an appropriate turbulence model. Each turbulence model shows superior performance dependent upon flow conditions. Some important flow conditions are listed below.

1. Transitional flow
2. Flow separation
3. Free shear layers
4. Swirling and vortices
5. Severe adverse pressure gradients

6. Near wall regions that are not well behaved due to reverse flow

Most of these conditions exist in film cooling flows to some degree. Therefore, it is difficult for a turbulence model to perform well over the entire domain of film cooling injection. For ICHT-ROFM, many of these points do not need to be accounted for since the actual injection does not need to be modeled and resolved in CFD, only the base boundary layer formation around the solid needs to be resolved. For this study, two equation shear stress transport *k-ω* (KW-SST) model developed by Menter [58] & [59] in 1994 will be used. This model is recommended for resolving boundary layers in these flow conditions by Jennings [7] and Kane and Yavuzkurt [13].

The Navier-Stokes equations are the conservation of mass and the conservation of momentum equations in differential form. Reynolds Averaged Navier-Stokes (RANS) method averages all fluctuations of the turbulence in the flow temporally and all turbulence scales are processed with a turbulence model. Following methods proposed by J. Boussinesq (1877), turbulent stresses or Reynolds stresses in the Navier-Stokes Equation are expressed below.

$$-\rho\overline{u_i{}'u_j{}'} = \mu_t\left(\frac{\partial u_i}{\partial x_j} + \frac{\partial u}{\partial x_i} - \frac{2}{3}\frac{\partial u}{\partial x}\delta_{ij}\right) - \frac{2}{3}\rho k\delta_{ij} \tag{116}$$

where $\mu_t$ is the turbulent dynamic viscosity and needs to be modeled. One of the popular models to calculate $\mu_t$ is the RANS *k*-ω model, where the two transported variables are the turbulent kinetic energy (k-TKE) and the specific dissipation rate (ω).

$$\frac{\partial k}{\partial t} + u_j\frac{\partial k}{\partial x_j} = P_k - \beta^* k\omega + \frac{\partial}{\partial x_j}\left[(\nu + \sigma_k\nu_T)\frac{\partial k}{\partial x_j}\right] \tag{117}$$

$$\frac{\partial \omega}{\partial t} + u_j\frac{\partial \omega}{\partial x_j} = \alpha S^2 - \beta\omega^2 + \frac{\partial}{\partial x_j}\left[(\nu + \sigma_\omega\nu_T)\frac{\partial \omega}{\partial x_j}\right] + 2(1 - F_1)\sigma_{\omega 2}\frac{1}{\omega}\frac{\partial k}{\partial x_i}\frac{\partial \omega}{\partial x_i} \tag{118}$$

The closure coefficients and the auxiliary relations are very important but will not be discussed here; they can be found in Menter [58] & [59].

For all cases run, variable properties were considered and implemented for air. The density was treated as an incompressible ideal gas. The specific heat was modeled using a 5-term polynomial. The thermal conductivity was modeled with a 4-term polynomial. The viscosity was modeled using a 3-term Sutherland method. The values used in the latter three properties can be found in Appendix A: Scheme Code for Fluent ICHT-ROFM.

For the following cases, the baseline heat transfer was simulated using k-ω SST turbulence model in ANSYS-FLUENT 12 using a first-order upwind scheme. The fluid domain is solved for a geometrically similar solid without cooling holes. The baseline heat transfer is then modified using the film cooling parameters and applied to the solid. This is repeated until the baseline heat transfer coefficient and solid temperature profiles converge.

## 4.2 Investigation of Effects of 3D Conjugate Heat Transfer: 3D Flat Plate Film-Cooling Simulation at Low Temperature Difference Using ICHT-ROFM

### 4.2.1 Description of Simulation

The first case investigated was selected to compare the developed 2D correlations for the film cooling parameters developed in Chapter 2 with experimental data. The effects and importance of conjugate heat transfer were also investigated and highlighted for this case.

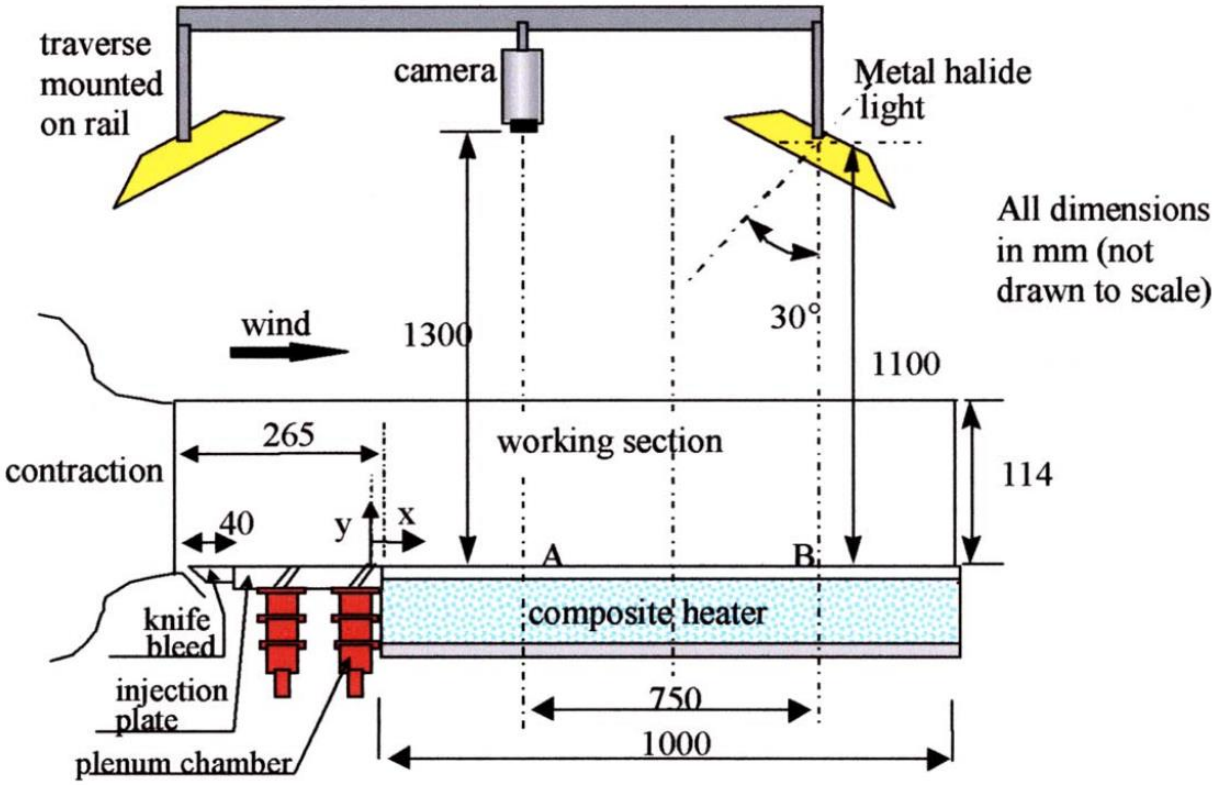


Figure 36. Flat plate with film cooling. Experimental setup of Yuen et al [18].

Flat plate film-cooling was simulated using a 3D computational domain with experimental input from Yuen et al. [18], as seen in Figure 36, which has an extensive data set on various film-cooling configurations. Table 4 gives the experimental conditions. A constant heat flux of 410 W/m$^2$ was used on the bottom surface of the metal plate. A slab of 163mm thickness was used to investigate the effect of composite conduction. The numerical simulation employed a three-dimensional grid of size 150 x 250 x 110 was for the external convection and a 200 x 50 x 100 for the metal conduction. The convection side grid was selected after performing a mesh sensitivity test. The depth of the mesh is $22D$. 3D mesh used is shown in Figure 37. The correlations developed in Chapter 2 were further modified to satisfy the spanwise-averaged data presented by Yuen et al. [18].

Table 4. Flow conditions for low temperature difference.

| **BOUNDARY CONDITIONS** | |
|---|---|
| Injection angle $\alpha=30^0$ | |
| Diameter of hole **D** | **10mm** |
| Mainstream gas velocity, $\mathbf{V_G}$ | **13m/s** |
| Mainstream temperature, $\mathbf{T_G}$ | **300K** |
| Free stream turbulence, **Tu %** | **2.7 %** |
| Coolant Temperature **Tc** | **280K** |
| Blowing Ratio **M** | 0.5 |
| **Material Properties** | |
| Material of Plate | Composite |
| Conductivity Composite **k** | 1.5 W/mK |

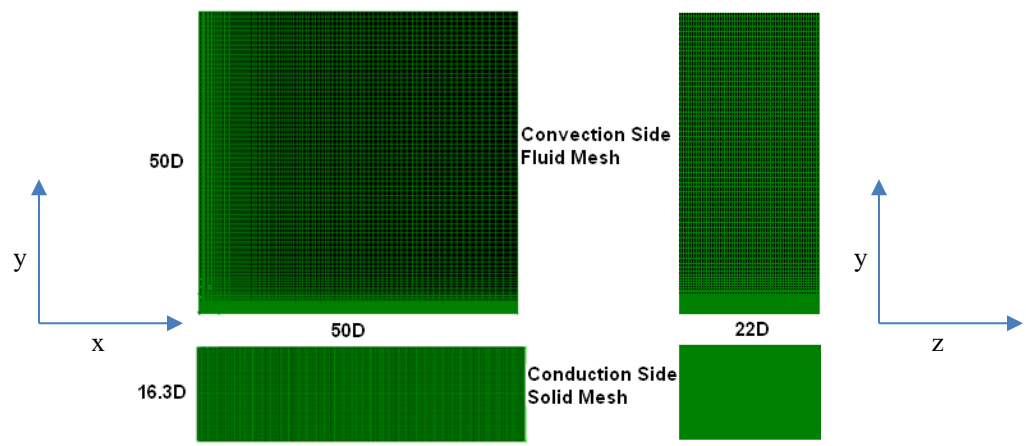


Figure 37. 3D mesh used for simulating the flat plate film-cooling experiment low temperature difference.

### 4.2.1 Results obtained Using ICHT-ROFM method

The distribution of effectiveness and heat-transfer coefficient augmentation obtained from the correlations developed here can be seen in Figure 38 and Figure 39, respectively. The effectiveness shown in Figure 38 begins at a value around 0.5 and decays downstream. Around $30D$ the effectiveness is less than 0.1 and becomes more uniform across the span. In Figure 39, the heat-transfer coefficient augmentation begins at 1.4 and quickly decays to close to 1 around

$25D$ downstream. The two peaks occur at the edge of the hole, which agrees with observations by Yuen et al. [18] and Ammari et al. [52]. The contours of effectiveness and heat-transfer coefficient augmentation is compared with data of Yuen et al. [18] [20]. This is shown in Figure 40 and Figure 41 for $M = 0.5$ and $\alpha = 30^0$. The peak value of heat-transfer coefficient augmentation is located at the hole edge to agree with the theory. The correlation starts with an effectiveness value of about 0.4 at a distance of $2D$ from the hole and decays to a value of 0.1 at a distance of $18D$. This agrees with the Yuen et al. [17] data, which begins at a value between 0.35-0.4 at a distance of $2D$ from the hole and decays to a value of 0.1 around $15D$. This is well within the resolution given by Yuen et al. [17]. The contours in Figure 41 show the similarities between the correlation results and the data given by Yuen et al. [18]. At around $15D$ the spanwise variation of the heat-transfer coefficient augmentation has dropped below the resolution of Yuen et al. [18] data.

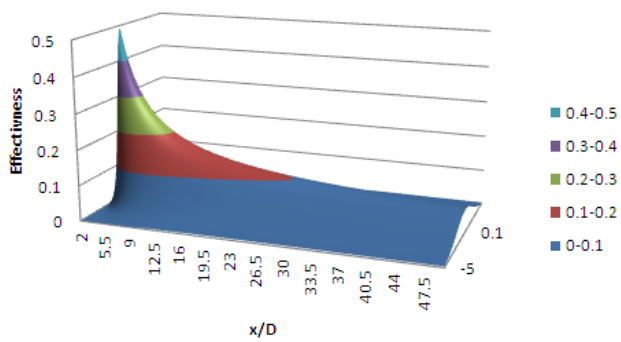


**Figure 38. Effectiveness distribution for a single hole with M=0.5, α=30⁰ from correlations.**

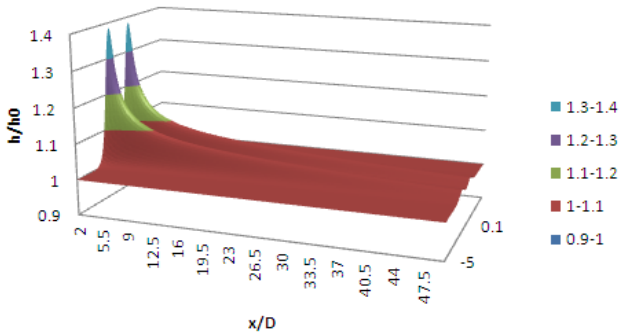


**Figure 39. Heat-transfer coefficient augmentation (hf/h0) distribution for a single hole with M=0.5, α=30$^0$ from correlations.**

The developed 2D correlations are compared to 2D empirical measurements to determine the accuracy for this case. Figure 40 and Figure 41 show the 2D contours of the effectiveness and heat-transfer coefficient augmentation from Yuen et al. [17] [18] The conjugate and non-conjugate results were obtained using the 2D correlations developed here for film-cooling on the geometry used by Yuen et al. [19]. Boundary conditions employed were the same as the spanwise-averaged study by Dhiman and Yavuzkurt [15], the inlet mainstream gas temperature was kept at 300K and secondary gas coolant temperature at 280K. Results for surface temperature contours are shown in Figure 42 - Figure 44.

The resulting temperature distribution of the solid surface, after the first iteration using the ICHT-ROFM technique (non-conjugate), is shown in Figure 42. The conjugate results found in the final iteration of ICHT-ROFM technique can be seen in Figure 43. The difference of the two iterations can be seen in Figure 44. This figure shows a maximum temperature difference of about 6K, or about 10% the maximum temperature difference or 2% of the local temperature between conjugate and nonconjugate cases. The conjugate case for this geometry is cooler overall than the non-conjugate case. This is because the plate is heated and is being cooled by the mainstream air and cooling air. This is the reverse of what will occur in turbines, as the mainstream air is hotter than the turbine blade. This agrees with the spanwise-averaged run done by Dhiman and Yavuzkurt [15]. The temperature gradients in the conjugate case are higher than that in the non-conjugate case.

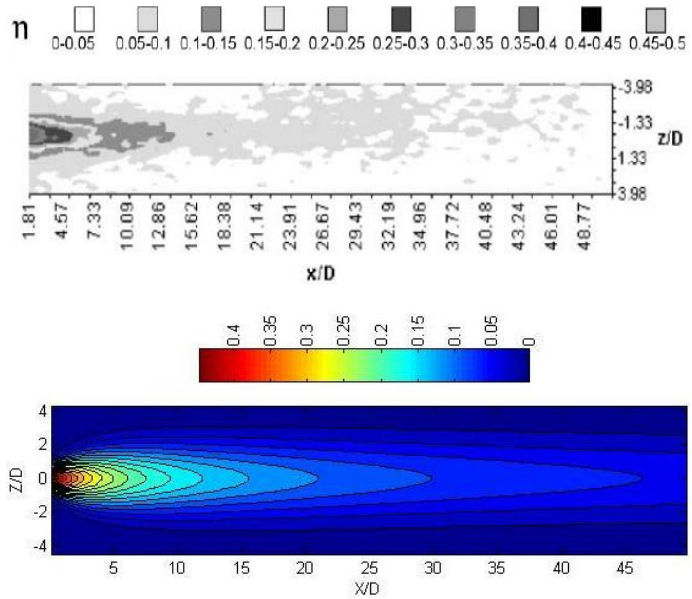


**Figure 40. Contours of effectiveness data for a single hole with m=0.5, α=30$^0$ as given by Yuen et al. [17] (upper) and from correlations (lower).**

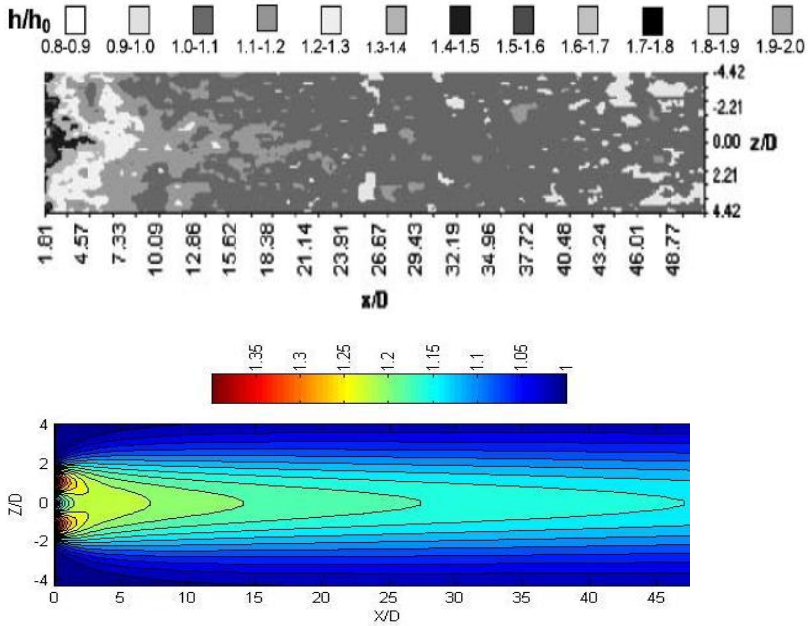


**Figure 41. Contours of heat-transfer coefficient augmentation (hf/h0) data for a single hole with M=0.5, α=30$^0$ as given by Yuen et al. [18] (upper) and from correlations (lower).**

The variations in the spanwise temperature distribution for the conjugate case are around 6 K, as can be seen in Figure 43. This is on the same order as the temperature difference between the conjugate and non-conjugate cases as can be seen in Figure 44. This shows that both conjugate and 3D simulations are needed to accurately predict the surface temperature.

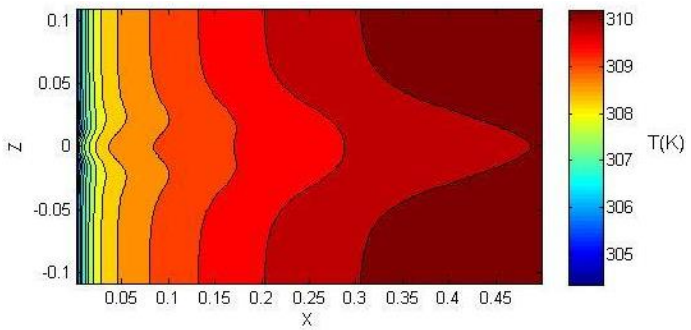


**Figure 42. Surface temperature contours for the low temperature difference study for non-conjugate solution (first iteration).**

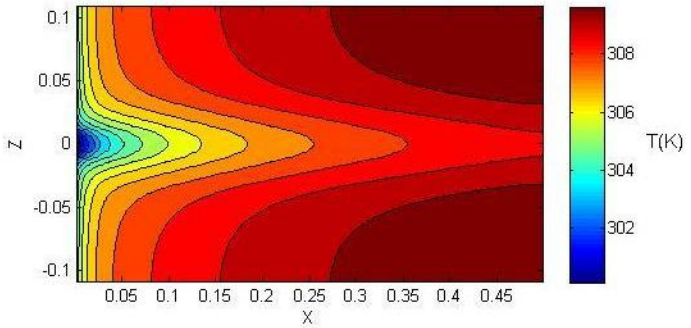


**Figure 43. Surface temperature contours for the low temperature difference study for conjugate solution (final iteration, iteration 7).**

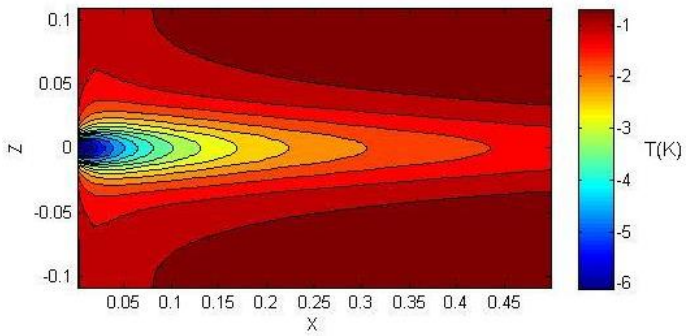


**Figure 44. Surface contours of the temperature difference between the conjugate and non-conjugate heat-transfer for the low temperature difference study.**

## 4.3 Investigation of Effects of 3D Conjugate Heat Transfer: 3D Flat Plate Film-Cooling Simulation at High Temperature Difference Using ICHT-ROFM

### 4.3.1 Description of Simulation

The second case investigated was also selected to compare the developed 2D correlations for the film cooling parameters with experimental data. For this high temperature difference case, the effects and importance of conjugate heat transfer were also investigated and highlighted.

Flat plate film-cooling was simulated with a 3D computational domain using the geometry of the Baldauf et al. [21] experiment, shown in Figure 45, as was done in 2D by Dhiman and Yavuzkurt [15] The geometry has a single row of seven film-cooling holes with flow parameters given in Table 5.

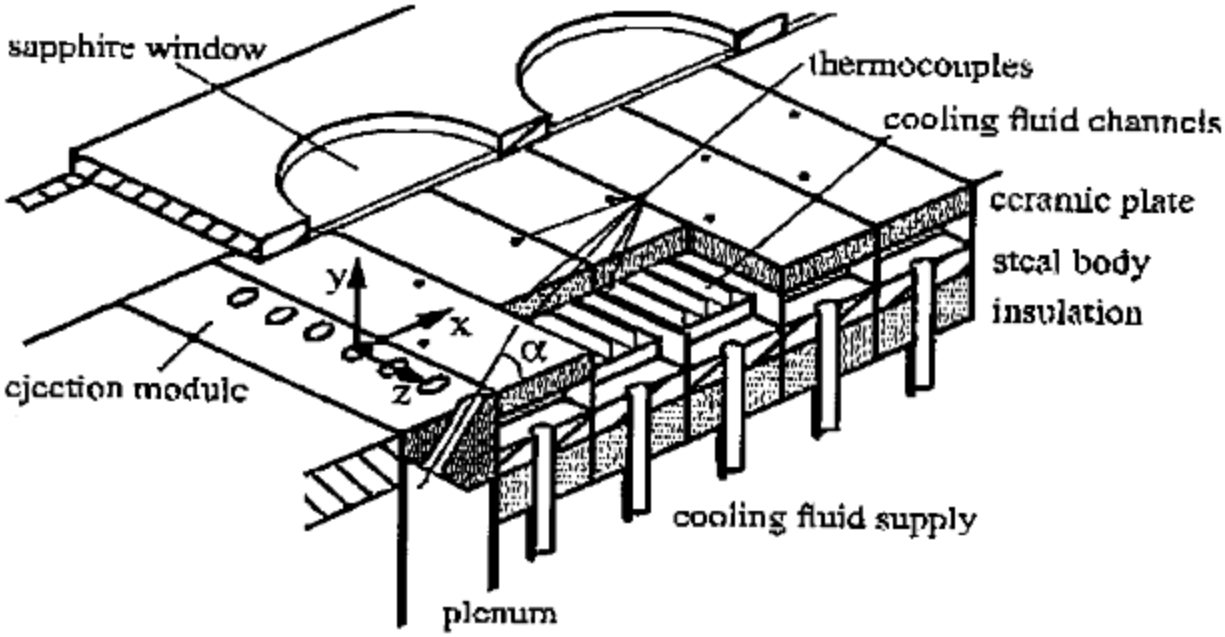


Figure 45. Flat plate with film cooling. Experimental setup of Baldauf et al. [9].

The grid shown in Figure 46 was used for the experimental set up used by Baldauf et al. [9]. A mesh size of 150 x 250 x 110 was employed for external convection and a 200 x 50 x 100 for the metal conduction. This mesh was selected after performing a mesh sensitivity test and found to be sufficient. The depth of the mesh is 44D to match the geometry in Baldauf et al. [9].

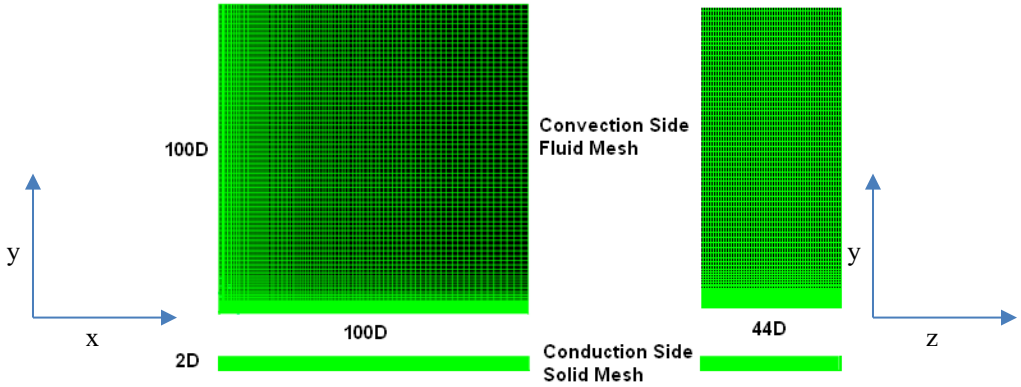


Figure 46. 3D mesh used for simulating the flat plate film-cooling experiment for high temperature difference.

Table 5. Flow conditions for high temperature difference.

| **BOUNDARY CONDITIONS** | |
|---|---|
| Injection angle $\alpha=30^0$ | |
| Diameter of hole **D** | 5mm |
| Mainstream gas velocity, $\mathbf{V_G}$ | 60m/s |
| Mainstream temperature, $\mathbf{T_G}$ | 550K |
| Free stream turbulence, **Tu %** | 1.5 % |
| Coolant Temperature **Tc** | 300K |
| Blowing Ratio **M** | 1 |
| **Material Properties** | |
| Material of Plate | Corning Macor, |
| Conductivity Corning Macor **k** | 2.0 W/mK |

### 4.3.2 Results obtained Using ICHT-ROFM method

The simulation was performed to investigate the workings of the ICHT-ROFM method using the developed 2D film-cooling correlations for effectiveness and heat-transfer coefficient augmentation. The experiment performed by Baldauf et al. [21] [22] was chosen due to its simple geometry and completeness of experimental conditions. This data was also used by Dhiman and Yavuzkurt [15] for spanwise-averaged simulations shown in Figure 47. It shows that the ICHT process for this case converges quickly in about 5 iterations for the 2D geometry. The spanwise-average temperature for this 3D case is compared to the 2D case by Dhiman and Yavuzkurt [15] to highlight the effects of the spanwise variation of film cooling parameters on the temperature predictions.

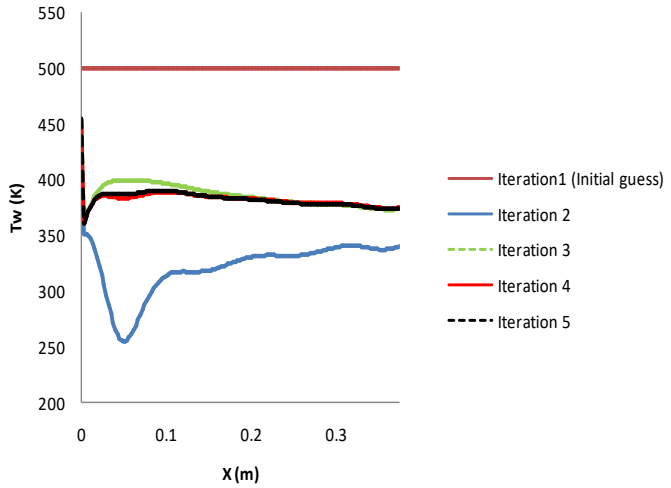


**Figure 47. Variation of surface temperature during ICHT process on a film-cooled flat plate-spanwise-averaged result Dhiman and Yavuzkurt [15] for the high temperature difference study.**

Figure 48 and Figure 50 show the contours of the film-cooling effectiveness and heat-transfer coefficient augmentation obtained from developed correlations in this study used for the 3D simulation of Baldauf et al. [9] study. Figure 49 and Figure 51 are more detailed contours in the near hole region. Due to the high level of entrainment near the hole, the location for maximum heat-transfer coefficient augmentation was chosen to occur near the mid-pitch. This agrees with the observations of Yu et al. [20]. In Figure 49, the effectiveness begins with a value of 0.5 at the hole. At $x/D$ of 20, the effectiveness has become fairly uniform. This agrees with the theory applied when developing these correlations. The heat-transfer coefficient augmentation begins at 1.6 and decays to a value below 1.1 around $x/D = 20$ as shown in Figure 51.

The temperature profile along a centerline cut through the plate is shown in Figure 52. As expected near the hole the plate temperature is significantly cooler than downstream temperatures.

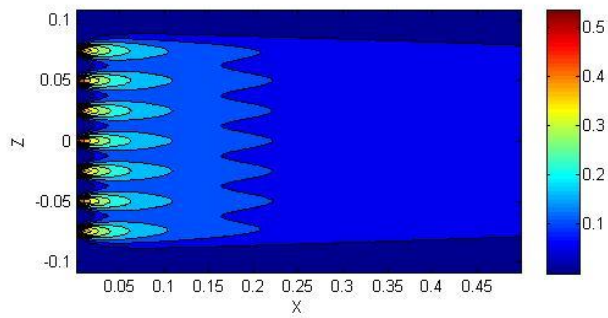


**Figure 48. Effectiveness contours used in 3D simulation for the high temperature difference study.**

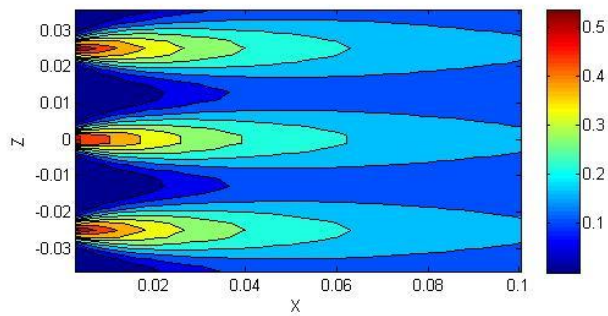


**Figure 49. Simulated effectiveness contours of near holes for center holes for the high temperature difference study obtained from developed correlations.**

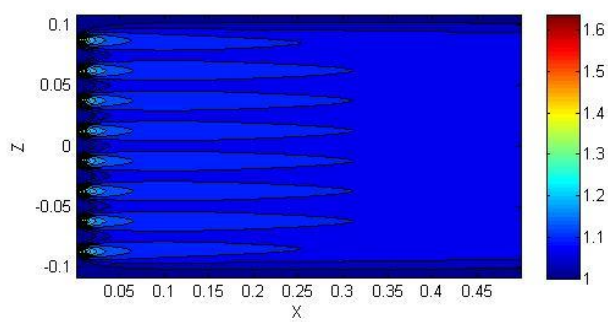


**Figure 50. Heat-transfer coefficient augmentation (hf/h0) contours used for the high temperature difference study obtained from developed correlations.**

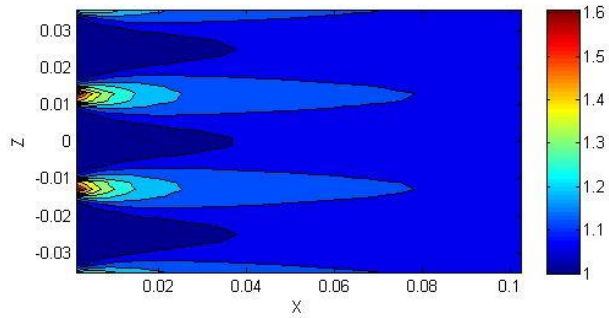


**Figure 51. Simulated heat-transfer coefficient augmentation (hf/h0) contours near center holes for the high temperature difference study obtained from developed correlations.**

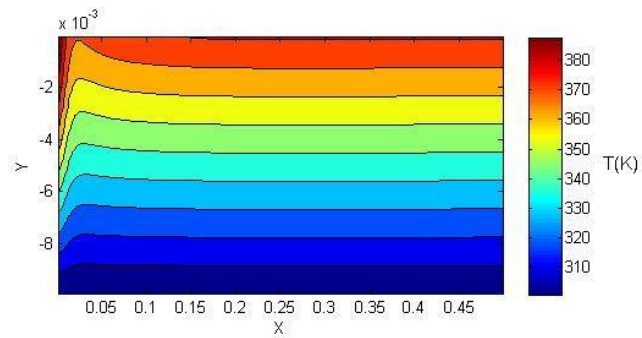


**Figure 52. Calculated temperature distribution along centerline cut of solid for the high temperature difference study.**

The resulting temperature distribution of the solid surface after the first iteration using the ICHT-ROFM technique (non-conjugate) is shown in Figure 53 with the near hole region shown in Figure 54. The conjugate results found in the final iteration of ICHT-ROFM technique can be seen in Figure 55 and the near hole region in Figure 56. High temperatures can be seen along the leading edge of the plate and at the mid-pitch between the holes. The difference of the two iterations can be seen Figure 57, with a maximum temperature difference of about 20K or about 5% of the total temperature difference ($T_G - T_C$) or 8% of the local temperature difference ($T_G - T_W$).

As can be seen, the differences in temperatures in the spanwise direction are quite significant, showing a need for 3D simulations. Along the spanwise direction, temperatures near the hole vary

between 450K near the mid-pitch and 390K near the hole. These temperature variations are of the same order of magnitude as the difference between the conjugate and non-conjugate solutions.

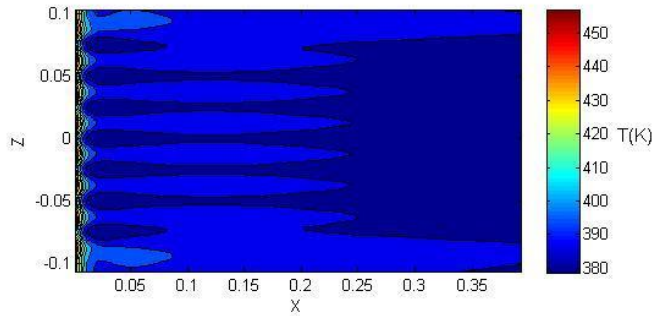


**Figure 53. Simulated surface temperature contours for the high temperature difference study, non-conjugate solution (first iteration).**

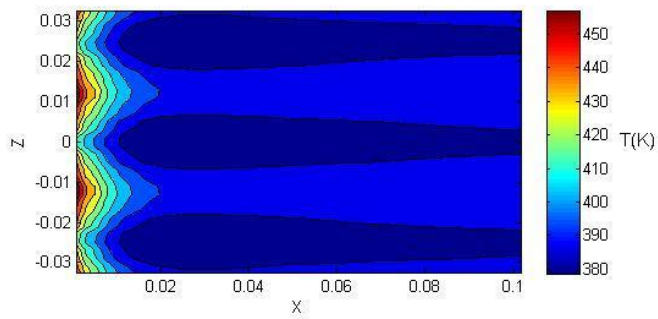


**Figure 54. Simulated surface temperature contours for the high temperature difference study, non-conjugate solution (first iteration), near-hole region.**

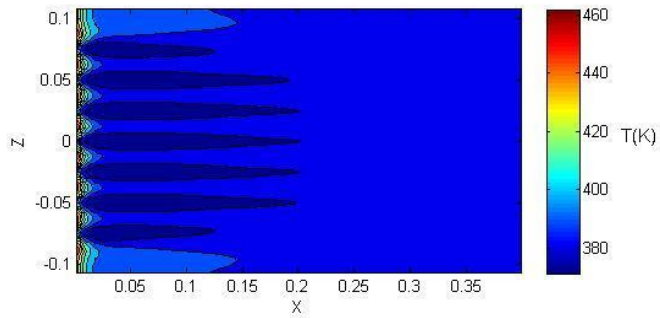


**Figure 55. Simulated surface temperature contours for the high temperature difference study, conjugate solution (final iteration).**

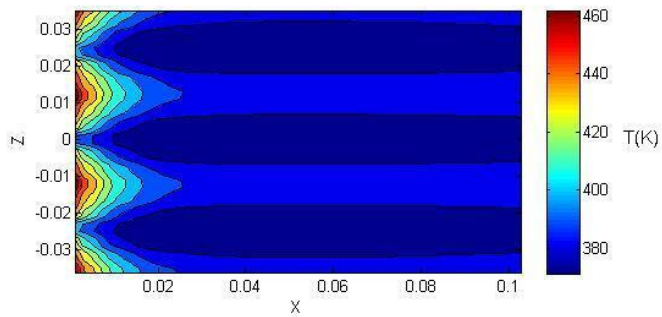


**Figure 56. Temperature contours for the high temperature difference study, conjugate solution (final iteration), near- hole region.**

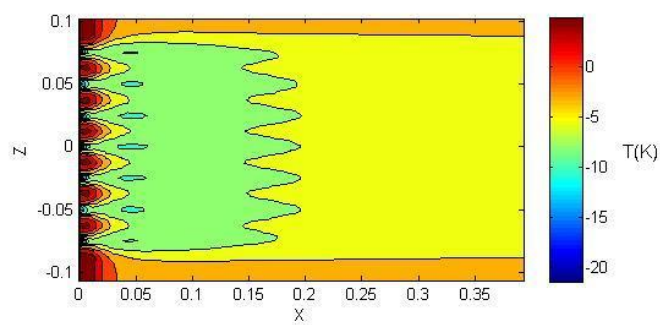


**Figure 57. Results from the current simulation for surface temperature difference between the conjugate and non-conjugate heat-transfer for the high temperature difference study.**

Figure 58 shows the spanwise-averaged temperature obtained from the 3D simulation. This is comparable to the final iteration of Dhiman and Yavuzkurt [15] shown in Figure 47. The two are similar except the near hole region. The spanwise-average result computed by Dhiman and Yavuzkurt overestimates the cooling near the hole compared to the 3D simulation. This occurs because near the hole there is significant entrainment of the mainstream gas. The entrainment causes high values of heat-transfer coefficient augmentation near the mid-pitch while the effectiveness is high near the centerline of the holes. This phenomenon cannot be captured with only a 2D simulation.

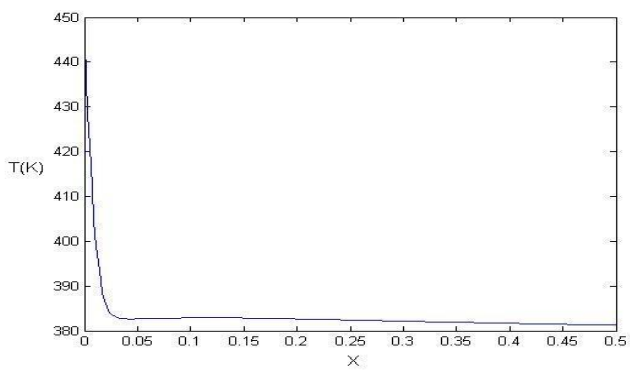


**Figure 58. Spanwise-averaged temperature of final iteration for the 3D simulation of for the high temperature difference study.**

## 4.4 Investigations of Effects of Compound Injection: 3D Flat Plate Film-Cooling Simulation Using ICHT-ROFM

### 4.4.1 Descriptions of Simulations

The next case was run to compare the correlations developed to include the effects compound injection to that of experimental data. These specific flow conditions were selected due to the well documented experimental data and flow conditions [54]. The experimental geometry can be seen in Figure 59.

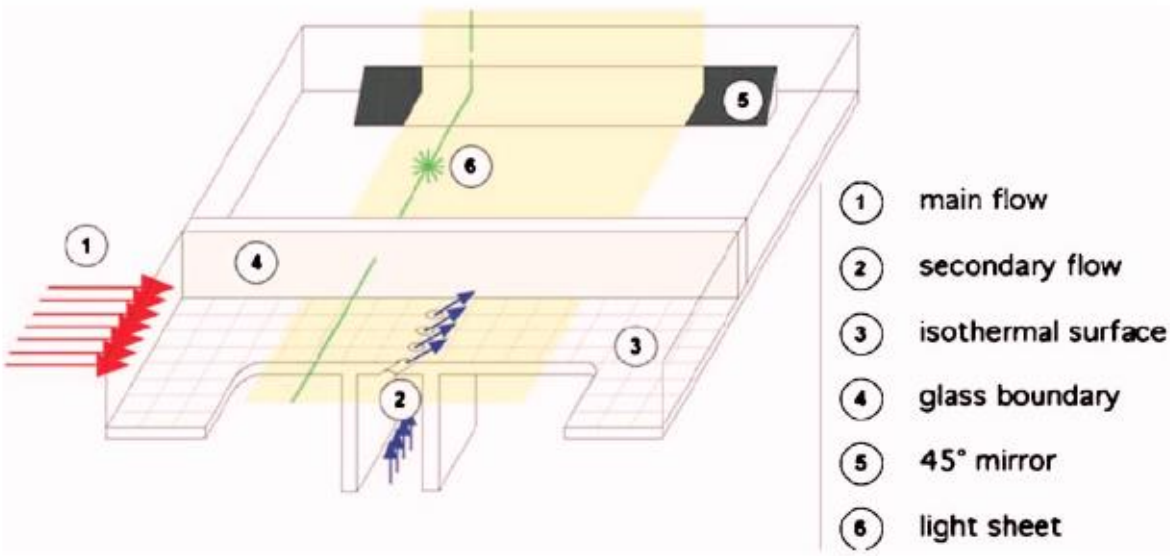


**Figure 59. Flat plate with film cooling. Experimental setup of Aga and Abhari [54].**

The case was run on a geometry similar to that used by Ingram and Yavuzkurt [60]. The flow conditions are for this case are given in Table 6. The advantage of compound angle holes is that they can output a higher amount of coolant at the same streamwise exit blowing ratio.

Table 6. General flow conditions for a compound cylindrical hole.

| **BOUNDARY CONDITIONS** | |
|---|---|
| Injection angle $\alpha=30^0$ | |
| Diameter of hole **D** | 10mm |
| Number of holes | 5 |
| Spanwise pitch P/D | 4 |
| Mainstream gas velocity, $\mathbf{V_G}$ | 60m/s |
| Mainstream temperature, $\mathbf{T_G}$ | 550K |
| Free stream turbulence, **Tu %** | 1.5 % |
| Coolant Temperature **Tc** | 300K |
| Exit Streamwise Blowing Ratio $\mathbf{M_{ex}}$ (excluding effects of α) | 0.5 |
| **Material Properties** | |
| Material of Plate | Corning Macor, |
| Conductivity Corning Macor **k** | 2.0 W/mK |
| Compound injection **β** | $60^0$ |

A mesh size of 150 x 250 x 110 was employed for external convection and 200 x 50 x 100 for the metal conduction. This mesh was selected after performing a mesh sensitivity test and found to be sufficient. The depth of the mesh is $22D$ and can be seen in Figure 60.

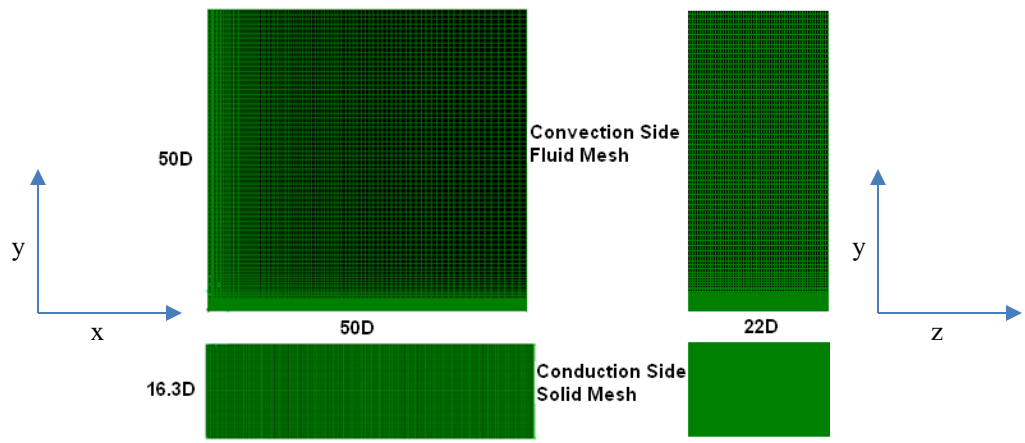


**Figure 60. 3D mesh used for simulating the flat plate film-cooling experiment for shaped hole and compound injection.**

### 4.4.2 Results obtained Using ICHT-ROFM method

The developed 2D correlations are compared to 2D empirical measurements to determine the accuracy for this case. Figure 61 and Figure 63 show the experimental measurements of adiabatic effectiveness and heat transfer coefficient augmentation for a single compound angle film cooling hole with $M = 1.0$, $\alpha = 30^0$, $\beta = 60^0$ taken from Aga and Abhari [54]. Figure 62 and Figure 64 show the results from the correlations for the same conditions, The maximum value of effectiveness at an $x/D = 5$ is about 0.45 and at $x/D = 10$ it is about 0.34. This agrees well with the result from the correlation results and its value is 0.479. The value at $x/D$ is 0.338. The centerline effectiveness predicted by the correlation is within 6.5% of the experimental data from Aga and Abhari [54]. The location of maximum effectiveness also agrees quite well and is within 7% of the measured location. The spanwise spreading agrees well near the hole but at $x/D$=10 it does not show enough spread. The spanwise distribution for compound hole deviates from a simple Gaussian distribution because the upstream jet is carried downstream resulting in a skewing of the effectiveness distribution.

The location of maximum heat transfer coefficient augmentation agrees between Figure 63 and Figure 64, as does the spreading of the heat transfer coefficient augmentation. The value of maximum heat transfer is 1.55 at about $x/D = 4$, from the correlation the value at this location is 1.54. Closer to the hole for $x/D < 4$ the correlation currently under predicts the value of heat

transfer coefficient augmentation. This is because the compound angle injection results in a significant increase in mixing at the upstream side of the jet. This local mixing effect decreases at a higher rate than the main jet mixing. The developed correlations does not fully account for this effect.

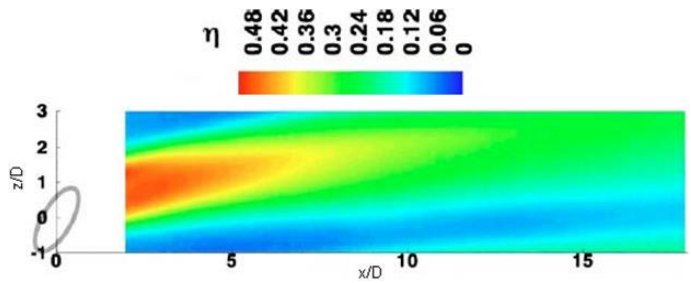


**Figure 61. Contours of adiabatic effectiveness around one of the compound angle holes measured by Aga and Abhari [54], M=1.0, $\alpha=30^0$, $\beta=60^0$.**

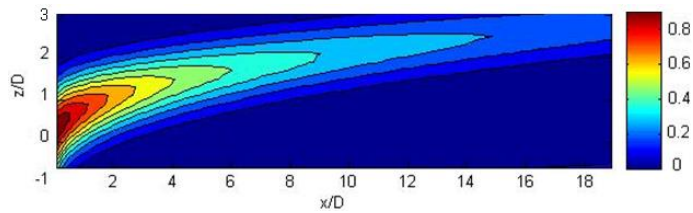


**Figure 62. Contours of adiabatic effectiveness around one of the compound angle holes, M=1.0, $\alpha=30^0$, $\beta=60^0$ obtained from the developed correlations.**

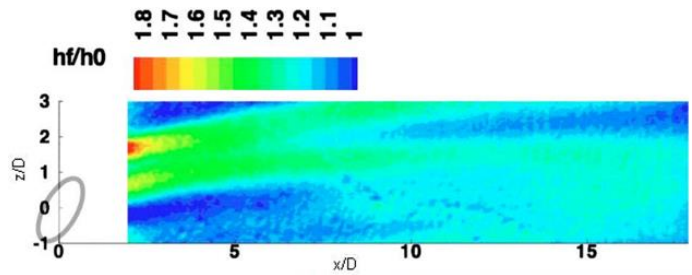


**Figure 63. Contours of heat-transfer coefficient augmentation around one of the compound angle holes measured by Aga and Abhari [54], M=1.0, α=30$^0$, β=60$^0$.**

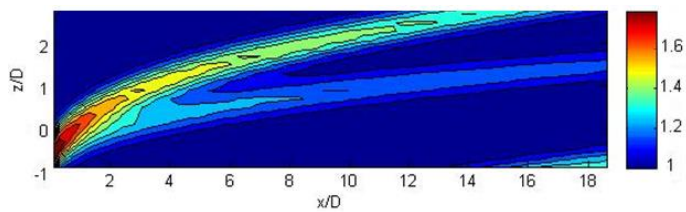


**Figure 64. Contours of heat-transfer coefficient augmentation around one of the compound angle holes, M=1.0, α=30$^0$, β=60$^0$ obtained from the developed correlations.**

Figure 65 and Figure 66 show the temperature contours from the compound angle injection resulting from correlation results in Figure 62 and Figure 64. Figure 62 shows the contour of the adiabatic effectiveness and Figure 64 heat transfer coefficient augmentation results from the correlations for a compound angle hole with $M = 1$, $\alpha = 30^0$, $\beta = 60^0$. The main advantage the compound angle holes has over the cylindrical holes is that it has an increase in heat transfer coefficient augmentation and a change in location of maximum effectiveness and heat transfer coefficient augmentation. This minimizes the high mid-span temperatures that occur with inline injection. Figure 62 shows that the overall surface coverage of the higher effectiveness is larger than that for the cylindrical hole. The maximum local temperature deviation between the conjugate and the non-conjugate results is 18K which is 11% the local temperature difference of 165K. The spanwise variation of temperature near the hole was 50K, 20% the temperature difference.

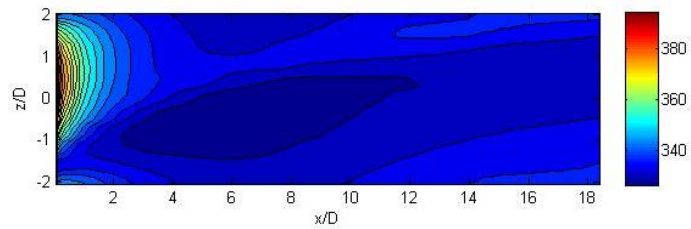


**Figure 65. Contours of temperature around one of the compound angle holes M=0.5, α=30$^0$, β=60$^0$, first iteration (non-conjugate solution).**

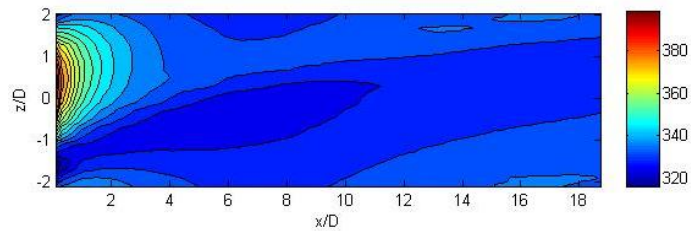


**Figure 66. Contours of temperature around one of the compound angle holes M=0.5, α=30$^0$, β=60$^0$, last iteration (conjugate solution).**

## 4.5 Investigations of Effects of Shaped Holes: 3D Flat Plate Film-Cooling Simulation Using ICHT-ROFM

### 4.5.1 Descriptions of Simulations

The next was run to compare the correlations developed to include the effects of shaped holes to that of experimental data. These specific flow conditions were selected due to the well documented experimental data and flow conditions [54]. The experimental geometry can be seen in Figure 67.

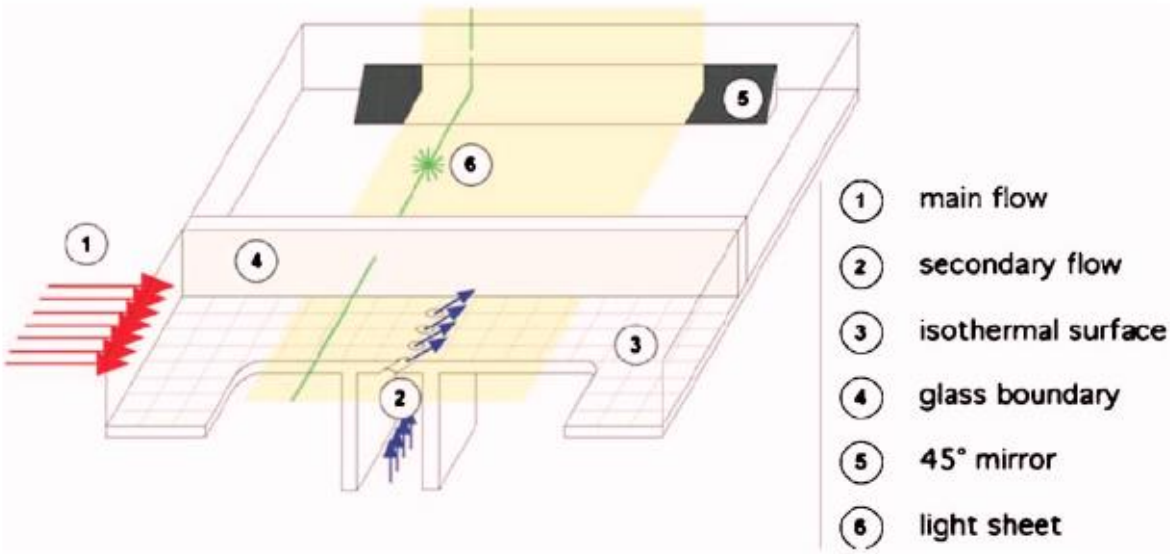


Figure 67. Flat plate with film cooling. Experimental setup of Aga and Abhari [54].

The case was run on a geometry similar to that used by Ingram and Yavuzkurt [60]. The flow conditions are for this case are given in Table 7. The advantage of shaped holes is that they can output a higher amount of coolant at the same streamwise exit blowing ratio.

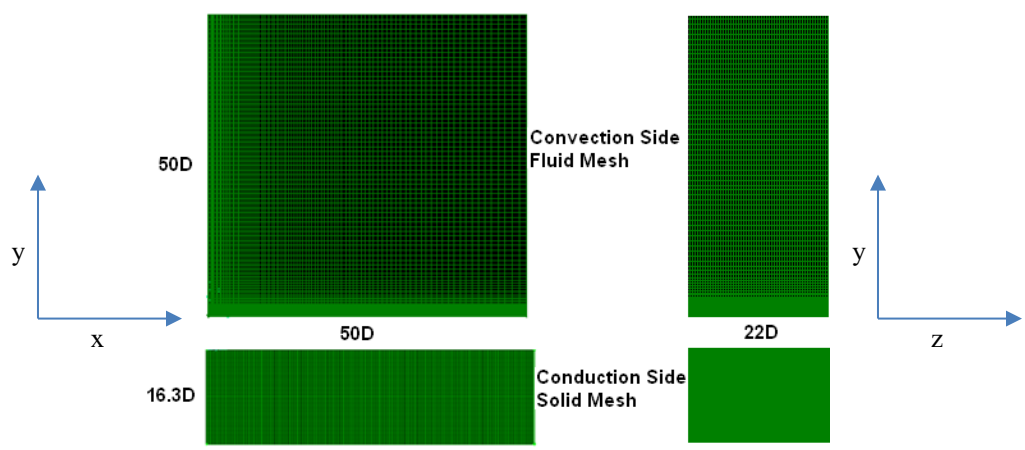


Figure 68. 3D mesh used for simulating the flat plate film-cooling experiment for shaped hole and compound injection.

**Table 7. General flow conditions for shaped holes.**

| **BOUNDARY CONDITIONS** | |
|---|---|
| Injection angle $\alpha=30^0$ | |
| Diameter of hole **D** | 10mm |
| Number of holes | 5 |
| Spanwise pitch P/D | 4 |
| Mainstream gas velocity, $\mathbf{V_G}$ | 60m/s |
| Mainstream temperature, $\mathbf{T_G}$ | 550K |
| Free stream turbulence, **Tu %** | 1.5 % |
| Coolant Temperature **Tc** | 300K |
| Exit Streamwise Blowing Ratio $\mathbf{M_{ex}}$ (excluding effects of α) | 0.5 |
| **Material Properties** | |
| Material of Plate | Corning Macor, |
| Conductivity Corning Macor **k** | 2.0 W/mK |
| Area Ratio **AR** | 2 |
| Breakthrough width **T/D** | 2 |

A mesh size of 150 x 250 x 110 was employed for external convection and 200 x 50 x 100 for the metal conduction. This mesh was selected after performing a mesh sensitivity test and found to be sufficient. The depth of the mesh is $22D$ and can be seen in Figure 68.

### 4.5.2 Results obtained Using ICHT-ROFM method

Figure 69 and Figure 70 show the contours of the adiabatic effectiveness and heat transfer coefficient augmentation for the shaped holes for $M = 1$, $\alpha = 30^0$, $AR = 2$, and $t/D = 2$ obtained from the developed correlations. The shaped hole gives significantly better coverage of the coolant over the plate when compared to the cylindrical hole. This is due to the slower decay in the maximum effectiveness resulting from shaped holes. The maximum heat transfer coefficient augmentation for the shaped hole is not as high as that in cylindrical hole but does have a higher area coverage because of the increased amount of coolant. The temperature results from the first iteration of ICHT-ROFM can be seen in Figure 71 and the final iterations results are shown in Figure 72. Again, near the hole, the temperature from the non-conjugate (first iteration) over- predicts the temperature by 8% the local temperature difference, along the centerline temperature when compared to the conjugate solution. The spanwise variation in the near-hole region is about 50K or 20% of the total temperature difference between the mainstream flow temperature and the coolant temperature. Comparing final temperatures of the cylindrical and shaped holes, seen in Figure 72, the shaped hole has significantly larger cooling area than the cylindrical holes. Shaped holes can inject more coolant than cylindrical holes at the same exit blowing ratio and the same injection tube diameter.

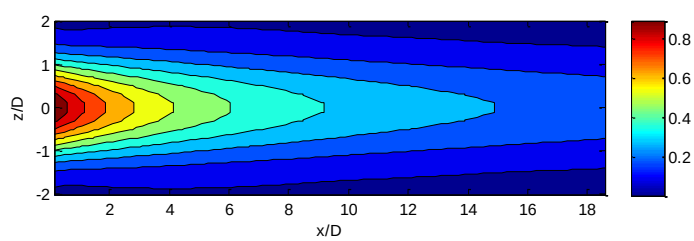


**Figure 69. Contours of adiabatic effectiveness around one of the shaped holes, M=1.0, α=30$^0$, AR=2, t/D=2 obtained from the developed correlations.**

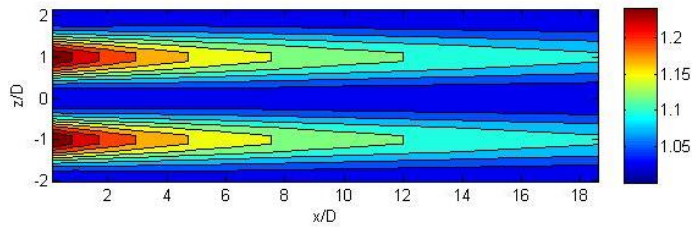


**Figure 70. Contours of heat transfer coefficient augmentation around one of the shaped holes, M=1.0, α=30$^0$, AR=2, t/D=2 obtained from the developed correlations.**

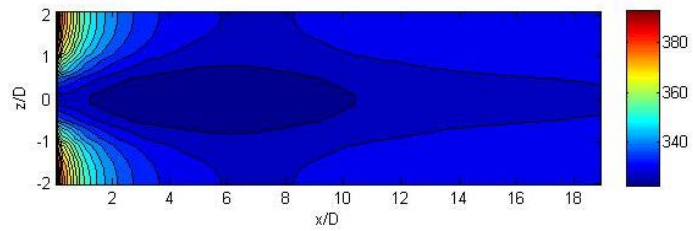


**Figure 71. Contours of temperature around one of the shaped holes M=0.5, α=30$^0$, AR=2, t/D=2, first iteration (non-conjugate solution).**

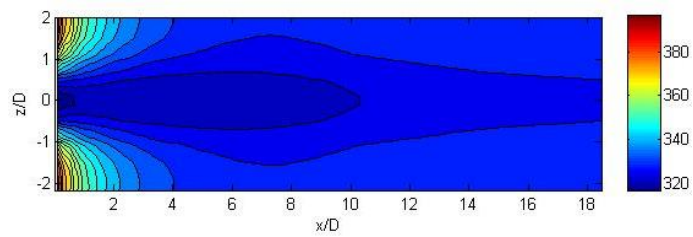


**Figure 72. Contours of temperature around one of the shaped holes M=0.5, α=30$^0$, AR=2, t/D=2 last iteration (conjugate solution).**

The spanwise-averaged temperatures of compound injection case and the shaped hole case are compared and can be seen in Figure 73. The developed correlations for both the shaped hole and the compound angle hole resulted in improved cooling effects as compared to the cylindrical holes. The shaped holes have the greatest cooling effect of about 24K near the hole when compared to the cylindrical hole. The compound hole showed a maximum improvement of 20K near the hole. The compound hole showed less of an improvement in

cooling because the shaped hole has a higher coverage area for both the effectiveness and the heat transfer coefficient augmentation. The correlation underpredicted the spreading of the effectiveness and the maximum heat transfer coefficient augmentation. This leads to a decrease in the predicted cooling effect.

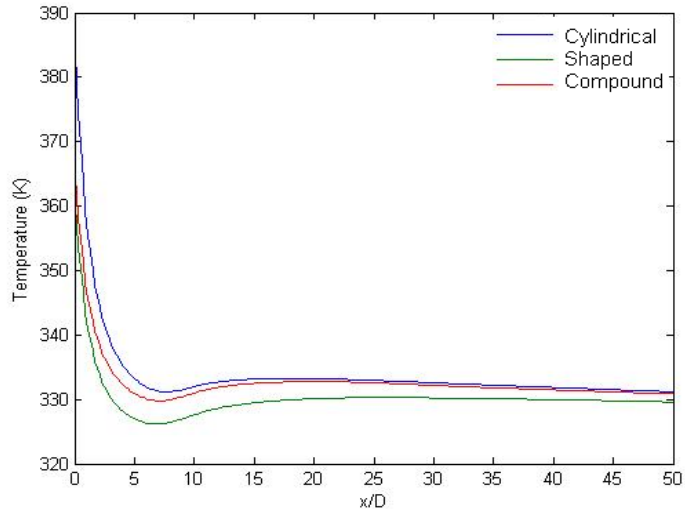


**Figure 73. Conjugate spanwise-averaged temperature profiles for cylindrical, shaped, and compound injection holes.**

## 4.6 Investigation and Implementation of Developed Superposition Technique: 3D Flat Plate Film-Cooling Simulation of Multi-row Injection with ICHT-ROFM

### 4.6.1 Description of Simulation

This case was run to compare the developed superposition technique for multi-row film cooling with that of experimental data. This specific set of flow conditions was selected due to the availability of data for both individual rows and the experimental results for the superimposed multi-row film cooling.

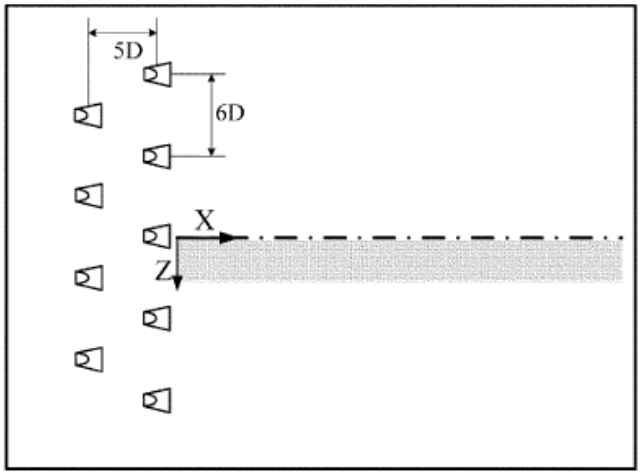


**Figure 74. Schematic of staggered rows of dustpan-shaped holes used by Zhu et al. [28].**

The superposition of two staggered rows of dustpan-shaped holes were simulated. The flow conditions can be found in Table 8 and match those used in experiments by Zhu et al. [28], seen in Figure 74, and are used to calculate the total film cooling effectiveness and heat transfer coefficient augmentation. The mesh used in the simulation is shown in Figure 75. The correlations developed for shaped holes were used for the prescribed geometry and flow conditions. These correlations were superimposed as per Equations (7) and (8) and compared to data from Zhu et al [28]. These simulations are performed using the ICHT-ROFM method while implementing the correlations for $\eta$ and $\left(\frac{h_f}{h_0}\right)$. The solid is given a constant temperature boundary condition on the bottom surface and adiabatic boundary conditions on the sides. The top of the solid is given a convective boundary condition that is updated using the ICHT-ROFM method. The simulations were run in ANSYS-FLUENT 12 using the *k-ω SST* turbulence model.

The computational grid shown in Figure 75 has 150 x 250 x 110 cells for external convection and 200 x 50 x 100 cells for the solid conduction in streamwise, wall-normal, and spanwise directions respectively. This grid was selected after performing a mesh sensitivity study and found to be sufficient. The depth of the mesh is $22D$.

**Table 8. General flow conditions for rows of shaped holes.**

| **BOUNDARY CONDITIONS** | |
|---|---|
| Injection angle $\alpha=30^0$ | |
| Diameter of hole **D** | 10mm |
| Number of holes | 4,5 |
| Spanwise pitch P/D | 6 |
| Mainstream gas velocity, $\mathbf{V_G}$ | 15m/s |
| Mainstream temperature, $\mathbf{T_G}$ | 280K |
| Free stream turbulence, **Tu %** | 1.5 % |
| Coolant Temperature **Tc** | 300K |
| Exit Streamwise Blowing Ratio $\mathbf{M_{ex}}$<br><br>(excluding effects of α) | 0.5, 1.5 |
| Material of Plate | Corning Macor, |
| Conductivity Corning Macor **k** | 2.0 W/mK |

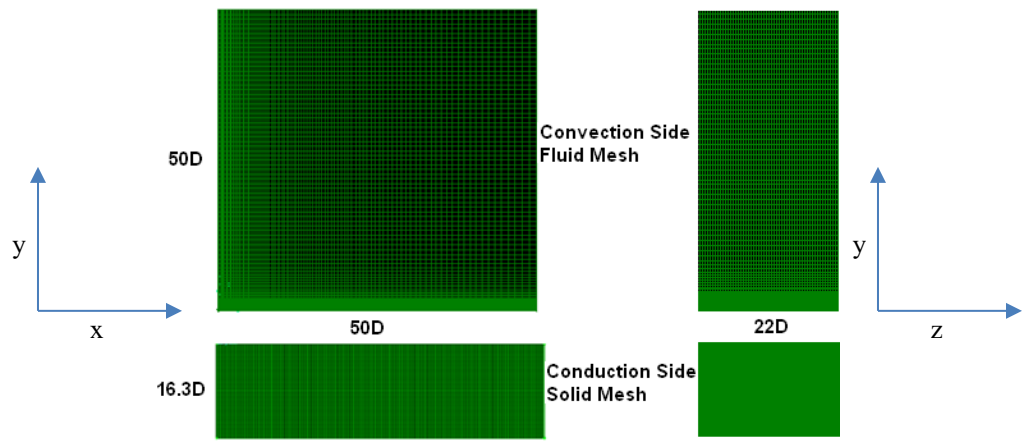


**Figure 75. 3D mesh used for simulating the flat plate film-cooling experiment for high temperature difference.**

### 4.6.2 Results obtained Using ICHT-ROFM method

The heat transfer coefficient augmentation resulting from the superposition method can be seen in Figure 76 and Figure 77 for blowing ratios of $M = 0.5$ and $M = 1.5$ respectively. The heat transfer coefficient augmentation significantly increases between the holes of the second row for both blowing ratios. This increase in heat transfer coefficients is due to mixing between the jets of the second row with jets from the first row of injection.

The superimposed film-cooling effectiveness for the lower blowing ratio $M = 0.5$ can be seen in Figure 78 and the effectiveness for the higher blowing ratio $M = 1.5$ is shown in Figure 79. For the lower blowing ratio, the effectiveness from the first row is rather uniform at about $10D$ downstream of the row with maximum values of about $\eta = 0.3$. The effectiveness from the first row in the higher blowing ratio does not become as uniform until about $25D$ due to lower mixing time with the mainstream. This results in more variations in spanwise direction. These spanwise variations cause spanwise-averaged methods to be less accurate as the average is a poorer approximation of the local values.

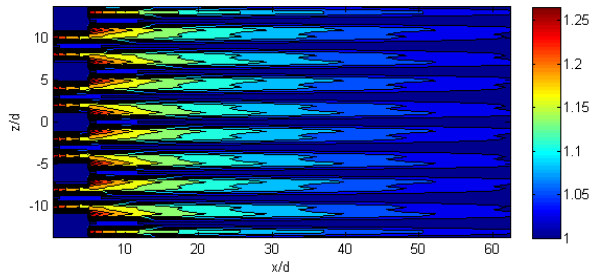


**Figure 76. Contours of heat transfer coefficient augmentation for two staggered rows, M=0.5.**

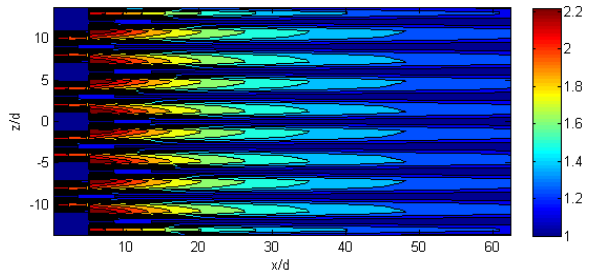


**Figure 77. Contours of heat transfer coefficient augmentation for two staggered rows, M=1.5.**

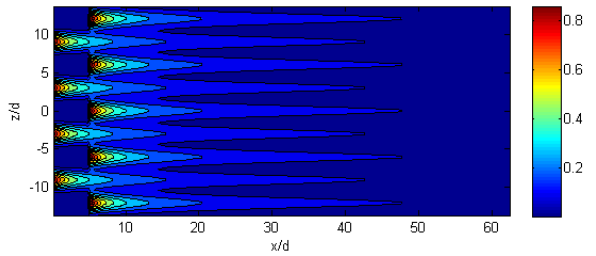


**Figure 78. Contours of effectiveness for two staggered rows, M=0.5.**

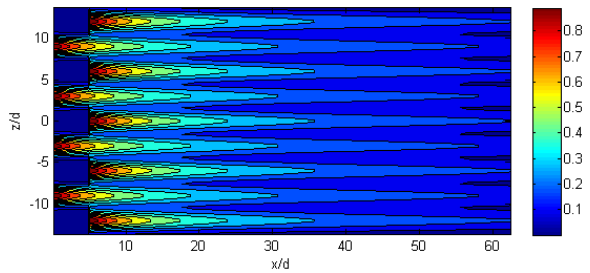


**Figure 79. Contour of effectiveness for two staggered rows, M=1.5.**

The spanwise average effectiveness of this 2D superposition technique is compared to other 1D superposition techniques in literature to highlight the effects of the spanwise variation of film cooling parameters. The spanwise-averaged results of effectiveness for the lower blowing ratio can be seen in Figure 80 along with data from Zhu et al. [28]. The method proposed in this paper agrees well with the data and has a difference with data of about 15%. The method proposed by Sellers [27] and used by Zhu et al. [28] also agrees well with data for the lower blowing ratio. This is because the effectiveness is rather uniform, as discussed earlier. The spanwise-averaged is a good approximation when the effectiveness approaches a uniform spanwise distribution.

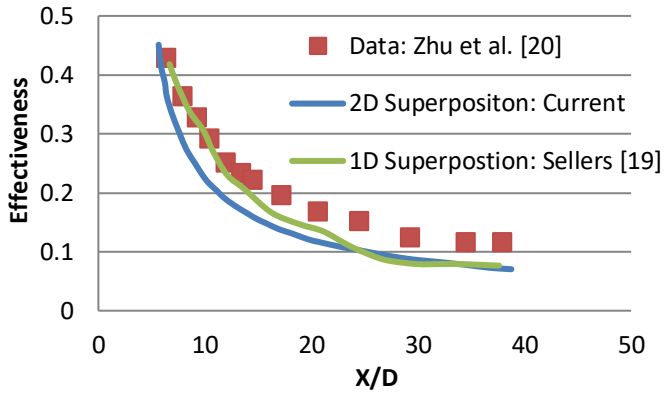


**Figure 80. Spanwise-averaged effectiveness after second row for M=0.5.**

Spanwise-averaged results of effectiveness for the higher blowing ratio can be seen in Figure 81 along with data from Zhu et al. [28]. The method proposed in this paper also agrees well with the

data within 15%. Again, some of the variation is from errors in the correlations used. The method proposed by Sellers [27] does not agree well with data for the higher blowing ratio with errors near 50%. This is due to the high spanwise variations and jet interactions that the spanwise-averaged data cannot capture. For the staggered row configuration, the film-cooling properties from the first row are high in areas where the second row is low. This yields significantly better coverage of the surface. Spanwise-average methods cannot capture this interaction as those interactions are lost when the average is taken.

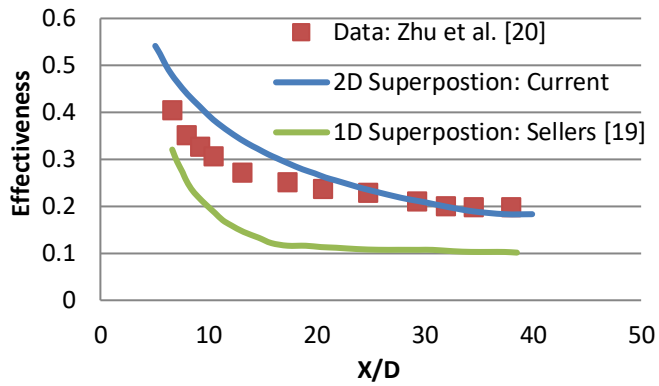


**Figure 81. Spanwise-averaged effectiveness after second row for M=1.5.**

## 4.7 ICHT-ROFM with Internal Cooling with Coolant Warming

Several items need to be addressed in order to incorporate the effects of coolant warming into the ICHT-ROFM method. First is to update the coolant temperature as it passes through the cooling hole. This could be incorporated either with in a commercial solver using a user defined function, a profile that is updated each iteration using functions outside the commercial solver, or a custom solid side solver. The last is used in further analyses.

The second is to deal with the boundary conditions for the holes in the fluid solutions. When solving the fluid side for base line convection coefficients, the solid surface temperatures is mapped to the solid fluid interface as a boundary condition. The issue arises in that there is no longer a continuous solid to map the temperatures since there is no material at the location of the cooling hole exit. The boundary condition chosen should align with that used in the baseline experiment. This could be adiabatic if the hole was filled with a low conductivity material, or constant heat flux if the test rig was replaced to one without cooling holes. Adiabatic boundary conditions will be used in further analyses.

The updated ICHT-ROFM procedure can be seen in Figure 82. The additional loop in red was added to account for the coolant warming.

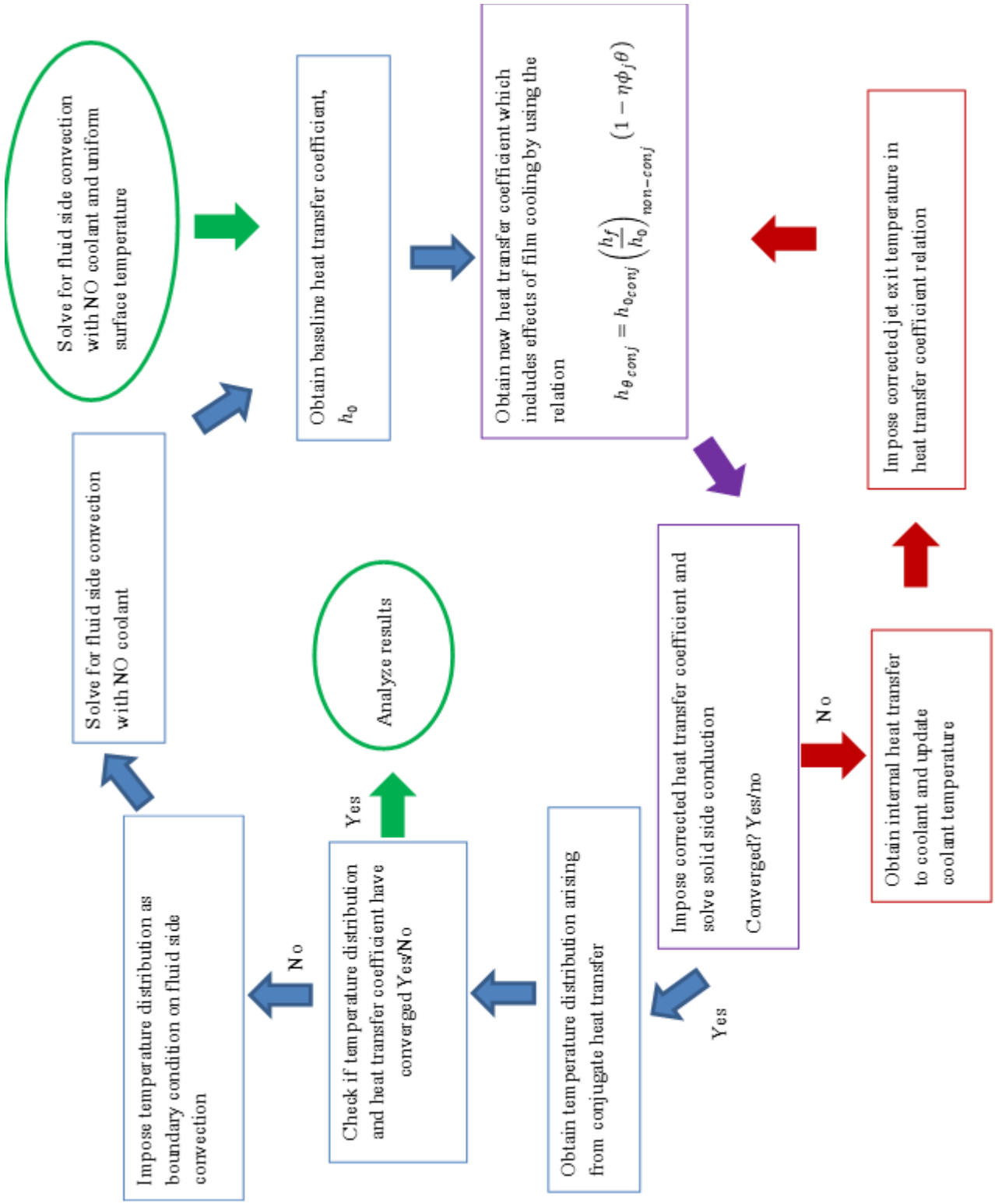


**Figure 82. Flow chart of modified ICHT-ROFM to include internal cooling effects.**

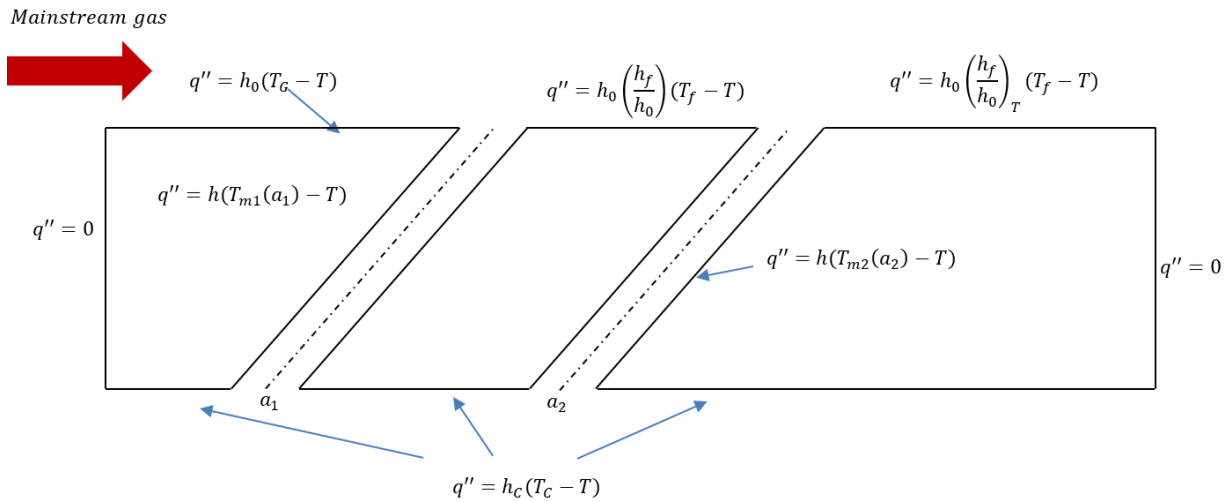


**Figure 83. Solid domain and applied boundary conditions.**

The boundary conditions for the film cooled solid are shown in Figure 83. The baseline heat transfer coefficient, $h_0$, is determined from experiment, correlation, or CFD. The last of which is used in ICHT-ROFM. $T_f$ is determined by

$$T_f \cong T_{AW} = (1 - (\eta\phi)_T)T_G + (\eta\phi)_T\, T_C \tag{119}$$

Where $(\eta\phi)_T$ is the result of superposition when appropriate. The adiabatic effectiveness and the heat transfer coefficient can be determined from experiment or correlation, the latter is used in the study at conditions as Zhu et al. [28] with $M = 0.5$. The dimensionless jet exit temperature, $\phi$, is determined during the solid analysis and is determined by updating the mean temperature along the hole length using Eq (104). Each hole jet exit temperature is determined.

The internal flow heat transfer was simplified using convection coefficient correlations and a mechanical energy balance of the flow. The correlations are mostly independent of conjugate effects; as with the correlation developed by Dittus and Boelter [61], if the correlation for turbulent flow is robust enough, the interface boundary condition does not significantly affect the heat transfer coefficient. Selection of the convective heat transfer coefficient that best fits the

internal flow is vital to accurate temperature predictions. If the conjugate effects on the internal flow are deemed to be significant, then the flow can be modeled and resolved computationally either using a full conjugate technique or using an iterative approach.

For this study, a convection coefficient was calculated from a correlation developed by Hata and Noda [57] for short vertical tubes with turbulent flow. The correlation was evaluated with properties at average temperature for the flow and for an $L/D = 4$.

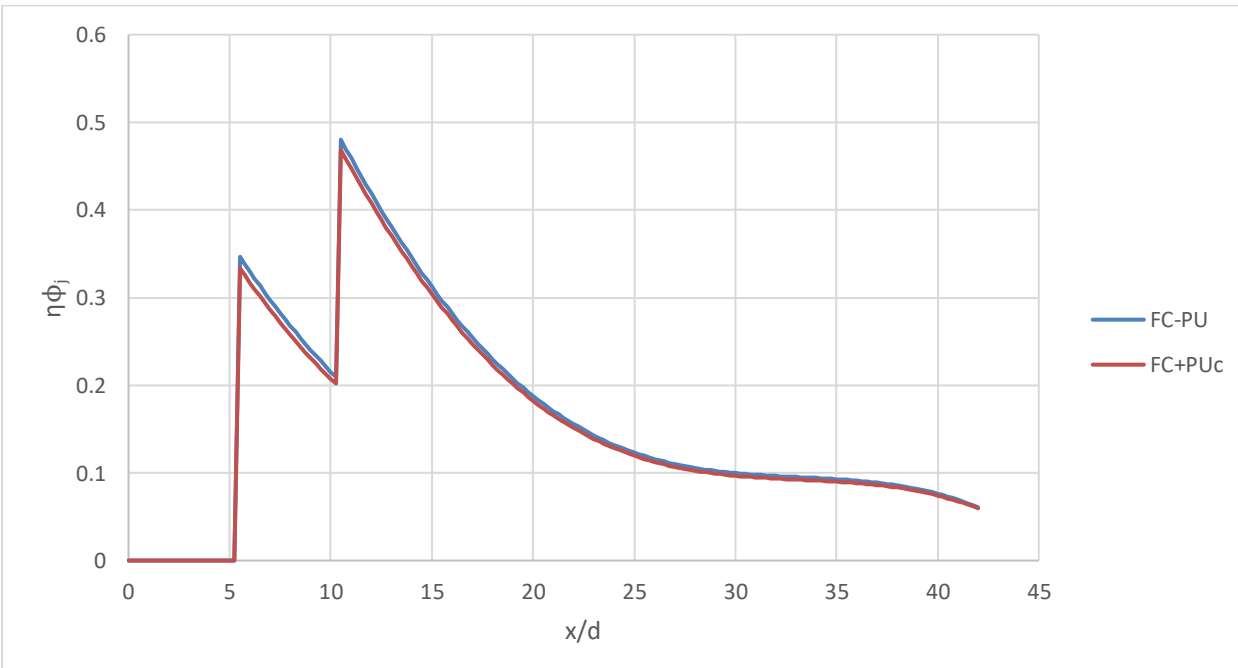


**Figure 84. Spanwise-averaged Adiabatic Effectiveness. FC-PC: Full coverage without coolant warming, FC+PUc: full coverage with coolant warming and conjugate effects.**

Figure 84 shows the spanwise-averaged adiabatic effectiveness resulting from superposition for the two cases of the film cooling without coolant warming and film cooling with coolant warming. The adiabatic effectiveness of the case with coolant warming is reduced due to the increased jet exit temperature.

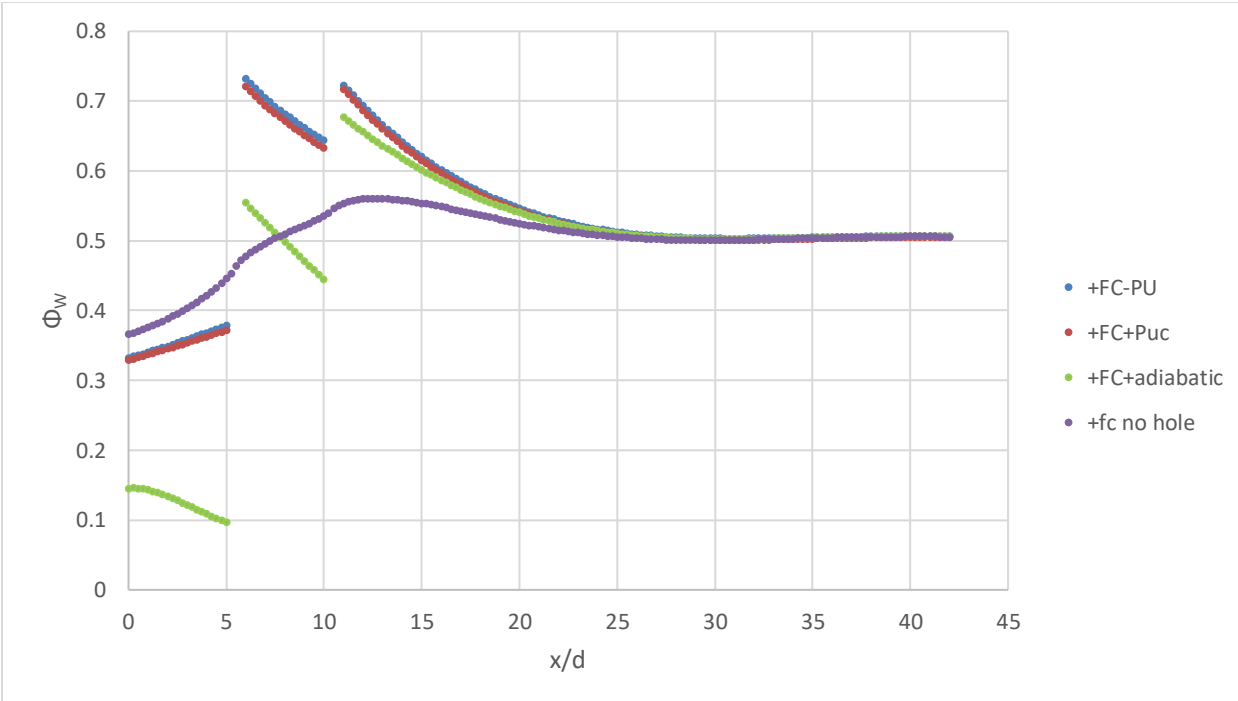


**Figure 85. Spanwise Averaged Temperature for various boundary conditions. FC-PC: Full coverage without coolant warming, FC+PUc: full coverage with coolant warming and conjugate effects, FC+adiabatic: full coverage with adiabatic cooling hole boundaries, fc no hole: full coverage without cooling hole geometry within the solid model.**

For this case, the dimensionless jet exit temperatures are $\phi_{j1} = 0.962$ and $\phi_{j2} = 0.977$ for first and second row respectively. As expected, the second row of cooling is shielded by the film from the first row, resulting in lower coolant warming in the second row of cooling holes. From the 2D radial analysis, the expected was $\phi_j = 0.970$. The first row had more significant coolant warming than predicted by the radial analysis, while the second row had less coolant warming.

Figure 85 shows the resulting wall temperatures for various boundary conditions. FC is film cooling, PU is coolant warming in the coolant hole, adiabatic is ignoring the heat transfer within the coolant hole, and the no hole refers to no hole in the solid. The case with film cooling and coolant warming and the case with film cooling and no coolant warming are compared in detail in Figure 86 and Figure 87.

The case of film cooling with an adiabatic hole and the case with film cooling and no hole differ in that the streamwise conduction is able to occur past the hole. The streamwise conduction led to cooler, but comparable, temperatures in the upstream region when compared to that with the

internal cooling. Downstream of the cooling holes, the temperature of the case without a hole is significantly warmer than the adiabatic case. This is due to the streamwise conduction around the hole, which occurs in the actual flows but is lacking in the spanwise averaged analysis.

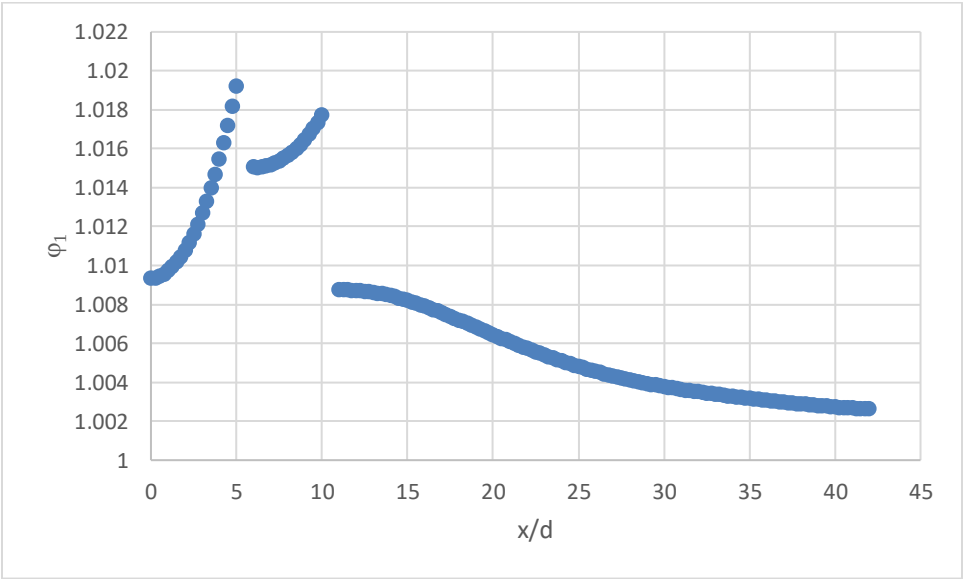


**Figure 86. Dimensionless temperature ratio of inclusion of coolant warming to that of neglecting effects of coolant warming.**

Figure 86 shows the effects of increasing coolant temperature on the surface temperatures. The temperatures across the surface has increased, with the largest effects being in the near-hole region. This is because the internal cooling is the most directly affected by the increasing coolant temperature. The increase in coolant temperature also leads to a higher film temperature and lower film cooling effectiveness. This effect is more significant when the adiabatic effectiveness is high. The increase in surface temperature is on the same order as the decrease in the dimensionless jet exit temperature.

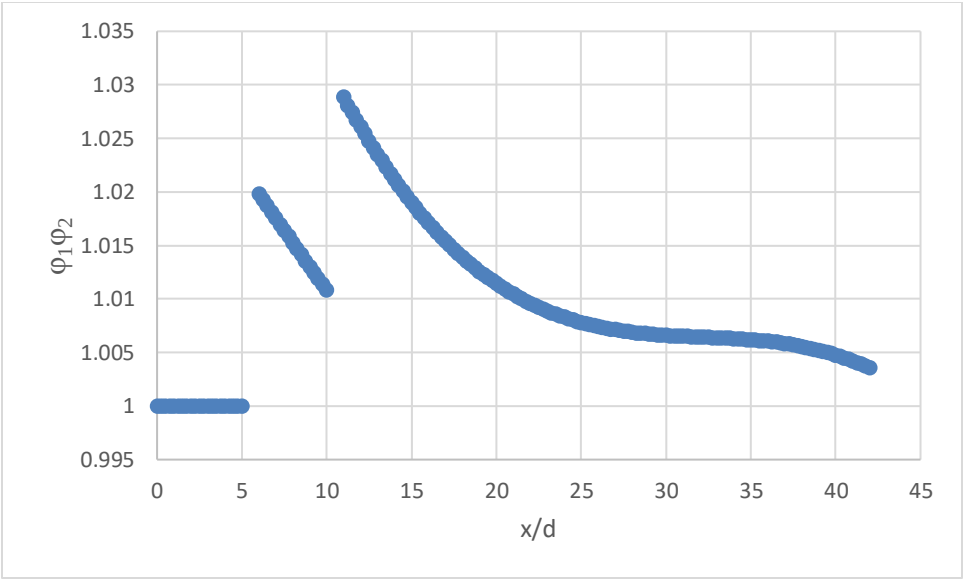


**Figure 87. Dimensionless heat transfer ratio of inclusion of coolant warming to that of neglecting effects of coolant warming.**

Figure 87 shows the effects increasing jet exit temperature on the heat transfer to the solid. The increase in film temperature due to the coolant warming leads to increased heat transfer to the solid of around 1%. This increased heat transfer is highest in the near-hole region, around 3%, where the cooling effect of the hole is diminished by the increased temperature and the adiabatic effectiveness is high and therefore more effected by increased coolant temperature. The highest increase is again on the order of the change in the dimensionless jet exit temperature.

# Chapter 5: Conclusions

Three-dimensional temperature distribution in film cooled solids was calculated using Iterative Conjugate Heat Transfer (ICHT) and Reduced Order Film Modeling (ROFM). ICHT is used to obtain conjugate temperature fields using a loosely coupled system. The convective heat transfer is calculated on a similar blade without film-cooling while under the same flow conditions. The heat transfer coefficients are corrected by use of experimental data or correlations to incorporate the effect of film-cooling on the heat transfer coefficients. ROFM needs experimental input for film cooling effectiveness and film heat transfer coefficients. Developed 2D correlations for film-cooling effectiveness and heat transfer coefficient augmentation have been improved to include the effects of shaped holes such as hole breakthrough width ($t/D$) and area ratio ($AR$). The correlations are improved to better match spanwise effectiveness of a single row of shaped cooling holes. Modifications to the correlations to improve application to compound injection ($\beta$) have been implemented. The blowing ratio is modified to account for the compound angle effect. The spanwise location of maximum film-cooling effectiveness and heat transfer coefficient augmentation are obtained as functions of the streamwise coordinate. Iterative Conjugate Heat Transfer Reduced Order Film Model (ICHT-ROFM) was used to obtain 3D conjugate temperature distribution in film cooled flat plates.

The developed correlations predicted a relative cooling effect in the near hole region for shaped holes (24 K) and for compound angle injection (20K) compared to cylindrical holes. Spanwise variations in the solid temperature in the near hole region are between 40-50K for a temperature difference of 250K between the surface and the mainstream and are quite significant, showing the need for 3D simulations. Shaped and compound angle holes increase this temperature difference due to the increased cooling. The comparisons of solid temperatures for conjugate and non-conjugate heat transfer cases show about 13-18K or 8-10% of the local temperature difference of 180K. This affirms that the calculations of 3D temperature distributions using conjugate heat transfer are very important for design purposes.

The study on the magnitude of spanwise temperature variation showed that for higher Biot numbers, 2D temperature predictions under predict the surface temperature. For the cases run, this occurred for Biot numbers larger than 0.3 with errors as large as 8%. This means that the surface temperature is 8% warmer than predicted by the 2D model.

A superposition technique for multiple-row film-cooling heat-transfer coefficient augmentation and effectiveness was investigated. The method proposed is for implementation with Iterative Conjugate Heat-Transfer using a Reduced Order Film Model (ICHT-ROFM). The superposition technique was used in conjunction with 2D correlations developed in a previous study by authors to obtain the heat transfer coefficient augmentation and film-cooling effectiveness for two staggered rows for dustpan shaped holes. The results were compared to the available experimental data for multiple-row film-cooling. The results for film-cooling effectiveness were within 15% of the data. The results obtained from the proposed technique were compared to spanwise-averaged superposition techniques, which had errors near 50% when compared with data, and were found to be more accurate. The proposed method does not rely on spanwise-averaged data and can be used to solve three-dimensional temperature distribution solids with film-cooling. For accurate temperature prediction, three dimensional calculations are necessary. The proposed method allows for two dimensional correlations and correlations obtained from experimental data for single rows to be used on more complicated hole schematics without the need for additional experiments.

ICHT-ROFM with coolant warming can increase the accuracy for temperature predictions during the design process by accounting for increasing temperature in the internal cooling systems and the effect of internal cooling on the baseline heat transfer in the external flow. ICHT-ROFM can account for these effects without having to resolve the complex flow fields of the coolant injection.

# Chapter 6: Continuing and Future Work

The ICHT-ROFM method is dependent upon having robust correlations for the film-cooling parameters. As such, continued correlation development is needed. Effects of momentum flux ratio, free stream pressure oscillations and other secondary parameters need to be accounted for. As more expansive correlations for spanwise-averaged film cooling parameters are developed, they can be implemented within the ICHT-ROFM method. The method for extending spanwise-averaged correlations into spanwise-varied correlations is dependent on the quality and expansiveness of the spanwise-averaged correlation. Continued spanwise-averaged and centerline film cooling parameter correlation development is recommended.

The developed model for spanwise variation is limited in that it assumes the only spanwise transportation is diffusion. This is not the case for compound injection or even shaped holes. A model that incorporates advection transport in the spanwise direction is recommended to be implanted for these cases.

The implemented superposition technique for multiple row injection does not account for jet interaction such as deflection of jet by subsequent rows. It is recommended that a superposition technique that includes more complex jet interactions be implemented.

An investigation of internal cooling and the effect of different modeling techniques on overall cooling should be done. An investigation into the cost-benefit of fully modeling the internal flow is recommended.

# References


[1] J. C. Han, S. Duttta and S. V. Ekkad, Gas Turbine Heat Transfer and Cooling Technology, New York: Taylor & Francis, Inc, 2000.

[2] B. Sunden, C. A. Brebbia and M. and Faghri, Heat Transfer in Gas Turbines, The University of Michigan: WIT Press, 2007.

[3] R. Mahesh, " The interaction of jets with crossflow," *Annu. Rev. Fluid Mech.,* vol. 45, no. 1, pp. 379-407, 2013.

[4] L. Gevorkyan, T. Shoji, D. R. Getsinger, O. I. Smith and A. R. Karagozian, "Transverse jet mixing characteristics," *J. Fluid Mech.,* vol. 790, pp. 237-274, 2016.

[5] B. Zang and T. H. New, "Near-field dynamics of parallel twin jets in cross-flow," *Phys. Fluid,* vol. 29, no. 3, 2017.

[6] Z. Chen, K. Hu and Y. Mao, "Simple Integral Model for Trajectories of Jet Deflection in Crossflow," *Physics of Fluids,* vol. 33, no. 111703, p. 6, 2021.

[7] T. Jennings, *Film-Cooled Gas Turbine Vane Temperarue Calculatiosn with an Iterative Conjugate Heat Transfer Approach Using Empirical Film Correlations,* State College: The Pennsylvania State University, 2011.

[8] E. R. G. Eckert, "Analysis of FIlm Cooling and Full-Coverage Film Cooling of Gas Turbine Blades," *ASME J. of Engineering for Gas Turbines and Power,* vol. 106, pp. 206-213, 1984.

[9] S. Baldauf, A. Schulz and S. Wittig, "Heat Flux Reduction from Film Cooling and Correlations of Heat Transfer Coefficients From Thermographic Measurements at Engine Like Conditions," *ASME J. Turbomach.,* vol. 124, pp. 699-710, 2002.

[10] M. Silieti, E. Divo and A. J. Kassab, "Numerical Investigation of Adiabatic and Conjugate Film Cooling Effectiveness on a Single Cylindrical Film Cooling Hole," in *ASME Heat Transfer Division*, 2004.

[11] D. E. Bohn, V. J. Becker and K. A. Krusterer, "3-d Conjugate Flow and Heat Transfer Calculations of a Film Cooled Turbine Guide Vane at Different operation Conditions," *ASME,* 1997.

[12] X. Lu, P. Jiang, H. Sugishita, H. Uechi and K. Suenaga, "Conjugate Heat Transfer Analysis of Film Cooling Flows," *J. of Thermal Science,* vol. 15, pp. 85-91, 2006.

[13] M. Kane and S. Yavuzkurt, "Calculaion of gas Turbine Blade Temeprature Using an Iterative Conjugate Heat Transfer Approach," in *Int. Symp. on Heat Transfer in gas Turbine Systems*, Antalya, Turkey, 2009.

[14] L. D. Hylton, V. Nirmalan, B. K. Sultanian and R. M. Kaufman, "The Effects of Leading Edge and Downstream Cooling on Turbine Vane Heat Transfer," NASA CR-182133, 1988.

[15] S. Dhiman and S. Yavuzkurt, "Film Cooling Calculation with an Iterative Conjugaet Heat Transfer Approach using Emperical Heat transfer Coefficient Corrections," in *ASME TurboExpo*, Glasgow, UK, 2010.

[16] R. J. Goldstein, Advances in Heat Transfer, New York: Academic Press, 1971, pp. 321-379.

[17] C. H. N. Yuen and R. F. Martinex-Botas, "Film Cooling Characteristics of a Single Round Hole at Various Angles in a Crossflow: Part I. Effectiveness," *Int. J. Heat Mass Transfer,* vol. 46, pp. 221-235, 2003.

[18] C. H. N. Yuen and R. F. Martinez-Botas, "Film Cooling Characteristics of a Single round Hole at Various Angles in a Crossflow: Part II. Heat Transfer Coefficients," *Int. J. Heat Mass Transfer,* vol. 46, pp. 237-249, 2003.

[19] C. H. N. Yuen and R. F. Martinez-Botas, "Film Cooling Characteristics of Rows of Round Holes at Various Angles in a Crossflow: Part I. Effectiveness," *Int. J. Heat Mass Transfer,* vol. 48, pp. 4995-5016, 2005.

[20] C. H. N. Yuen and R. F. Martinez-Botas, "Film Cooling Characteristics of Rows of Round Holes at Various Angles in a Crossflow: Part II. Heat Transfer Coefficients," *Int. J. Heat Mass Transfer,* vol. 48, pp. 5017-5035, 2005.

[21] S. Baldauf, A. Schulz and S. Wittig, "High Resolution Measurements of Local Effectiveness from Discrete hole Film Cooling," *ASME J. Turbomach.,* vol. 123, pp. 758-765, 1999.

[22] S. Baldauf, A. Schulz and S. Wittig, "High Resolution Measurements of Local Heat transfer Coefficients from Discrete hole Filme Cooling," *ASM J. Turbomach.,* vol. 123, pp. 749-757, 1999.

[23] S. Baldauf, M. Scheurlen, A. Schulz and S. Wittig, "Correlation of Film Cooling Effectiveness from Thermographic Measurements at Engine Like Conditions," *ASME J. Turbomach.,* vol. 124, pp. 686-698, 2002.

[24] S. V. Ekkad and J. C. Han, "A Transient Liquid Crystal Thermography Technique for Gas Turbine Heat Transfer Measurements," *Measurement Science and Technology,* vol. 11, 2000.

[25] M. Gritsch, A. Schulz and S. Wittag, "Film Cooling Holes with Expanded Exits: Near-Hole Heat Transfer Coefficients," *Int. J. of Heat and Flow,* vol. 21, pp. 146-155, 200.

[26] L. D. Hylton, M. S. Millec, E. R. Turner, D. A. Nealy and R. E. York, "Analytical and Experimental Evaluation of the Heat Transfer Distribution over Surface of Turbine Vanes," NASA Report CR 168015, 1983.

[27] J. P. J. Sellers, "Gaseous Film Cooling with Multiple Injection Stations," *AIAAJ,* pp. 2154-2156, 1965.

[28] H. Zhu, T. Guo and D. Xu, "Investigation of Film Cooling and Superpostion Method for Double Row Dustpan-Shaped holes," *Heat Transfer- Asian Research,* pp. 37-41, 2008.

[29] J. E. Dees, D. G. Bogard, G. A. Ledezma, G. M. Laskowski and A. K. Tolpadi, "Momentum and Thermal Boundary Layer Development on an Internally Cooled Turbine Vane," *Journal of Turbomachinery,* vol. 134, no. 6, 2012.

[30] K. Chavez, T. N. Slavens and D. Bogard, "Effects of Internal and Film Cooling on the Overall Effectiveness of a Fully Cooled Turbine Airfoil With Shaped Holes," in *ASME Turbo Expo 2016*, Seoul, South Korea, 2016.

[31] W. Colban, K. Thole and D. Bogard, "A Film Cooling Correlation for Shaped Holes on a Flat-Plate Surface," in *ASME Turbo Expo*, Berlin, Germany, 2008.

[32] M. Habte and S. Yavuzkurt, "Effect of Computational Grid on Performance of Two Equations Models of Turbulence for Film Cooling Applications," in *ASME Turbo Expo*, Berlin, Germany, 2008.

[33] A. Azzi and D. Lakehal, "Perspectives in Modeling Film Cooling of Turbine Blades by Transcending Conventional Two-Equations Turbulence Models," *J. of Turbomach.,* vol. 124, no. 3, pp. 472-484, 2002.

[34] J. E. Mayhew, J. W. Baughn and A. R. Byerley, "Adiabatic Effectiveness of Film Cooling with Compound Angel Holes- the effect of Blowing Ration and Freestream Turbulence," *J. of Heat Transfer,* vol. 126, p. 501, 2004.

[35] H. Foroutan and S. Yavuzkurt, "Numerical Simulations of the Near-Field Region of Film Cooling Jets under High Free Stream Turbulence: Application of RANS and Hybrid URANS/LES Models," *ASME J. Heat Transfer,* 2014.

[36] V. K. Garg, "Heat transfer on a film-cooled rotating blade using different turbulence models," *Int. J. Heat Mass Transf.,* vol. 42, no. 5, pp. 789-802, 1999.

[37] H. Ma, Q. Zhang, L. He, Z. Wang and I. Wang, " Cooling injection effect on a tran- sonic squealer tip—part i: experimental heat transfer results and CFD valida- tion," *J. Eng. Gas Turbine Power,* vol. 139, no. 5, 2017.

[38] X. Yan, Y. Huang and K. He, " Investigations into heat transfer and film cooling effect on a squealer-winglet blade tip," *Int. J. Heat Mass Transf.,* vol. 115, pp. 955-978, 2017.

[39] F. Montomoli, A. D'Ammaro and S. Uchida, "Numerical and experimental investi- gation of a new film cooling geometry with high p/d ratio," *Int. J. Heat Mass Transf.,* vol. 66, p. 366–375, 2013.

[40] Y. Jiang, L. Capone, P. Ireland and E. Romero, " A detailed study of the interac- tion between two rows of cooling holes," *J. Turbomach.,* vol. 140, no. 4, 2018.

[41] Y. Jiang, A. Murray, L. di Mare and P. Ireland, "Mesh sensitivity of RANS simulations on film cooling flow," *Int. J. of Heat and Mass Transfer,* vol. 182, 2022.

[42] L. L. Yuan, R. L. Street and J. H. Ferziger, "Large-eddy Simulations of a Round Jet in Crossflow," *J. Fluid Mech.,* vol. 379, pp. 71-104, 1999.

[43] S. Muppidi and K. Mahesh, "Direct numerical simulation of round turbulent jets in crossflow," *J. Fluid Mech.,* vol. 574, no. 59, 2007.

[44] A. Andreini, R. D. Soghe, B. Facchini, L. Mazzei, S. Colantuoni and F. Turrini, "Local source based CFD modeling of effusion cooling holes: validation and applica- tion to an actual combustor test case," *J. Eng. Gas Turbine Power,* vol. 136, no. 1, 2013.

[45] A. Burdet, R. S. Abhari and M. G. Rose, "Modeling of film cooling—part II: model for use in three-dimensional computational fluid dynamics," *J. Turbomach.,* vol. 129, no. 2, pp. 221-231, 2006.

[46] C. E. Bryant and J. L. Rutledge, "A Computational Technique to Evaluate the Relative Influence of Internal and External Cooling on Overall Effectiveness," *Journal of Turbomachinery,* vol. 142, no. 5, 2020.

[47] E. k. Look, "Teardrop Film Cooled Blade," Free Patents Online, James Ryley, [Online]. Available: http://www.freepatentsonline.com/7008186.html. [Accessed 28 March 2011].

[48] Z. Chen, Y. Li, X. Su and X. Yuan, "Scalar Diffusion Equation-Based Model to Predict 2-Dimensional Film Cooling Effectiveness of a Shaped Hole," *Journal of Turbomachinery,* vol. 143, no. 041005, p. 13, 2021.

[49] Z. Chen, Y. Mao and K. Hu, "Theoretical Model for Two-Dimensional Film Cooling Effectiveness Distribution Prediction," *Physics of Fluids,* vol. 34, no. 05122, p. 15, 2022.

[50] J. W. Ramsey, R. J. Goldstein and E. R. G. Eckert, "A Model for Analysis of the Temperature Distribution with Injection of a Heated Jet into an Isothermal Flow," 69-IC-136, 1969.

[51] S. Lawson, "Simulations of Multi-Phase Particle Deposition on Film Cooled Turbine Sections," PhD Thesis, Dept. of Mech. and Nuc. Engr. Penn State University, 2011.

[52] H. D. Ammari, N. Hay and D. Lampard, "The Effect of Density Ratio on the Heat Transfer Coefficient From a Film Cooled Flate Plate," *J. Turbomach.,* vol. 112, pp. 444-450, 1990.

[53] Y. Yu, C. H. Yen, T. I. P. Shih, M. K. Chyu and S. Gogineni, "Film Cooling Effectiveness and Heat Transfe Coefficient Distributiions around Diffusion Shaped Holes," *J. Heat Transfer,* vol. 124, 2002.

[54] V. Aga and R. Abhari, "Influence of Flow Structure on Compound Angled Film Cooling Effectiveness and Heat Transfer," *ASME J. Turbomach.,* vol. 133, 2011.

[55] J. Maikell, D. Bogard, J. Piggush and A. Kohli, "Experimental Simulation of a Film Cooled Turbine Blade Leading Edge Including Thermal BarrierCoating Effects," *Journal of Turbomachinary,* vol. 133, 2011.

[56] E. N. Seider and G. E. Tate, "Heat Transfer and Pressure Drop of Liquids in Tubes," *Industrial Engineering Chemistry,* vol. 28, pp. 1429-1435, 1936.

[57] K. Hata and N. Noda, "Momentum and Thermal Boundary Layer Development on an Internally Cooled Turbine Vane," *Journal of Power and Energy,* vol. 2, no. 1, pp. 318-329, 20082.

[58] F. R. Menter, "Zonal Two Equation k-omega Turbulence Models for Aerodynamic Flows," *AIAA,* 1993.

[59] F. Menter, "Two-Equation Eddy-Viscosity Turbulence Models for Engineering Applications," *AIAA,* vol. 32, pp. 1598-1605, 1994.

[60] P. T. Ingram and S. Yavuzkurt, "Calculations of 3-D Distribution in Film Cooled Flate plates Using 2-D Emperical Correlaitons for Film Cooling Effectiveness and Heat Transfer Augmentation," in *ASME Turbo Expo*, Copenhagen, Denmark, 2012.

[61] F. W. Dittus and L. M. K. Boelter, *University of California Publicaitons on Engineering,* vol. 2, p. 433, 1930.

[62] R. S. Bunker, "Turbine Cooling Design Analysis," in *Gas Turbine Handbook*, Department of Energy, 2005, p. Section 4.2.1.

[63] P. T. Ingram and S. Yavuzkurt, "Derivation of 2-D emperical Correlations for Film Cooling Effectiveness and Heat Transfer Augmentation From Spanwise Averaged Data and Correlations," in *ASME Turbo Expo*, San Antonio, Texas, USA, 2013.

[64] P. T. Ingram and S. Yavuzkurt, "A Superostion Technique for Multiple-Row Film Cooling for Calculations of 2-D effectiveness and Heat Transfer Coefficients," in *ASME Turbo Expo*, Montreal, Canada, 2015.

[65] J. Ahn, I. S. Jung and J. S. Lee, "Film Cooling from Two Rows of Holes with Opposite Orientation Angles: Injectant Behaviour and Adiabatic Film Cooling Effectiveness," *Int. J. of Heat and Fluid Flow,* vol. 24, no. 1, pp. 91-99, 2003.

[66] J. L. Rutledge, M. D. Polanka and N. J. Greiner, "Computational Fluid Dynamics Evaluations of Film Cooling Flow Scaling Between Engine and Experimental Conditions," *Journal of Turbomachinery,* vol. 139, no. 2, p. 7, 2017.

[67] D. D. Borup, D. Fan, C. J. Elkins and J. K. Eaton, "PROCEEDINGS OF THE ASME TURBO EXPO: TURBOMACHINERY TECHNICAL CONFERENCE AND EXPOSITION," in *ASME Turbo Expo: Turbomachinery Technical Conference and Exposition*, Oslo, Norway, 2018.

[68] S. I. Baek and S. Yavuzkurt, "Effects of Flow Oscillations in the Mainstream on Film Cooling," *Inventions,* vol. 3, no. 73, p. 34, 2018.

# Appendix

## Computer Code

Scheme Code for Fluent ICHT-ROFM

Matlab Code for Performing ICHT-ROFM

Matlab Code for Correlations for Film Cooling Effectiveness and Heat Transfer Coefficient augmentation

Matlab Code for Correlation Compiling

Matlab Code for Reading Fluent Profiles

Matlab Code for Writing Fluent Profiles

Matlab Code for Converting Fluent Profiles to Contours

Matlab Code for Plotting Contours

```
(define icht-it 7)
(define x 1)
(ti-menu-load-string (format #f "chdir /home/PIngram/Desktop/paper2/cylinder"))


;BEGIN ICHT LOOP
(do ((x 1 (+ x 1))) ((= x icht-it))
;(begin


;-----------------------------------------START GAS-----------------------------------------
;read the mesh
(ti-menu-load-string (format #f "file read-case \"fluidp5v4d.msh\"\"\"))
;check the grid
(ti-menu-load-string (format #f "mesh check"))
;turn on the energy model
(ti-menu-load-string (format #f "define models energy n"))
(ti-menu-load-string (format #f "define models energy y y"))
;set viscous model
(ti-menu-load-string (format #f "define models viscous kw-sst y"))
;set operating conditions
(ti-menu-load-string (format #f "define operating-conditions operature-pressure 101325"))

;-------------------------------------MATERIAL PROPERTIES-----------------------------------------
;set metal properties
(ti-menu-load-string (format #f "define materials change-create aluminum steel y constant 2520 y constant 794 y
constant 2 n"))
;***note steel is actually ceramic

;set air properties
(ti-menu-load-string (format #f "define materials change-create air air y incompressible-ideal-gas y polynomial 5
1057.5 -0.44890001 .0011407 -8e-7 1.9327e-10 y polynomial 4 -.00039333 .00010184 -4.8574002e-8 1.5207e-11 y
sutherland three-coefficient-method 1.716e-5 273.10999 110.56 n n n"))

;-------------------------------------BOUNDARY CONDITIONS-----------------------------------------
;set inlet bc
(ti-menu-load-string (format #f "file read-profile \"3dyuen_inlet2.prof\"\"\"))

(cond ((> x 1) (ti-menu-load-string (format #f (string-append "file read-profile temp_top_" (number->string (- x
1))))))
(else (format "\n FIRST RUN - NO PROFILE NECESSARY")))

(ti-menu-load-string (format #f "define boundary-conditions velocity-inlet inlet n n y y y n \"inlet\" \"velocity-
magnitude\" n 0 n 550 n y 1.5 0.00022"))

(ti-menu-load-string (format #f "define boundary-conditions pressure-outlet outlet n 0 n 550 n y n y 2.7 0.000044 n
n"))

(cond ((> x 1) (ti-menu-load-string (format #f "define boundary-conditions wall plate 0 n 0 y steel y temperature y n
\"top\" \"wall-temp-out-surf\" n n n n 0 n 0.5")))
(else (ti-menu-load-string (format #f "define boundary-conditions wall plate 0 n 0 y steel y temperature n 300 n n n n
0 n 0.5"))))
```

```
(ti-menu-load-string (format #f "define boundary-conditions symmetry front"))

(ti-menu-load-string (format #f "define boundary-conditions symmetry back"))

(ti-menu-load-string (format #f "define boundary-conditions symmetry top"))

(ti-menu-load-string (format #f "define boundary-conditions fluid fluid n n n n n 0 n 0 n 0 n 0 n 0 n 0 n n n n"))

;-------------------------------------------INITIALIZE-------------------------------------------
;set under-relaxation factors
(ti-menu-load-string (format #f "solve set under-relaxation k .7"))
(ti-menu-load-string (format #f "solve set under-relaxation omega .7"))
(ti-menu-load-string (format #f "solve set under-relaxation turb-viscosity .7"))
(ti-menu-load-string (format #f "solve set under-relaxation temperature .7"))
(ti-menu-load-string (format #f "solve set under-relaxation pressure .3"))
(ti-menu-load-string (format #f "solve set under-relaxation mom .7"))
(ti-menu-load-string (format #f "solve set under-relaxation density .7"))
(ti-menu-load-string (format #f "solve set under-relaxation body-force .7"))
;plot residuals
(ti-menu-load-string (format #f "solve monitors residual check-convergence y y y y y y y"))
(ti-menu-load-string (format #f "solve monitors residual plot? y"))
;initialization
(ti-menu-load-string (format #f "solve initialize compute-defaults velocity-inlet inlet"))
(ti-menu-load-string (format #f "solve initialize initialize"))
;first order setup and run
(ti-menu-load-string (format #f "solve set equations kw y"))
(ti-menu-load-string (format #f "solve set equations temperature y"))
(ti-menu-load-string (format #f "solve set discretization-scheme density 0"))
(ti-menu-load-string (format #f "solve set discretization-scheme mom 0"))
(ti-menu-load-string (format #f "solve set discretization-scheme k 0"))
(ti-menu-load-string (format #f "solve set discretization-scheme omega 0"))
(ti-menu-load-string (format #f "solve set discretization-scheme temperature 0"))
(ti-menu-load-string (format #f "solve set discretization-scheme pressure 10"))
(ti-menu-load-string (format #f "solve monitors residual convergence-criteria 1e-6 1e-6 1e-6 1e-6 1e-6 1e-6 1e-6"))
(ti-menu-load-string (format #f "solve iterate 3000"))


;-------------------------------------------OUTPUT-----------------------------------------------
;set reference values to the inlet so that the output values are correct
(ti-menu-load-string (format #f "report reference-values compute velocity-inlet inlet"))
(ti-menu-load-string (format #f "report reference-values temperature 550"))
(ti-menu-load-string (format #f "report reference-values area 0.22"))

;delete old proflies
(cond ((file-exists? "plate_htcoef.prof") (remove "plate_htcoef.prof")))
(cond ((file-exists? "plate_temp.prof") (remove "plate_temp.prof")))
(cond ((file-exists? "plate_htheta.prof") (remove "plate_htheta.prof")))


(ti-menu-load-string (format #f (string-append "file write-profile plate_htcoef_" (number->string x) " plate () heat-
transfer-coef ()")))
(ti-menu-load-string (format #f (string-append "file write-profile plate_temp_" (number->string x) " plate () total-
temperature ()")))
```

```
;disposable profiles for matlab
(ti-menu-load-string (format #f (string-append "file write-profile plate_htcoef plate () heat-transfer-coef ()")))
(ti-menu-load-string (format #f (string-append "file write-profile plate_temp plate () total-temperature ()")))


(ti-menu-load-string (format #f (string-append "file write-case-data 3dyuen_" (number->string x) ".cas")))

;--------------------------------CLEAR OLD FLAG FILE-------------------------------------------
(if (file-exists? "flag.txt") (remove "flag.txt"))
;-------------------------------------MATLAB SCRIPT-------------------------------------------
(system "matlab -nodesktop -r rofm_yuen")

(define (delay) (cond ((file-exists? "flag.txt") (
))

(else (delay))))

(delay)

;-----------------------------------------Solid-------------------------------------------
;read the mesh
(ti-menu-load-string (format #f "file read-case \"solidv2.msh\"\"))
;check the grid
(ti-menu-load-string (format #f "mesh check"))
;turn on the energy model
(ti-menu-load-string (format #f "define models energy n"))
(ti-menu-load-string (format #f "define models energy y y y"))
(ti-menu-load-string (format #f "define models viscous laminar y"))
;set operating conditions
(ti-menu-load-string (format #f "define operating-conditions operating-pressure 101325"))

;-------------------------------------MATERIAL PROPERTIES-------------------------------------------
;set metal properties
(ti-menu-load-string (format #f "define materials change-create aluminum steel y constant 2520 y constant 794 y
constant 2 n"))
;set air properties
(ti-menu-load-string (format #f "define materials change-create air air y incompressible-ideal-gas y polynomial 5
1057.5 -0.44890001 .0011407 -8e-7 1.9327e-10 y polynomial 4 -.00039333 .00010184 -4.8574002e-8 1.5207e-11 y
sutherland three-coefficient-method 1.716e-5 273.10999 110.56 n n n"))

;-------------------------------------BOUNDARY CONDITIONS-------------------------------------------
;set inlet bc
(ti-menu-load-string (format #f (string-append "file read-profile plate_htheta")))
(ti-menu-load-string (format #f "define boundary-conditions wall top 0 n 0 y steel y convection y n \"plate\" \"heat-
transfer-coef\" n 550 n"))
(ti-menu-load-string (format #f "define boundary-conditions wall bottom 0 n 0 y steel y temperature n 300 n"))
(ti-menu-load-string (format #f "define boundary-conditions wall left 0 n 0 y steel y heat-flux n 0 n"))
(ti-menu-load-string (format #f "define boundary-conditions wall right 0 n 0 y steel y heat-flux n 0 n"))
(ti-menu-load-string (format #f "define boundary-conditions wall front 0 n 0 y steel y heat-flux n 0 n"))
(ti-menu-load-string (format #f "define boundary-conditions wall back 0 n 0 y steel y heat-flux n 0 n"))

(ti-menu-load-string (format #f "define boundary-conditions solid solid y steel y 0 y n n n 0 n 0 n 0 n 0 n 0 n 0 n n"))

;-------------------------------------------INITIALIZE-------------------------------------------
;set under-relaxation factors
```

```
(ti-menu-load-string (format #f "solve set under-relaxation temperature 1"))
(ti-menu-load-string (format #f "solve set under-relaxation pressure 1"))
(ti-menu-load-string (format #f "solve set under-relaxation mom 1"))
(ti-menu-load-string (format #f "solve set under-relaxation density 1"))
(ti-menu-load-string (format #f "solve set under-relaxation body-force 1"))
;plot residuals
(ti-menu-load-string (format #f "solve monitors residual check-convergence y y y y y"))
(ti-menu-load-string (format #f "solve monitors residual plot? y"))
;initialization
(ti-menu-load-string (format #f "solve initialize initialize"))
;first order setup and run
(ti-menu-load-string (format #f "solve set equations flow y"))
(ti-menu-load-string (format #f "solve set equations temperature y"))
(ti-menu-load-string (format #f "solve set discretization-scheme mom 0"))
(ti-menu-load-string (format #f "solve set discretization-scheme temperature 0"))
(ti-menu-load-string (format #f "solve set discretization-scheme pressure 10"))
(ti-menu-load-string (format #f "solve monitors residual convergence-criteria 1e-7 1e-7 1e-7 1e-7 1e-7"))
(ti-menu-load-string (format #f "solve iterate 1000"))


;-----------------------------------------OUTPUT----------------------------------------------
;set reference values so that the output values are correct
(ti-menu-load-string (format #f "report reference-values temperature 550"))
(ti-menu-load-string (format #f "report reference-values area .11"))

(ti-menu-load-string (format #f (string-append "file write-profile temp_top_" (number->string x) " top () wall-temp-
out-surf ()")))

(ti-menu-load-string (format #f (string-append "file write-case-data yuen_icht_solid_" (number->string x) ".cas")))

;))

;(else (delay))))

;(delay)

;) ;end begin
) ;end do loop
```

```
format long

tg=550;
tc=300;
d=.01;

%reading in node locations

[x,y,z,hocon]=fluentread('plate_htcoef.prof',4);
[x,y,z,temp]=fluentread('plate_temp.prof',4);

n=length(x);

%initializing
eta=zeros(n,1);
haug=zeros(n,1);

%buidling parameters
for i=1:n
   [eta(i),haug(i)]=correlationbuildershaped(x(i),z(i));
end
%writing parameters

theta=(tg-tc)./(tg-temp);
```

```
htheta=haug.*hocon.*(1-eta.*theta);

fluentwrite3('plate_htheta.prof','plate',x,y,z,htheta,'heat-transfer-coef')

pause(5);

dlmwrite('flag.txt',n)
```

## Matlab Code for Correlations for Film Cooling Effectiveness and Heat Transfer Coefficient augmentation

```
function[eta, h, etacl, sig]=correlationbuildershaped3(x,z)

d=.01;
M=1;
sd=4;
P=1.2;
alpha=pi/6;
beta=pi/3;
delz=44;
H=7;
AR=2;
td=max(1,sin(beta)/sin(alpha));


holeloc=[-2 -1 0 1 2]*sd;

hmaxloc=[-2*sd-td/2 -2*sd+td/2 -sd-td/2 -sd+td/2 -td/2 td/2 sd-td/2 sd+td/2 2*sd-td/2 2*sd+td/2];

Me=M*(AR^0.8762);

xic=0.6+(.4*(2-cos(alpha)))/(1+((sd-1)/3.3)^6);

U=Me/P;

xi0=9;
```

```
as=4;
bs=.7;
cs=0.24;

ns=bs/((as+bs)*cs);

C1=1;

xi=x/d*sd*xic/(pi/4*U^((sd/3)-.75));

xir=xi/xi0;

etacl=C1/(1+xir^((as+bs)*cs))^ns;

M=M*cos(beta);

xie=4/pi*x/d*sd/(M*AR);

c1=0.1721;
c2=-0.2664;
c3=0.8749;

etabar=1/(sd/td+c1*M^c2*xie^c3);

sig=sd/sqrt(2*pi)*etabar/etacl;
```

```
sd=8;

ep=1.2-0.05*sd+(sd-4)*cos(alpha*1.5)/(10*sqrt(2))+2.91*(sin(1.38*alpha)-0.99)*((sd-1.7)/(1+(sd-1.7)^2)-0.277);

zeta0=45+250*cos(alpha);

n=50;

m0=(2.22-1.48*(cos(alpha))^.28)*(0.027+1.35*exp(-(1.6+.5*sin(2*alpha))*sd));

m1=0.6*(1+(2.08+1.47*cos(1.5*alpha))/(1+0.172*(sd-2.5)^2));

r=1+cos(1.5*alpha)/sqrt(2);

zeta=(x/d)^ep;

m=m0*(2*M)^(m1*P^r);

zetar=zeta/zeta0;

gamma=1-(2.1*m)^4/(1-(zetar/0.6)^7);

hbar=1/gamma*(zeta0/5)^m*((1-zetar^(m*n))^(1/n))/((1+(zeta/5)^(m*30))^(1/30));

hmax=delz/(sqrt(2*pi)*H*sig)*(hbar-1)+1;
```

```
eta=0;

for i=1:length(holeloc)
    eta=eta+etacl*exp(-(z/d-holeloc(i))^2/(2*sig^2));
end

h=0;

for j=1:length(hmaxloc)
    h=h+(hmax-1)*exp(-(z/d-hmaxloc(j))^2/(2*(sig/2)^2));
end
h=h+1;

end
```

## Matlab Code for Correlation Compiling

```
%reading in node locations
[x,y,z,temp]=fluentread('temp_top_1.prof',4);
d=0.01;
n=length(x);

%initializing
eta=zeros(n,1);
haug=zeros(n,1);
etacl=zeros(n,1);
sigeta=zeros(n,1);
etabar=zeros(n,1);


%buidling parameters
for i=1:n
   [eta(i),haug(i)]=correlationbuildershaped(x(i),z(i));
end
%writing parameters
dlmwrite('eta.prof',eta,'precision',8);
dlmwrite('haug.prof',haug,'precision',8);


data=[x/d,z/d,eta];
datas=sortrows(data);
```

```
ContourPlot(datas,'s',1,10,'n','bob','y')
```

## Matlab Code for Reading Fluent Profiles

```
function[var1,var2,var3,var4,var6,var7,var8]=fluentread(filename,num_var)


data=textread(filename,'%s%*[^\n]');

n=length(data);

vn=(n-2*(num_var+1))/num_var;


for i=1:num_var

    varloc=[(i-1)*vn+2*i 0 i*vn+2*(i-1)+1 0];

    vari=dlmread(filename,'\t',varloc);

    eval(['var' num2str(i) '= vari;'])

end



end
```

## Matlab Code for Writing Fluent Profiles

```
function[message]=fluentwrite3(filename,location,x,y,z,var,var_name)


xl=length(x);

xls=mat2str(xl);

firstline=['((',location,' ','point',' ',xls,')'];

varline=['(',var_name];

dlmwrite(filename,firstline,'')

dlmwrite(filename,'(x','-append','delimiter','')

dlmwrite(filename,x,'-append','delimiter','','precision',8)

dlmwrite(filename,')','-append','delimiter','')

dlmwrite(filename,'(y','-append','delimiter','')

dlmwrite(filename,y,'-append','delimiter','','precision',8)

dlmwrite(filename,')','-append','delimiter','')

dlmwrite(filename,'(z','-append','delimiter','')

dlmwrite(filename,z,'-append','delimiter','','precision',8)

dlmwrite(filename,')','-append','delimiter','')

dlmwrite(filename,varline,'-append','delimiter','')

dlmwrite(filename,var,'-append','delimiter','','precision',8)

dlmwrite(filename,')','-append','delimiter','')

dlmwrite(filename,')','-append','delimiter','')


end
```

## Matlab Code for Converting Fluent Profiles to Contours

```
%-----------------------------------------------------------------------
% function [NewData] = SList2Contour(Data)
% Purpose: Take data from "Structured List" format to "Contour" format
%
% Inputs
%
% Data is a [m x 3] cell array or numeric array with the input values. The
%   first two columns should be reserved for the coordinates; the third for
%   data values.
%
%   Data =  [x1 y1 z11]
%           [x1 y2 z12]
%           [. .  . ]
%           [. .  . ]
%           [x1 yn z1n]
%           [x2 y1 z21]
%           [x2 y2 z22]
%           [. .  . ]
%           [. .  . ]
%           [x2 yn z2n]
%           [. .  . ]
%           [. .  . ]
%           [xm y1 zm1]
%           [xm y2 zm2]
%           [. .  . ]
```

```
%          [.  .   . ]
%          [xm yn zmn]
%
% Outputs
%
% NewData is a [m x 3] cell array holding the output values. The first two
%   columns are [m x 1] and [n x 1] coordinate arrays. The third column is
%   a [m x n] array used for storing the value of interest. m does not have
%   to be equal to n.
%
%   NewData =  [x1 y1 [z11 z12 ... z1n] ]
%              [x2 y2 [z21 z22 ... z2n] ]
%              [ .  . [ .    . ...  . ] ]
%              [ .  . [ .    . ...  . ] ]
%              [ . yn [ .    . ...  . ] ]
%              [xm  0 [zm1 zm2 ... zmn] ]
%
%-----------------------------------------------------------------------
   clc


   if (iscell(Data))
      x = Data{1};
      y = Data{2};
      z = Data{3};
   elseif (isnumeric(Data))
      x = Data(:,1);
      y = Data(:,2);
```

```
    z = Data(:,3);
else
    Display('Incorrect format for data array; terminating')
    return
end

val = 1;
while gt(val,0)
    if x(val)==x(val+1)
    val=val+1;
    else
        ycount = val;
        val=0;
    end
end

xcount = length(x)/ycount;
X = zeros(xcount,1);
Z = zeros(ycount,xcount);

for i=1:xcount
    X(i) = x(ycount*i);
end

Y = y(1:ycount);

for i=1:xcount
```

## Matlab Code for Plotting Contours from Fluent

```
function [] = ContourPlot(Data,Format,Fill,Num,Flip,Var,Save)
%-----------------------------------------------------------------------
% function [] = ContourPlot(Data,Format,Fill,Num,Flip,Var,Save)
% Purpose: Take 3D data and product contour plots
%
% Inputs
%
% Data: [m x 3] array. First two columns are coordinate data, second
%   column contains the variable of interest.
%
% Format: There are three usable formats.
%
%   'c' is for Contour format. Example below. In this format, m does not have
%   to equal n.
%   Data =  [x1 y1 [z11 z12 ... z1n] ]
%           [x2 y2 [z21 z22 ... z2n] ]
%           [ .  . [ .    . ...  . ] ]
%           [ .  . [ .    . ...  . ] ]
%           [ . yn [ .    . ...  . ] ]
%           [xm  0 [zm1 zm2 ... zmn] ]
%
%   's', stands for Structured List format. Example provided below.
%   Data =  [x1 y1 z11]
%           [x1 y2 z12]
```

```
%       [. . . ]
%       [. . . ]
%       [x1 yn z1n]
%       [x2 y1 z21]
%       [x2 y2 z22]
%       [. . . ]
%       [. . . ]
%       [x2 yn z2n]
%       [. . . ]
%       [. . . ]
%       [xm y1 zm1]
%       [xm y2 zm2]
%       [. . . ]
%       [. . . ]
%       [xm yn zmn]
%
% 'p', stands for Point Cloud format. Example provided below.
% In this format, m does not have to equal n. Note that in its current
% form, this can require a significant amount of time, so the completion
% percentage is printed on the screen. It is not recommended to use this
% during an automation sequence as a 50 x 50 contour, resulting in 2500
% data points, takes approximately one hour to generate.
% Data =  [x11 y11 z11]
%       [x12 y12 z12]
%       [ . . . ]
%       [ . . . ]
%       [x1n y1n z1n]
```

```
%         [x21 y21 z21]
%         [x22 y22 z22]
%         [ .  .  . ]
%         [ .  .  . ]
%         [x2n y2n z2n]
%         [ .  .  . ]
%         [ .  .  . ]
%         [xm1 ym1 zm1]
%         [xm2 ym2 zm2]
%         [ .  .  . ]
%         [ .  .  . ]
%         [xmn ymn zmn]
%
%   'surf', stands for Surface. Depending on how many points are chosen,
%   this could take a long time to generate.
%
% Fill: Integer value. 1 = filled contour; any other number = not filled
%
% Num: Number of contour lines.
%
% Flip: Flips the axes for the contour plot, i.e., (x,y,z) -> (y,x,z')
%
% Var: Character value. Allows user to provide a variable name for the
%   filename of the saved plots.
%
% Save: Allows the user to save plots as JPEG images. 'y' saves; 'n'
%   doesn't.
```

```
%
%------------------------------------------------------------------------


clc


if (isnumeric(Data)==1)
    Data = {Data(:,1), Data(:,2), Data(:,3)};
end


if (Format=='c')


    if (Flip==1)
        Data = {Data{2}, Data{1}, Data{3}'};
    end


    if (Fill==0)
        figure(1)
        contour(Data{1},Data{2},(Data{3}(:,:))',Num)
        colorbar
        if (Flip==1)
            xlabel('x2')
            ylabel('x1')
        else
            xlabel('x1')
            ylabel('x2')
        end
```

```
    if (Save=='y')
        filename = strcat(Var,'_surface_contour_1.jpg');
        m=1;
        while 2==exist(filename,'file')
        m=m+1;
        filename = strcat(Var,'_surface_contour_',num2str(m),'.jpg');
        print('-f1','-djpeg',filename)
        end
    end

elseif (Fill==1)
    figure(1)
    contourf(Data{1},Data{2},(Data{3}(:,:))',Num)
    colorbar
    if (Flip==1)
        xlabel('x2')
        ylabel('x1')
    else
        xlabel('x1')
        ylabel('x2')
    end

    if (Save=='y')
        filename = strcat(Var,'_surface_contour_1.jpg');
        m=1;
        while 2==exist(filename,'file')
```

```
            m=m+1;
            filename = strcat(Var,'_surface_contour_',num2str(m),'.jpg');
            print('-f1','-djpeg',filename)
            end
        end

    else
        Display('Incorrect fill value; terminating')
        return
    end

elseif (Format=='s')

    [Data] = SList2Contour(Data);

    if (Flip==1)
        Data = {Data{2}, Data{1}, Data{3}'};
    end

    if (Fill==0)
        figure(1)
        contour(Data{1},Data{2},(Data{3}(:,:))',Num)
        colorbar
        if (Flip==1)
            xlabel('x2')
            ylabel('x1')
        else
```

```
        xlabel('x1')
        ylabel('x2')
    end

    if (Save=='y')
        filename = strcat(Var,'_surface_contour_1.jpg');
        m=1;
        while 2==exist(filename,'file')
        m=m+1;
        filename = strcat(Var,'_surface_contour_',num2str(m),'.jpg');
        print('-f1','-djpeg',filename)
        end
    end

elseif (Fill==1)
    figure(1)
    contourf(Data{1},Data{2},(Data{3}(:,:))',Num)
    colorbar
    if (Flip==1)
        xlabel('x2')
        ylabel('x1')
    else
        xlabel('x1')
        ylabel('x2')
    end

    if (Save=='y')
```

```
            filename = strcat(Var,'_surface_contour_1.jpg');
            m=1;
            while 2==exist(filename,'file')
            m=m+1;
            filename = strcat(Var,'_surface_contour_',num2str(m),'.jpg');
            print('-f1','-djpeg',filename)
            end
        end

    else
        Display('Incorrect fill value; terminating')
        return
    end

elseif (or((Format=='p'),(strcmp(Format,'surf'))))

    if (Format=='p')
        surf = SurfaceFit(Data,'p','dontcare','n');
        xminmax = fix([min(Data{1}), max(Data{1})]/.01)*.01;
        yminmax = fix([min(Data{2}), max(Data{2})]/.01)*.01;

    else
        [xmin xmax] = FindSurfaceLimits(Data,0,0,0,1);
        [ymin ymax] = FindSurfaceLimits(Data,0,0,0,2);

        xminmax = [xmin xmax];
        yminmax = [ymin ymax];
```

```
end

xr = xminmax(1):((xminmax(2)-xminmax(1))/20):xminmax(2);
yr = yminmax(1):((yminmax(2)-yminmax(1))/20):yminmax(2);
M = zeros(length(xr),length(yr));

for i=1:length(xr)
    for j=1:length(yr)
        M(i,j) = surf(xr(i),yr(j));
        prog = ((i-1)*length(yr)+j)/length(xr)/length(yr)*100 %#ok<NOPRT,NASGU>
    end
end

Data = {r1' r2' M};

if (Flip==1)
    Data = {Data{2}, Data{1}, Data{3}'};
end

if (Fill==0)
    figure(1)
    contour(Data{1},Data{2},Data{3},Num)
    colorbar
    if (Flip==1)
        xlabel('x2')
        ylabel('x1')
    else
```

```
        xlabel('x1')
        ylabel('x2')
    end

    if (Save=='y')
        filename = strcat(Var,'_surface_contour_1.jpg');
        m=1;
        while 2==exist(filename,'file')
        m=m+1;
        filename = strcat(Var,'_surface_contour_',num2str(m),'.jpg');
        print('-f1','-djpeg',filename)
        end
    end

elseif (Fill==1)
    figure(1)
    contourf(Data{1},Data{2},Data{3},Num)
    colorbar
    if (Flip==1)
        xlabel('x2')
        ylabel('x1')
    else
        xlabel('x1')
        ylabel('x2')
    end

    if (Save=='y')
```

```
            filename = strcat(Var,'_surface_contour_1.jpg');
            m=1;
            while 2==exist(filename,'file')
            m=m+1;
            filename = strcat(Var,'_surface_contour_',num2str(m),'.jpg');
            print('-f1','-djpeg',filename)
            end
        end



    else
        Display('Incorrect fill value; terminating')
        return
    end


else
    Display('Incorrect format value; terminating')
    close all;
    return
end
```

**Peter Timothy Ingram**

**Vita**

## Education

The Pennsylvania State University, University Park, PA

Ph.D., Mechanical Engineering, August 2023

The Pennsylvania State University, University Park, PA

M.S., Mechanical Engineering, August 2017

Grove City College, Grove City, PA

B.S.M.E., May 2008

## Employment

The Pennsylvania State University, The Behrend College, Erie, PA

Lecturer in Mechanical Engineering and Mechanical Engineering Technology, August 2018 to present

## Published Papers

P. T. Ingram and S. Yavuzkurt, "Calculations of 3-D Distribution in Film Cooled Flat plates Using 2-D Empirical Correlations for Film Cooling Effectiveness and Heat Transfer Coefficient augmentation," in *ASME Turbo Expo*, Copenhagen, Denmark, 2012.

P. T. Ingram and S. Yavuzkurt, "Derivation of 2-D Empirical Correlations for Film Cooling Effectiveness and Heat Transfer Coefficient augmentation From Spanwise Averaged Data and Correlations," in *ASME Turbo Expo*, San Antonio, Texas, USA, 2013.

P. T. Ingram and S. Yavuzkurt, "A Superposition Technique for Multiple-Row Film Cooling for Calculations of 2-D effectiveness and Heat Transfer Coefficients," in *ASME Turbo Expo*, Montreal, Canada, 2014